Title
Microfluidics for investigating single-cell biodynamics

Author
Cookson, Scott Warren

Publication Date
2008

UNIVERSITY OF CALIFORNIA, SAN DIEGO

Microfluidics for Investigating Single-Cell Biodynamics

A dissertation submitted in partial satisfaction of the requirements for the degree
Doctor of Philosophy

in

Bioengineering

by

Scott Warren Cookson

Committee in charge:

Jeff Hasty, Chair
Marcos Intaglietta
Tracy Johnson
Julian Schroeder
Lev Tsimring
Kun Zhang

2008

The dissertation of Scott Warren Cookson is approved, and it is acceptable in quality and form for publication on microfilm and electronically:

Chair

University of California, San Diego

2008

DEDICATION

For my wife

Natalie

and our loving families

TABLE OF CONTENTS

LIST OF ABBREVIATIONS

AU	arbitrary units
bp	base pair
CAD	computer-aided design
CFP	cyan fluorescent protein
CTMS	chlorotrimethylsilane
DES	discrete element simulations
div.	division
DNA	deoxyribonucleic acid
E. coli	*Escherichia coli*
eqn.	equation
fig.	figure
fl.	fluorescence
FP	fluorescent protein
FSC	forward scatter
GFP	green fluorescent protein
HPLC	high-pressure liquid chromatography
IPTG	isopropyl β-D-1-thiogalactopyranoside
LB	lysogeny broth
MD	molecular dynamics
MQD	minimum quadratic difference
mRNA	messenger ribonucleic acid
MW	molecular weight
no.	number
OD	optical density
ODE	ordinary differential equation
PB	photobleach
PBS	phosphate buffered saline

PCR	polymerase chain reaction
PDMS	poly(dimethylsiloxane)
PIV	particle image velocimetry
RBITC	Rhodamine B isothiocyanate
RFP	red fluorescent protein
RHS	right-hand side
S. cerevisiae	*Saccharomyces cerevisiae*
SD	synthetic drop-out
TμC	Tesla microchemostat
UV	ultraviolet
yemGFP	monomeric yeast-enhanced green fluorescent protein
yeVFP	yeast-enhanced Venus fluorescent protein
YFP	yellow fluorescent protein
YG	yellow-green

LIST OF FIGURES

LIST OF TABLES

ACKNOWLEDGEMENTS

I warmly acknowledge my advisors, Drs. Jeff Hasty and Lev Tsimring, for providing invaluable guidance and good friendship throughout my time at UCSD. Additionally, I thank my fellow researchers, whose contributions were essential in completing this work. I am indebted to Jesse Stricker and Matt Bennett for their exceptional talents in molecular biology and dynamic modeling. My deepest appreciation goes to Dmitri Volfson for his computational brilliance and patient tutelage. I am grateful to Natalie Ostroff and Lee Pang for their extensive wet-lab knowledge and technical savvy. Finally, I thank the National Defense Science and Engineering Graduate (NDSEG) Fellowship program sponsored by the United States Department of Defense (DoD) and administered by the American Society for Engineering Education (ASEE) for funding.

Chapter 2 contains material originally published as Cookson, S.*, Ostroff, N.*, Pang, W. L.*, Volfson, D., and Hasty, J., 2005: Monitoring dynamics of single-cell gene expression over multiple cell cycles. *Mol. Syst. Biol.*, **1**, msb4100032-E1-6. (*equal contribution). Copyright permission to republish here was granted by Nature Publishing Group.

Chapter 3 contains material originally published as Volfson, D.*, Cookson, S.*, Hasty, J., and Tsimring, L. S., 2008: Biomechanical ordering of dense cell populations. *Proc. Natl. Acad. Sci. U. S. A.*, **105**(40), 15346-51. (*equal contribution). Copyright permission to republish here was granted by the National Academy of Sciences of the USA.

Chapter 4 contains material originally published as Stricker, J.*, Cookson, S.*, Bennett, M. R.*, Mather, W. H., Tsimring, L. S., and Hasty, J., 2008: A fast, robust and tunable synthetic gene oscillator. *Nature*. doi:10.1038/nature07389. (*equal contribution). Copyright permission to republish here was granted by Nature Publishing Group.

VITA

2001	Bachelor of Science in Engineering Physics University of Maine, Orono
2004–2007	Teaching Assistant, Department of Bioengineering University of California, San Diego
2007	Master of Science in Bioengineering University of California, San Diego
2003–2008	Research Assistant, Department of Bioengineering University of California, San Diego
2008	Doctor of Philosophy in Bioengineering University of California, San Diego

PUBLICATIONS

Cookson, S.*, Ostroff, N.*, Pang, W. L.*, Volfson, D., and Hasty, J., 2005: Monitoring dynamics of single-cell gene expression over multiple cell cycles. *Mol. Syst. Biol.*, **1**, msb4100032-E1-6. (*equal contribution).

Volfson, D.*, Cookson, S.*, Hasty, J., and Tsimring, L. S., 2008: Biomechanical ordering of dense cell populations. *Proc. Natl. Acad. Sci. U. S. A.*, **105**(40), 15346-51. (*equal contribution).

Stricker, J.*, Cookson, S.*, Bennett, M. R.*, Mather, W. H., Tsimring, L. S., and Hasty, J., 2008: A fast, robust and tunable synthetic gene oscillator. *Nature*. doi:10.1038/nature07389. (*equal contribution).

FIELDS OF STUDY

Major Field: Bioengineering (Synthetic Biology)

Studies in Gene Regulation
Professor Jeff Hasty and Dr. Lev S. Tsimring

ABSTRACT OF THE DISSERTATION

Microfluidics for Investigating Single-Cell Biodynamics

by

Scott Warren Cookson
Doctor of Philosophy in Bioengineering

University of California, San Diego, 2008

Jeff Hasty, Chair

Progress in synthetic biology requires the development of novel techniques for investigating long-term dynamics in single cells. Here, we demonstrate the utility of microfluidics for investigating single-cell biodynamics within tightly-controlled environments in the model organisms *Saccharomyces cerevisiae* and *Escherichia coli*. First, we develop a microfluidic chemostat for monitoring single-cell gene expression within large populations of *S. cerevisiae* over many cellular generations. We overcome typical difficulties in tracking individual cells throughout long sequences of time-lapse microscopy images by constraining colony growth to a monolayer. Second, we construct a variant of this device to elucidate a new mechanism of cellular ordering within dense *E. coli* populations. By comparing colony growth and alignment inside a long and narrow microfluidic channel with continuum models and discrete element simulations, we conclude that the observed dynamic transition from an isotropic disordered phase to a nematic ordered phase is caused by biomechanical interactions arising from cellular growth and division. Finally, we use microfluidics and time-lapse microscopy to characterize an engineered genetic oscillator in *E. coli*. We find the circuit to exhibit fast and robust oscillatory periods that can be tuned by altering inducer levels, temperature, and the growth medium. Together, these studies illustrate the role of novel measurement techniques in advancing the goals of synthetic biology. Specifically, the ability to generate single-cell expression profiles for a large number of cells is essential to understanding the roles of regulatory motifs within native and synthetic gene networks. Through such an understanding, we aim to develop an engineering-based approach to building gene-regulatory circuits, where design specifications generated from computational modeling drive the construction of regulatory networks with desired properties.

Chapter 1

Introduction

1.1 Systems Biology and Synthetic Biology

1.1.1 The Emergence of Systems Biology

Systems biology has grown rapidly following breakthroughs in the sequencing of entire organism genomes, including that of the human. These accomplishments have identified gene candidates within organisms with surprising speed and have produced large databases of sequences with unknown function. Although these technical achievements have given rise to a wealth of valuable data, they have also brought with them the realization that a greater challenge remains. Knowing gene sequences does little to help us understand the complex regulatory mechanisms that lead to biological function. Therefore, our next and more challenging task is to discover the dynamic connections between these genes, thereby revealing the intricate networks responsible for all cellular behavior.

Having emerged to meet this distinct challenge, systems biology is uniquely positioned to address the enormous complexity of biological networks. In a two-pronged approach, systems biology couples experimental research with quantitative modeling to develop an understanding of the regulatory dynamics behind biological function. Already, high-throughput technologies have been utilized to successfully reconstruct gene regulatory networks in many organisms (Tavazoie et al., 1999; Ideker et al., 2001; Ibarra et al., 2002; Gardner et al., 2003), and quantitative models have been developed to explain many complex and fundamental cellular processes (Vogelstein et al., 2000; Simon et al., 2001; Breeden, 2003; Bartek et al., 2004; Begley and Samson, 2004; Kohn and Pommier, 2005). Future successes in this field depend upon our ability to accurately extract meaningful measurements of dynamic gene regulation and to integrate this data into complete quantitative models of biological systems.

1.1.2 Aims and Methods of Synthetic Biology

To complement the progress of genome-scale measurement technologies, the discipline of synthetic biology aims to recreate the complex functions of highly-integrated gene networks within simpler regulatory architectures (Hasty et al., 2002b; Mangan et al., 2003; Basu et al., 2005; Pedraza and van Oudenaarden, 2005; Rosenfeld et al., 2005). This field seeks to reproduce in artificial systems the emergent properties found in natural biology. As these artificial systems are decoupled from the tangled and often poorly-understood interaction webs ubiquitous to native regulatory networks, they have the advantage of being subject to both tractable experimentation and mathematical modeling. The Hasty Laboratory in particular works to design, construct, and model novel engineered gene circuits. We believe that a thorough understanding of simple genetic regulatory motifs will be invaluable in elucidating the mechanisms by which native systems operate. In building and modeling basic regulatory modules, such as feedback loops, bistable switches, and oscillators, we hope to gain insight into how common regulatory architectures lead to complex biological functions, such as regulation of metabolism and cell cycle control.

Growing excitement in the field of synthetic biology is largely due to recent advances in molecular biology and *in vivo* microscopy, which provide new capabilities to probe and measure the responses of functional gene regulatory networks. Current techniques in deoxyribonucleic acid (DNA) manipulation provide researchers with great freedom in genetically engineering organisms. Genetic circuits can be assembled by combining customized DNA sequences into self-contained circular plasmids, which are then inserted ("transformed") into prokaryotic or eukaryotic cells and replicated ("cloned") by the host cell machinery. These circuits are designed with "inputs" ranging from chemical concentrations to temperature. Certain chemicals can bind to regulatory proteins, either promoting or repressing their effect on transcription rate through altering DNA binding ability. In a similar fashion, temperature fluctuations can be used to either reversibly or irreversibly denature critical regulatory proteins to modulate transcription. Genetic circuit "output" is measured via a reporter signal, which in the case of gene regulation is often a fluorescent protein (FP). While green fluorescent protein (GFP), first isolated from the bioluminescent jellyfish *Aequorea victoria*, has been most commonly used in the past, targeted sequence modifications have lately created many variants, such as yellow (YFP), cyan (CFP), and red (RFP). By measuring the production of FPs *in vivo* over time, we can extract dynamic gene expression data to be used in formulating mathematical models of regulatory systems.

Accurate measurement of dynamic FP expression requires the development of novel optical platforms for live cell imaging. These platforms must be able to monitor FP levels in single cells within a growing population over many cellular generations. Not only should they provide a means of containment that is amenable to the time-lapse imaging and tracking of single cells, but they must also support precise and dynamic control of the cellular microenvironment. Over the past decade, microfluidic technology has matured to largely fulfill its promise in satisfying these and other requirements of the biomedical community. As the Hasty Laboratory was quick to recognize the utility of these devices, the main focus of my graduate work has been on developing and using novel microfluidic platforms to investigate both native and synthetic gene regulatory dynamics in single microbial cells.

1.2 Microfluidics and Microscopy

1.2.1 Motivation for Quantitative Imaging

Quantitative descriptions of the dynamics of many important cellular processes require novel experimental techniques that enable the generation of time-series data for the governing regulatory proteins in a large number of individual living cells. An ideal data acquisition system would allow for the growth of a large population of cells in a defined environment which can be monitored by high resolution microscopy for a lengthy period of time. With such a setup, the gene expression state of each cell could be monitored for the length of the experiment, giving the experimenter accurate data about the temporal progression of each individual cell in the larger population. To this end, bioengineers have increasingly used devices with fluid channels on the micron scale known as microfluidic devices.

Microtechnology, and microfluidics in particular, can facilitate the accurate study of cellular behavior *in vitro* because it provides the necessary tools for recreating *in vivo*-like cellular microenvironments (Walker et al., 2004). Microfluidics involves the handling and manipulation of very small fluid volumes, enabling the creation and control of microliter-volume reactors while drawing advantages from low thermal mass, efficient mass transport, and large surface-area-to-volume ratios. Because fluid viscosity, not inertia, dominates fluid behavior at this scale, microfluidic flow is laminar, ensuring that the system does not include turbulent flows which would be detrimental for observing cellular behavior under high magnification. Lately, microfluidic "lab-on-a-chip" devices have become increasingly valuable as the known complexity of gene networks grows, driving the need for reduced-scale assays in probing the operational regimes of genetic circuits. The result has been the development of integrated microfluidic circuits analogous to their electrical counterparts, which aim to support large-scale multi-parameter analysis. Recent applications of microfluidics in biotechnology include DNA amplification (Huang et al., 2006), separation (Ashton et al., 2003), purification (Hong et al., 2004), and sequencing (Paegel et al., 2003); large-scale proteomic analysis (Lion et al., 2003); development of memory storage devices (Thorsen et al., 2002; Groisman et al., 2003); cell sorting (Fu et al., 2002; Huh et al., 2005); cell patterning (Chiu et al., 2000); and single-cell gene expression profiling (Thompson et al., 2004).

1.2.2 The Microfabrication Process

In recent years, soft lithography has become the preferred method for fabricating microfluidic devices for biology (Whitesides et al., 2001; Sia and Whitesides, 2003). Soft lithography includes a suite of methods for replicating a pattern using elastomeric polymers and can be represented as a three-step process comprising concept developing, rapid prototyping, and replica molding (Figure (Fig.) 1.1).

The first step, concept developing, involves drafting a device design in a computer-aided design (CAD) program. Here, a general idea for a device that serves some purpose is expanded upon using engineering approaches. Using the laws of fluid dynamics under the condition of low Reynolds number for microvolume flow, fluid channel resistances are calculated and modified to satisfy desired driving pressures and flow rates. Following fine-tuning of the entire channel architecture, the device design is broken up into multiple layers, where all features of a given height are placed on a single layer for photolithographic purposes. Finally, all device layers are printed at high resolution onto transparency film. These are then fastened to ultra-transmissive borosilicate glass for use as a photomask set in the following contact lithography step.

In rapid prototyping, a positive or negative photoresist is spin-coated onto a clean silicon wafer at a specified thickness and then exposed to ultraviolet (UV) light through a photomask to selectively crosslink the features represented by the mask. Since each exposure iteration creates all device features of a given height (being the depth of the photoresist layer), this process can be repeated to pattern the wafer for multi-layer device features. The final result is a positive relief of photoresist on the silicon wafer, known as a “master mold,” whose topology precisely reflects the desired device channel and

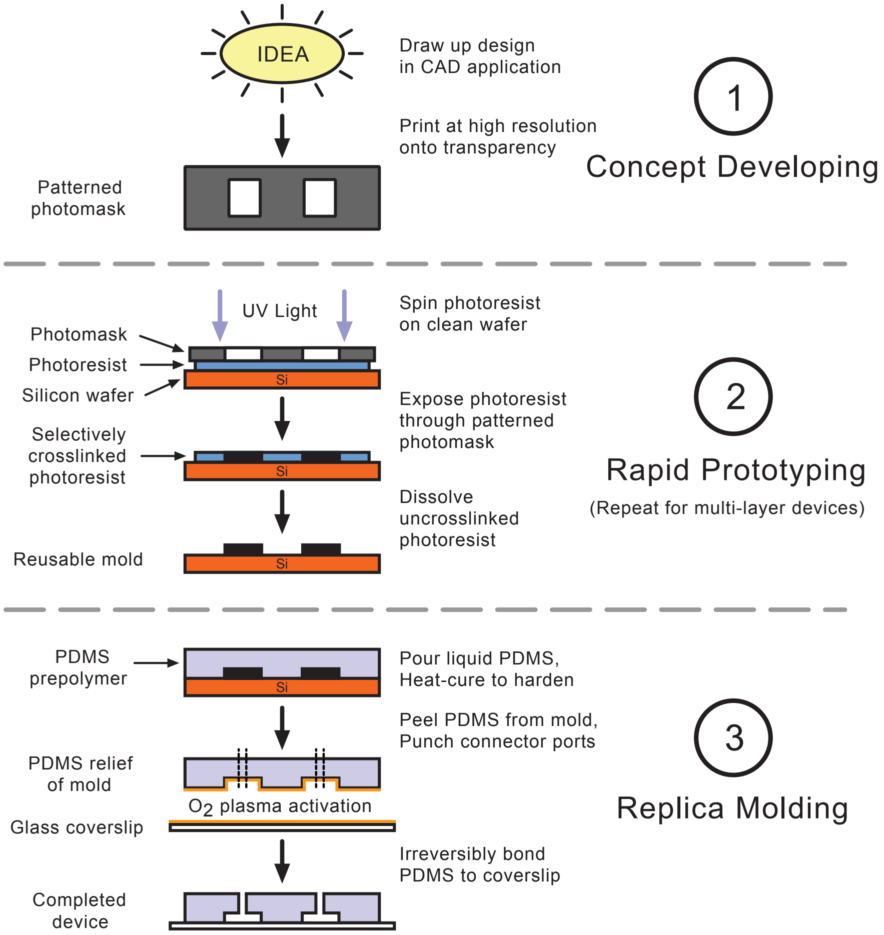

Figure 1.1: Schematic of microfluidic device fabrication using soft lithography. Soft lithography is a three-step process involving concept developing, rapid prototyping, and replica molding (adapted from Ng et al. (2002)).

feature structures and can be used repeatedly to form successive batches of devices.

The final step, replica molding, involves the casting of a transparent, silicone-based liquid prepolymer (usually poly(dimethylsiloxane) (PDMS)) against the master mold to generate a negative replica of the master. The prepolymer is first poured onto the wafer and heat-cured in place to form a rubbery silicone solid. This monolith is then peeled from the mold to reveal an inversion of the feature topology represented by the mold. For example, ridges on the master mold appear as valleys in the replica. This monolith is then diced into individual devices, bored with a cylindrical punch to form holes for connection to fluid reservoirs, and cleaned using Scotch tape and methanol. In the final step, the feature sides of the devices, along with the opposing coverslip surfaces, are briefly treated with low-power oxygen plasma. This process "activates" the surfaces of the PDMS devices and glass coverslips such that they form a permanent bond when placed in contact. In bonding the two objects, fluid channels in the PDMS are sealed against the flat coverslip surface to form microchannels that internally connect the device fluidic ports. These finished devices mark completion of the soft lithography method.

The techniques described here can be extended to perform multilayer soft lithography, which provides the capability to bond multiple patterned layers of elastomer to create active microfluidic systems containing on/off valves, switches, and pumps. Recent research in the microfluidics field has produced several examples of complex devices with hugely parallel active channel structures for high-throughput cell analysis. In approaching years, the fundamental benefits of soft lithography for biology, which include ease of fabrication, inexpensive production, and rapid device turnover, will continue to aid the researcher seeking increasingly functional cell assays.

1.2.3 Recent Applications

Microfluidics has recently found wide application in research aimed at observing cellular development within dynamic microenvironments. Devices designed for these purposes frequently possess the ability to generate thermal and/or chemical gradients across the cell development volume (Dertinger et al., 2001; Mao et al., 2002; Lin et al., 2004), and many advanced designs incorporate large-scale and highly parallel networks of fluidic channels for high-throughput cellular analysis (Hong et al., 2004; Fu et al., 2002; Balaban et al., 2004). Despite the advantages of microfluidic technology, researchers interested in studying the behavior of synthetic gene circuits have met challenges in developing platforms that enable the long-term monitoring of single cells within a large population. Therefore, much recent research has focused on this goal using various design strategies.

Wheeler et al. (2003) developed a microfluidic network enabling the passive and gentle separation of a single cell from bulk suspension. In this device, hydrostatic pressure and laminar flow streams were used to focus an individual cell to a trapping region for monitoring, while integrated valves and pumps precisely delivered reagents. Whereas this solution enabled imaging of a single cell over a relatively short time span, Tourovskaia et al. (2005) developed a microfluidic platform for long-term cell culture studies spanning the entire differentiation process of mammalian cells. They demonstrated operation of this device by observing a culture of muscle cells differentiating from myoblasts to myotubes over the course of two weeks.

To monitor long-term gene expression dynamics within a larger microbial population, several researchers have developed microfluidic chemostats. These devices in particular have been driven to miniaturization in recent years due to the many challenges involved in operating continuous macroscale bioreactors (such as the need for large quantities of reagents) and the need to monitor single cells within a culture. In continually providing fresh nutrients and removing cellular waste to support exponential growth, the microfluidic chemostat presents a nearly constant environment that is ideal for investigating single-cell biodynamics.

Recently, Groisman et al. (2005) reported a microfluidic chemostat for culturing bacterial and yeast cells in an array of shallow microscopic chambers with support for dynamically-defined media. This device was used to monitor colony growth from a single cell and to analyze the cellular response to an exogenously-added autoinducer. Similarly, Balagaddé et al. (2005) implemented a microfluidic bioreactor to enable the long-term culturing and monitoring of small populations of bacteria with single-cell resolution. This microchemostat contained an integrated peristaltic pump and a series of micromechanical valves to add media, remove wastes, and recover cells, and it was used to observe the dynamics of an *Escherichia coli* (*E. coli*) strain carrying a synthetic "population control" circuit.

A final implementation of the chemostat design was designed and built by the dissertation author in the Hasty Laboratory. This device, termed the Tesla microchemostat (TμC), was based on an implementation of the classic Tesla diode loop (Tesla, 1920; Duffy et al., 1999; Bendib and Français, 2001) and took advantage of precisely-controlled dimensions to constrain exponential growth of the yeast *Saccharomyces cerevisiae* (*S. cerevisiae*) and bacterium *E. coli* to cellular monolayers (Cookson*, Ostroff*, Pang*, Volfson, and Hasty, 2005, *equal contribution). Through directed planar growth over many generations, we were able to image an entire cell population within each device while simultaneously resolving the temporal evolution of gene expression in single cells. A detailed description of this device follows.

Chapter 2

Monitoring Dynamics of Single-Cell Gene Expression over Multiple Cell Cycles

2.1 Introduction

The utility of single-cell measurements with high temporal resolution has been demonstrated by recent bacterial studies, which used optical microscopy to observe *E. coli* over long time periods and reveal interesting temporal fluctuations and cell-cell variability that would otherwise be masked by population-wide measurements (Pedraza and van Oudenaarden, 2005; Rosenfeld et al., 2005). However, traditional microscopy methods, which typically involve viewing cells on a microscope slide or an agar plate, limit both the length and quality of an experimental run, as large groups of cells tend to grow out of the focal plane. Here, we present the development and application of a novel "free-running" microfluidic platform tailored to the generation and analysis of single-cell fluorescence data over many cellular generations. We demonstrate the utility of the platform with experimental data acquired from *S. cerevisiae*, a workhorse for eukaryotic cell biology. In addition, we present software designed for the extraction of time-series data from a sequence of fluorescence images. The availability of this device should greatly aid quantitative modelers of both native and synthetic genetic circuits by facilitating the long-term observance of dynamical properties of gene regulation in *S. cerevisiae* and other model organisms.

2.2 Design and Fabrication

The TμC is based on an implementation of the classic Tesla diode loop (Tesla, 1920; Duffy et al., 1999; Bendib and Français, 2001), modified for the imaging of a monolayer culture of cells growing in exponential phase for many generations. The construction is such that the side-arm of the diode forms a shallow trapping region that constrains a population of cells to the same focal plane (Fig. 2.1). Fluid flow is utilized to continuously purge cells that grow beyond the trapping region boundaries so that the device can function as a standard chemostat. Coupled with optical autofocus, this design feature allows for the TμC to operate in “free-run” mode over long time periods without the need for external adjustment.

In order to achieve free-running long experimental runs, a critical design objective was to avoid clogging between the media port and the trapping region. We developed a three-port chip design in which the main channel extending from the cell port splits into both a media channel and a waste channel downstream of the trapping region, which prohibits the collection of cells in the media port during the loading process (Fig. 2.1A). By constructing the height of the bypass channel to be two or three times the height of the trapping region, substantial flow can be maintained throughout this channel while flow through the trapping region remains minimal. Once cells are loaded, they receive nutrients via a combination of diffusion and advection. As the colony grows, fluidic resistance increases through the trapping region, and diffusion dominates the transport process (see Device Characterization section of Materials and Methods). Supplied with abundant nutrients, the cells are able to grow exponentially to fill the trapping region in a monolayer (Fig. 2.1C, D). The open walls of the trapping region allow for

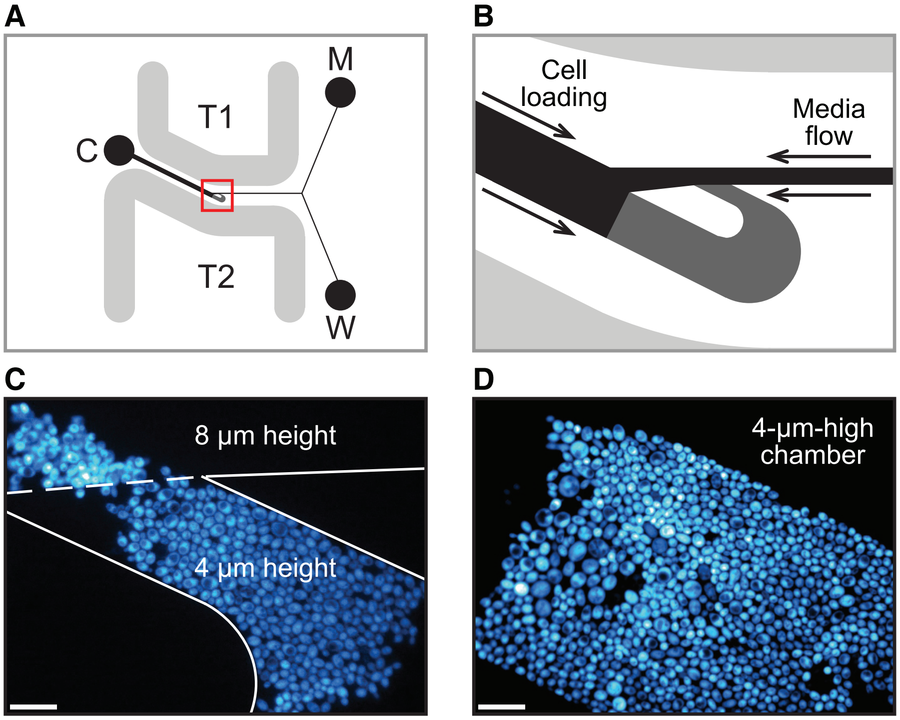

Figure 2.1: The TμC design was optimized to allow for long-term growth of cells in a monolayer. (**A**) Three separate ports for cell loading (C), media supply (M), and waste (W) minimize potential clogging of media supply lines. With this layout, we are able to generate optimal fluid flow both for the loading of cells into the trapping region and for the delivery of nutrients over many generations. Strong flow toward the trapping region provides the momentum necessary to carry cells into the region against high resistance. Cells that do not enter the trapping region are forced into the waste port by strong flow from the media port. Once cells are loaded, flow is reversed to run from the media port to both the waste and cell ports. Running temperature-regulated water through thermal lines T1 and T2 maintains the device at an optimal temperature. (**B**) A magnified view of the diode loop (red boxed region in **A**). The height of the trapping region (dark gray) is customized based on species. The flow channels (black) are 2–3 times higher than the trapping region. An open trapping region (black/gray interface) allows for peripheral cells to be pushed from the observation region as the colony grows. (**C**) Shallow trapping regions confine cells to a monolayer. Cells residing at the trapping region entrance highlight the benefit of a height-constrained growth environment. Scale bar, 20 μm. (**D**) The 4-μm-high yeast TμC full of cells after 24 h of growth. Scale bar, 20 μm.

peripheral cells to escape when they are pushed into the high flow of the main channel, thus permitting continuous exponential growth long after the trapping region becomes full.

Based on these design considerations, the TμC is constructed using standard microfabrication techniques (see Fabrication Procedure section of Materials and Methods). Briefly, a PDMS chip is created with the desired channels and microstructures from a patterned silicon wafer template. Device fabrication is relatively straightforward, as it requires only a single PDMS layer. Furthermore, flow control is maintained by passive gravitational forces alone, eliminating the need for complex on-chip actuators, flow circuitry, and run-time software. The minimal three-port design allows for a rapid experimental setup that has been optimized for convenience and requires approximately 1 h of bench time. The simplicity of device construction and experimental setup makes the platform accessible to experimentalists with minimal experience in microfabrication.

2.3 Experimental Results

We illustrate the utility of the device using the budding yeast *S. cerevisiae*, an excellent test for the TμC device owing to the tendency of cells to flocculate, or aggregate into clumps. This property presents a major obstacle in the attainment of long-term single-cell temporal data in this important model organism (Hartwell et al., 1997; Simon et al., 2001; Simon and Yen, 2003; Chen et al., 2004; McMurray and Gottschling, 2004; Scheibel et al., 2004). To address this problem, we designed the trapping region height to be approximately equal to the diameter of a single yeast cell. The significant advantage of monolayer growth in a height-constrained chamber is demonstrated by visualizing the group of cells residing at the trapping region boundary (Fig. 2.1C). The cells growing inside the 4-μm-high cell chamber are collectively in focus, and individual cells can easily be distinguished. In contrast, cells just outside of the chamber, where the height is 8 μm, grow in multiple layers, producing blurry aggregates from which quantitative single-cell data are very difficult to extract using wide-field microscopy. Although this may not impede the observation of a few cells over a short period of time, as these cells begin to divide it becomes increasingly difficult to resolve individual cells and quantify their behavior.

Using the TμC device to grow a monolayer colony of cells, we can obtain a long sequence of consistently focused fluorescence images (see Supplementary Movie 2.1). The extraction of single-cell expression dynamics from a sequence of images involves two major steps: (i) we segment each image into individual cells and (ii) we resolve the temporal evolution from the segmented images (see Image Processing section of Materials and Methods and Supplementary Movie 2.3). We utilized cells that exhibit galactose-dependent production of yeast-enhanced Venus fluorescent protein (yeVFP) from three integrated copies of the *gal1* promoter driving *yeVFP* expression. Fully induced cells are tracked through a series of images, yielding fluorescence trajectories that rise and fall with each cell cycle (Figs. 2.2A and 2.3). Since segmentation involves tracking a daughter cell from the moment the bud begins to emerge, the fluorescence signal of the mother is observed to decrease as yeVFP freely diffuses to the bud throughout the S, G2, and M phases. The fluorescence signal rises again at the beginning of the next G1 phase, when the mother and daughter have fully divided and the mother can resume the accumulation of yeVFP (Fig. 2.2B). The cell count grows exponentially until the chamber fills, at which point the chemostat enables extended run times as the population can continue growing by pushing peripheral cells out of the trapping region (Fig. 2.2C). Histograms of cell sizes at different time points throughout the experiment retain a constant distribution, indicating that growth conditions remain optimal for the duration of the run (Fig. 2.2D).

The most novel utility of the TμC is the ability to observe single-cell dynamics over long time periods. Quantitative accuracy of the fluorescence trajectories can be ensured by compensating for errors that may be introduced by experimental conditions and image analysis (see Quantitative Controls and Error Compensation section of Materials and Methods). These trajectories can be used to extract many types of information about individual cells, such as the average cell cycle time for any individual

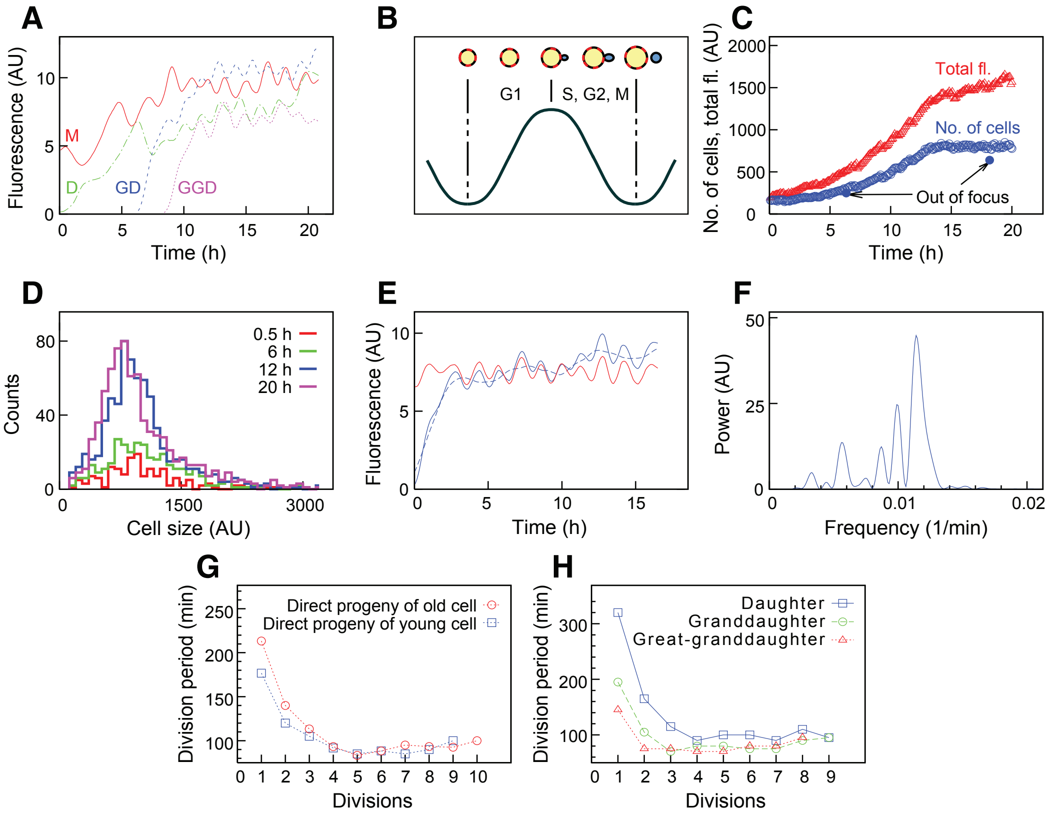

Figure 2.2: Analysis of long-term expression data acquired using the TμC. (**A**) Four representative, directly related (mother, daughter, granddaughter, great-granddaughter) trajectories showing fluorescence of each cell as a function of time. (**B**) Cartoon illustrating how the cell tracking leads to oscillations in a gene expression time series. (**C**) Total number of segmented cells as a function of time and the sum of the fluorescent signals of all cells as a function of time. (**D**) Histograms of cell sizes at various times throughout the experiment. (**E**) Data processing: raw data smoothed with an 8-point Savitsky-Golay filter (solid blue line); long-term trend obtained with a 45-point Savitsky-Golay filter (dashed blue); detrended data input to Lomb-Scargle transform (solid red). (**F**) Sample frequency spectrum of a typical trajectory, where the 0.0116 min^{-1} frequency peak corresponds to a cell division period of 86.1 min. (**G**) The time per division versus division number for progeny of a nearly senescent cell and progeny of a younger cell. Each curve is averaged over three cells. (**H**) The time per division versus division number for the daughter, granddaughter, and great-granddaughter of a nearly senescent cell.

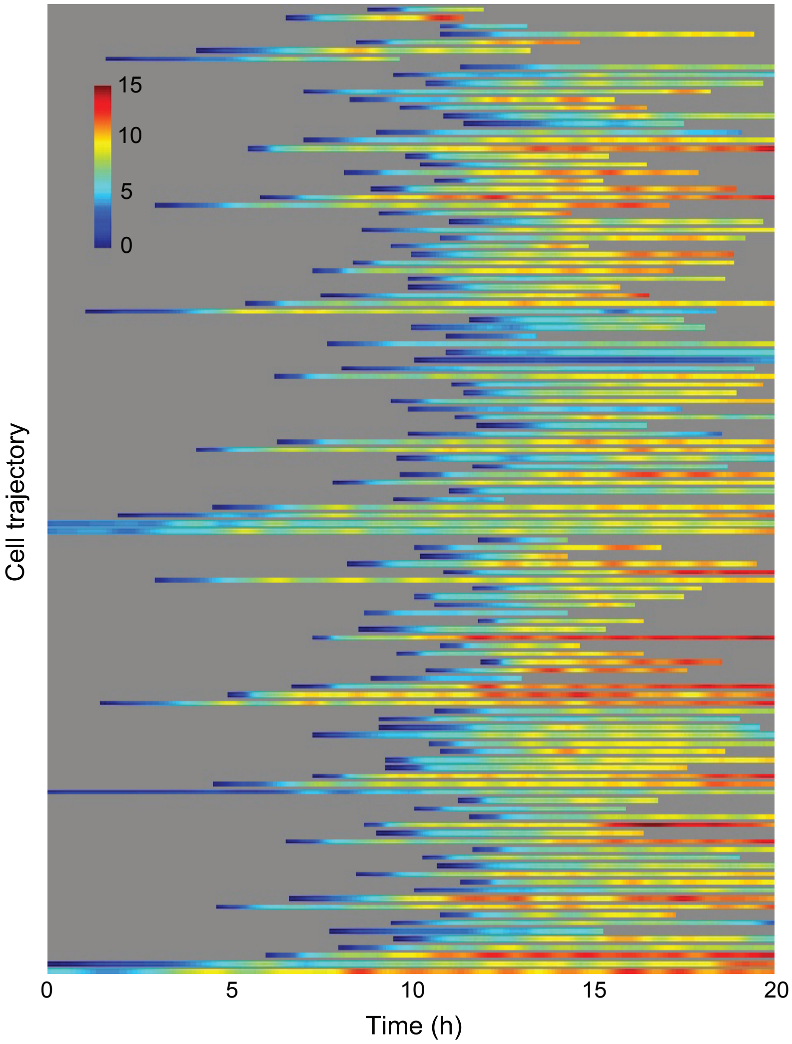

Figure 2.3: Single-cell yeVFP dynamics for 119 cells. Each row corresponds to a density plot that depicts the evolution of the amount of yeVFP in a single cell over a period of many hours (the scale bar denotes arbitrary units (AU) consistent with Fig. 2.2). Variations in cycle times and long-term trends are clearly discerned. The dynamics of yeVFP production and division were generated from the cells shown in Supplementary Movie 2.1

cell (Fig. 2.2E, F). We can also use fluorescence to monitor how the division rate of an individual cell evolves as it ages. Given that the local minima of a trajectory mark the beginning of each G1 phase, we can calculate the duration of each cell division as the time between each G1 start. As expected, the first cell cycle of a new bud is unusually long, as the bud first has to grow to a certain size before it can begin producing buds of its own. However, our fluorescence data suggest that it often takes a young cell two or three cycles to recover to a normal division rate (Fig. 2.2G). This phenomenon is particularly pronounced in daughters of old, nearly senescent cells, as reported in various studies of aging in yeast (Egilmez and Jazwinski, 1989). Fig. 2.2G compares the evolution of division times for direct progeny of an old cell and direct progeny of a young cell, averaged over three examples of each. For progeny of the young cell, we see that the first division time is long, as expected, and then the cells quickly recover down to a steady division rate. In contrast, progeny of older cells take longer to reach this steady state, as indicated by the longer division times for the first few cell cycles. This phenomenon is highlighted in Fig. 2.2H, where the division times for the daughter, granddaughter, and great-granddaughter of a nearly senescent cell are plotted. We observe that the daughter takes three cycles to recover to steady state, the granddaughter takes two cycles to recover, and the great-granddaughter recovers immediately. These cycle-time results are consistent with previous studies that utilized different assays (Egilmez and Jazwinski, 1989), and the ability to simultaneously track gene expression over long periods highlights the utility of the device.

2.4 Materials and Methods

2.4.1 Fabrication Procedure

Microfluidic devices were constructed using well-established techniques (Duffy et al., 1999; Hansen and Quake, 2003) and the UCSD Integrated Technology Laboratory (ITL). Briefly, photolithographic photomasks were drawn using FreeHand MX

(Macromedia Inc.; San Francisco, CA), printed onto transparency film at high resolution (Output City; Poway, CA), and mounted to clean borosilicate glass plates (McMaster-Carr; Los Angeles, CA). To make master molds, SU-8 2000 (MicroChem Corp.; Newton, MA) was spin-coated to appropriate depths using a Headway PWM32 programmable spinner (Headway Research Inc.; Garland, TX) and patterned by UV exposure via appropriate photomasks using a contact mask aligner (HTG; San Jose, CA). After all photolithographic steps were completed, SU-8 feature heights were verified using a DEKTAK 3030ST profilometer (Sloan Technology Corp.; Santa Barbara, CA), and treated with vaporous chlorotrimethylsilane (CTMS) for 5–10 min. PDMS (Sylgard 184; Dow Corning; Midland, MI), was mixed in a 10:1 ratio with the supplied crosslinking agent and degassed in a vacuum desiccator at $\sim$-1 atm for 30 min to 1 h. The degassed PDMS was then poured over the silicon/SU-8 master to a depth of approximately 0.5 cm and cured at 80°C for 1 h. After curing, the hardened PDMS monolith was carefully released from the master. Fluidic ports for media/cell loading and heated water lines were bored with 20- and 16-gauge Luer stub adapters, respectively, and flushed with 0.2-μm-filtered dH_2O. Individual chips were sectioned from the PDMS monolith, sonicated in a 0.1% v/v TWEEN 80 solution for 15 min, and rinsed with dH_2O. Scotch 810 office tape was used to remove any remaining particles from the PDMS surface. Finally, each chip was exposed to O_2 plasma at 30 W for 30 s in a 500-II Plasma Asher (Technics Plasma; Danville, CA) and brought into contact with plasma-cleaned 24×40 mm^2 number (no.) $1\frac{1}{2}$ coverslips (Corning Inc.; Corning, NY), which forms a strong irreversible bond between the two surfaces (Wu et al., 2002). Our photomask files are freely available for academic use and may be downloaded from our website (http://biodynamics.ucsd.edu/download.htm).

2.4.2 Device Characterization

We used two methods to characterize fluid flow through the TμC under typical run-time conditions. First, we used 0.5 μm yellow-green (YG) beads as tracers to map the flow field through the trapping region under the pressures used to deliver nutrients. We acquired a movie of bead flow at 10 frames s^{-1} and input this to a MATLAB implementation of the particle image velocimetry (PIV) method (Sveen and Cowen, 2004). PIV provides a vector field that accurately describes the magnitude and direction of flow, and the results affirmed our prediction of creeping flow through the trapping region (Fig. 2.4). From this vector field, the maximum velocity through the feeder channel was found to be $\sim$75 μm s^{-1}, and the mean velocity through the trapping region was $\sim$1.5 μm s^{-1}.

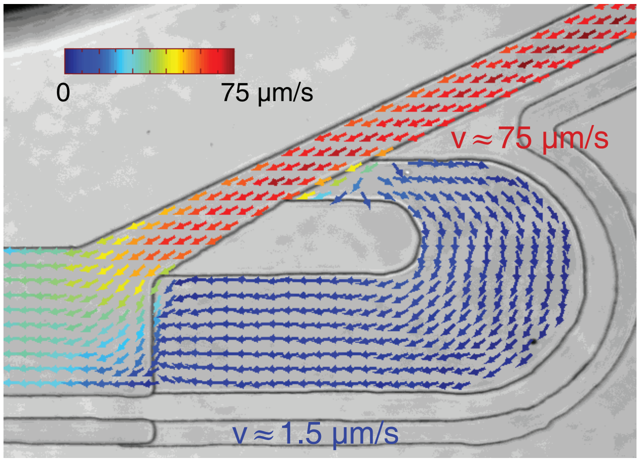

Figure 2.4: Flow vector field produced by implementing a PIV method to process images of fluorescent beads used as flow tracers. Unit velocity vectors show the direction of flow, and colors (from blue to red) correspond to the velocity magnitude (from low to high) on a log scale.

Second, in order to ensure that a culture growing in the trapping region would receive sufficient nutrients, we performed a more detailed flow characterization by simulating nutrient delivery using two red fluorescent dyes. Nutrient transport throughout the trapping region of the TμC is driven by both advective and diffusive processes, and the key parameters involved are the diffusion coefficient of each nutrient species and the advective velocity through the trapping region. We modeled this transport process by deriving a closed-form solution of the time-dependent chemical concentration profile throughout the trapping region. The analytical solution was fit to experimental data, yielding an estimate of the advective velocity.

The chemical species mass balance for unsteady diffusion with advection is

$$\frac{\partial c}{\partial t} + \vec{v} \cdot \vec{\nabla} c = \mathcal{D} \nabla^2 c. \tag{2.1}$$

Because flow within the microfluidic device is restricted to the laminar regime, analysis can be performed on the central streamline of flow through the trapping region (Fig. 2.5A). It is assumed that components of the velocity and concentration gradient normal to the direction of flow are negligible relative to the tangent components. Using this assumption, the physical process can be reduced to a 1D system (Fig. 2.5B), simplifying Equation (Eqn.) 2.1 to

$$\frac{\partial c}{\partial t} + V_0 \frac{\partial c}{\partial x} = \mathcal{D} \frac{\partial^2 c}{\partial x^2} \tag{2.2}$$

with the following boundary and initial conditions:

$$\begin{aligned} c\,(0,t) &= c_0, \quad t > 0 && (2.3) \\ c\,(L,t) &= c_0, \quad t > 0 && (2.4) \\ c\,(x,0) &= 0, \quad 0 < x < L. && (2.5) \end{aligned}$$

Here, V_0 is the average channel velocity, $\mathcal{D}$ is the molecular diffusivity of the chemical species, and c_0 is both the steady-state and boundary-supported concentration.

This system of equations can be further simplified by introducing the following dimensionless parameters:

$$\begin{aligned} C &= \frac{c - c_0}{c_0} && (2.6) \\ \xi &= \frac{x}{L} && (2.7) \\ \tau &= \frac{\mathcal{D}}{L^2} t. && (2.8) \end{aligned}$$

Hence, Eqns. 2.2–2.5 become

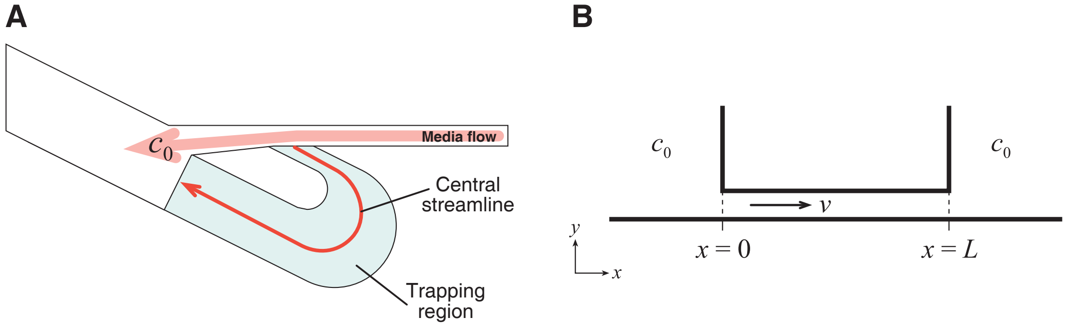

Figure 2.5: Schematics used in simulating nutrient delivery in the TμC. (**A**) Analysis is performed on the central streamline of flow through the trapping region. (**B**) 1D reduction of the system used to characterize diffusive and advective transport.

$$\frac{\partial C}{\partial \tau} + N_{\mathrm{Pe}} \frac{\partial C}{\partial \xi} = \frac{\partial^2 C}{\partial \xi^2} \tag{2.9}$$

and

$$C(0,\tau) = 0, \qquad \tau > 0 \tag{2.10}$$

$$C(1,\tau) = 0, \qquad \tau > 0 \tag{2.11}$$

$$C(\xi,0) = -1, \qquad 0 < \xi < 1, \tag{2.12}$$

where

$$N_{\mathrm{Pe}} = \frac{V_0 L}{\mathcal{D}} \tag{2.13}$$

is a dimensionless ratio of advective to diffusive transport that commonly arises in heat and mass transfer problems and is known as the Peclet number. Because this system is linear with respect to C and has homogeneous boundary conditions, it can easily be solved using the separation of variables method (Haberman, 1998). This yields the closed-form solution,

$$C(\xi,\tau) = \exp\left(\frac{N_{\mathrm{Pe}}}{2}\xi\right) \sum_{n=1}^{\infty} A_n \sin(n\pi\xi) \exp(-\lambda_n \tau) \tag{2.14}$$

or

$$c\,(x,t) = c_0 \left[\exp\left(\frac{N_{\mathrm{Pe}}}{2L}x\right) \sum_{n=1}^{\infty} A_n \sin\left(\frac{n\pi}{L}x\right) \exp\left(-\lambda_n \frac{\mathcal{D}}{L^2}t\right) + 1 \right], \tag{2.15}$$

where

$$\lambda_n = \frac{1}{4}\left[(2n\pi)^2 + N_{\mathrm{Pe}}^2\right] \tag{2.16}$$

and

$$A_n = 4\exp\left(-\frac{N_{\mathrm{Pe}}}{2}\right)\left[\frac{2n\pi\cos(n\pi) + N_{\mathrm{Pe}}\sin(n\pi) - 2n\pi\exp\left(\frac{N_{\mathrm{Pe}}}{2}\right)}{N_{\mathrm{Pe}}^2 + (2n\pi)^2}\right]. \tag{2.17}$$

Experimental concentration profiles were visualized using 10 kDa conjugated Rhodamine B isothiocyanate (RBITC). We estimated the diffusion constant of this dye using the Stokes-Einstein equation for large diffusing particles (Bird et al., 2002) as

$$\mathcal{D}_{AB} = \frac{k_b T}{6\pi\mu_B s_A}, \tag{2.18}$$

where $\mathcal{D}_{AB}$ is the diffusion coefficient of solute A in solvent B, k_b is Boltzmann's constant, T is the ambient temperature, μ_B is the dynamic viscosity of solvent B, and s_A is the molecular Stokes radius of solute A. The value of s_A was determined using a previously-reported correlation for dextrans based on molecular weight (MW) (Venturoli and Rippe, 2005):

$$s_A = 0.488\,(MW)^{0.437}\,. \tag{2.19}$$

Using this approximation, $\mathcal{D}_{AB}$ for a 10 kDa dextran was found to be 7.90×10^{-7} cm^2 s^{-1}. The calculated diffusivity of the dye was input to our analytical model of the transport process, which yielded a value of 1 μm s^{-1} for the advection velocity, V_0, and a path length, L, of 570 μm (approximately the path length analyzed in the experimental data), altogether providing a N_{Pe} of 7.125.

Experimental data was acquired by imaging fluorescent dye entering the trapping region and recording intensity values along the central streamline. Fluorescence images were acquired every 5 s for 1.4 h and post-processed by background subtraction, flat field correction, and smoothing using a 5-pixel Gaussian kernel. A quadratic interpolating spline was fit to 6–10 points manually chosen to define the central streamline and then subdivided into 100 points. For each image, fluorescence values at each point along the path were calculated as the mean pixel intensity over a 10-μm line normal to the spline. Experimental concentration was assumed to be linearly proportional to fluorescence signal and was normalized by the steady-state value. The temporal evolution profiles of the experimental data and the analytical model for the empty device are shown in Fig. 2.6. Analytical data is calculated from a 100-term Fourier series and plotted as $C'(\xi, t) = C(\xi, t) + 1$. A comparison of the two profiles shows good agreement, supporting the existence of creeping flow on the order of 1 μm s^{-1} within the trapping region of the device under normal operating conditions. In addition, the calculated velocity of the creeping flow closely matches the value obtained from the PIV analysis (1.5 versus 1.0 μm s^{-1}). The asymmetry in the concentration profile over ξ is due primarily to advective transport. Closer inspection of the analytical solution reveals that as $N_{\mathrm{Pe}} \rightarrow 0$, Eqns. 2.14–2.17 degenerate to the solution for simple 1D unsteady diffusion and the physical process becomes spatially symmetric about $\xi = 0.5$. Moreover, the speed of the transport process is highly dependent on the value of N_{Pe} (Fig. 2.7).

Our transport analysis based on the RBITC dye provides an estimate for the Peclet number in the case of a heavy molecule perfusing into the empty trapping region. To better approximate the diffusive transport of nutrients through the trapping region, we repeated this analysis with the red dye Sulforhodamine 101 (Acid-Free Texas Red), which has a diffusion constant on the same order of magnitude as a typical nutrient molecule (calculated to be 5.72$\times$10^{-6} cm^2 s^{-1}). With the diffusion constant an order of magnitude larger than RBITC, the Peclet number was an order of magnitude smaller, and we observed increased domination of diffusive over advective transport in both experimental and analytical results (Fig. 2.8). In experiments involving cells growing

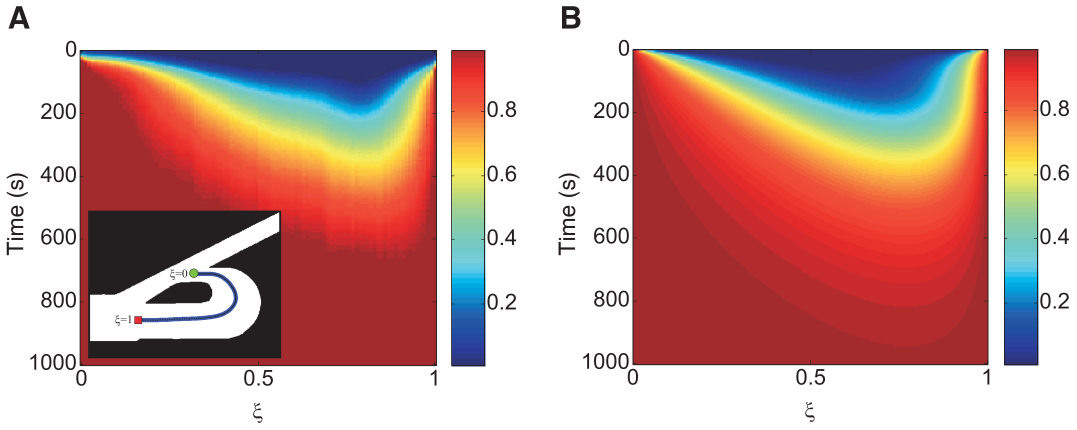

Figure 2.6: Comparison of experimental data and analytical solution for nutrient transport into the trapping region using 10 kDa Dextran-conjugated RBITC. (**A**) Experimental data collected along the central streamline of the trapping region. The inset shows the path analyzed (blue line), starting from the green circle and ending at the red square. (**B**) Analytical solution of 1D diffusion with advection for large molecule transport.

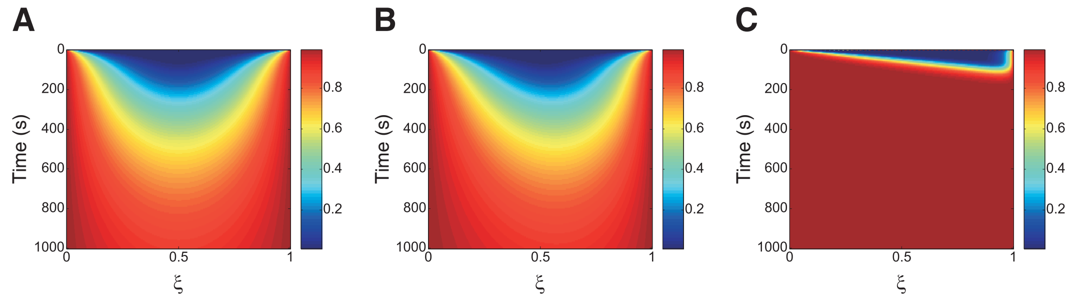

Figure 2.7: Analytical analysis of the time evolution of 1D concentration profiles for different advective velocities. (**A**) $V_0 = 0\ \mu\text{m s}^{-1}$, $N_{\text{Pe}} = 0$. (**B**) $V_0 = 0.2\ \mu\text{m s}^{-1}$, $N_{\text{Pe}} = 1.425$. (**C**) $V_0 = 5\ \mu\text{m s}^{-1}$, $N_{\text{Pe}} = 36.625$.

within the trapping region, we expected to see the Peclet number decrease even further, as advective velocity should be slowed by the increased resistance provided by colony expansion. Indeed, upon monitoring Sulforhodamine 101 dye penetration with the chamber both empty and full of cells, we found that diffusion dominates the transport process (see Supplementary Movie 2.2).

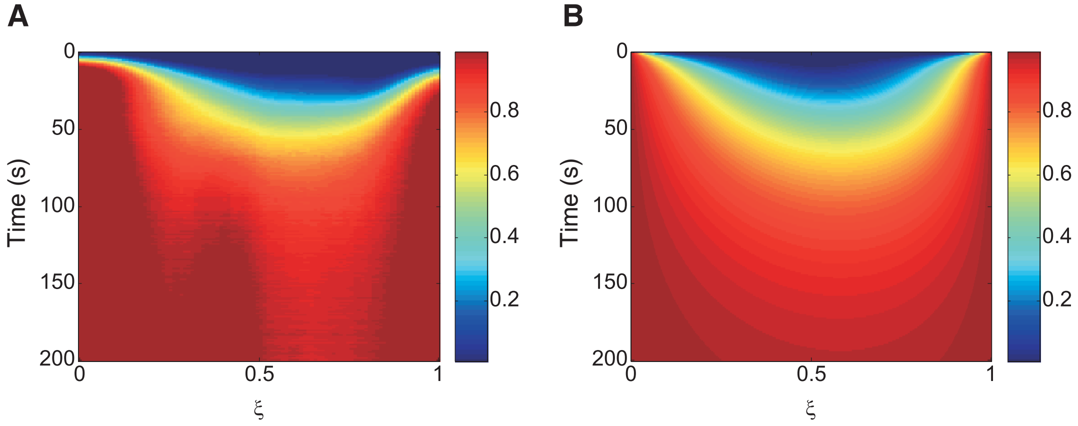

Figure 2.8: Comparison of experimental data and analytical solution for nutrient transport into the trapping region using Sulforhodamine 101. (**A**) Experimental data collected along the central streamline of the trapping region. (**B**) Analytical solution of 1D diffusion with advection for small molecule transport.

2.4.3 Strain and Cell Culture

The yeast strain was created by targeted chromosomal integration of the pRS41-yv vector (Fig. 2.9) at the *gal1-10* promoter locus of *S. cerevisiae* strain K699 (a, ADE2, ura3, his3, trp1, leu2). The vector was constructed using standard recombination techniques from two commercially available vectors. The tryptophan marker from pRS404 was inserted into the pESC-His vector containing the *gal1-10* promoter locus of *S. cerevisiae* by cutting both vectors at the AatII and NaeI restriction sites. The gene encoding a YFP variant, yeVFP, was inserted into the BamHI and XhoI restriction sites downstream of the *gal1* promoter for fluorescence production inducible by the addition of galactose to the medium. In preparation for transformation, the resulting vector, pRS41-yv, was cut at the AgeI restriction site within the *gal1-10* promoter to ensure sufficient homology for recombination into the yeast genome. Selection of integrants was performed by first growing cultures in synthetic drop-out (SD) medium containing 2% w/v glucose and supplemented with all amino acids except tryptophan. Subsequently, flow cytometry was used to identify a triple integrant in order to maximize yeVFP production. For experiments, cultures were grown in SD supplemented with all amino acids and containing 2% w/v galactose for full induction of the *gal1* promoter. To minimize flocculation of yeast while growing in the incubator shaker, a single colony was initially inoculated into a microcentrifuge tube containing 1 ml of medium and vortexed on high for 2 min before being transferred to a culture tube containing 4 ml total medium. Cultures were then grown at 30°C for 18–24 h to an optical density at 600 nm (OD_{600}) of 1.0 ± 0.25. In preparation for loading, four samples from a single culture were diluted to an OD_{600} of 0.05 in microcentrifuge tubes containing 1 ml of medium and vortexed for 5–10 min. Cultures were then recombined for a total loading volume of 4 ml.

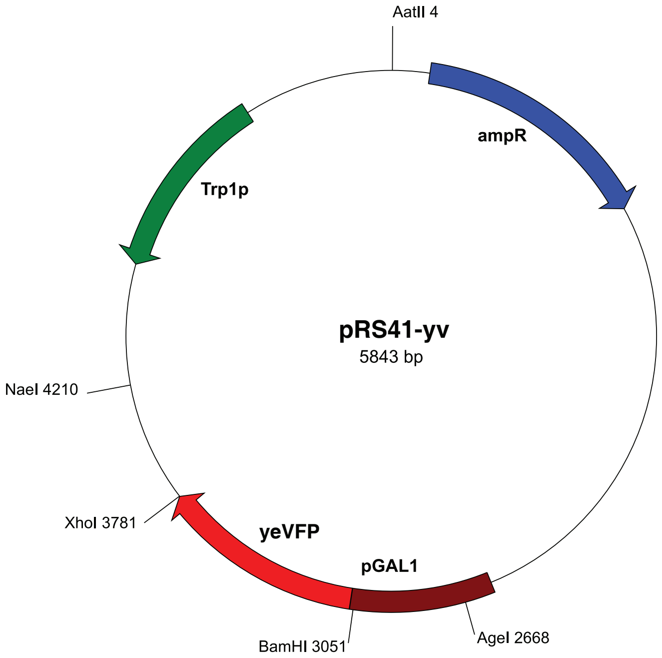

Figure 2.9: Map of the pRS41-yv vector used to integrate three copies of the *gal1* promoter driving expression of *yeVFP* into the yeast genome.

2.4.4 Loading Procedure

In preparation for cell observation, devices were mounted to the microscope stage and connected to thermal water baths to maintain the optimal growth temperature of 30°C. Thermal connections were made using Tygon microbore tubing (0.050 in inner diameter, 0.090 in outer diameter; Cole Parmer; Vernon Hills, IL) connected to chip thermal ports with 16-gauge dispensing needles (McMaster-Carr; Los Angeles, CA). Water temperatures flowing into and out of the device were monitored using in-line thermocouples. Following device priming with filtered dH_2O, an open 10 ml syringe serving as a waste reservoir was filled with medium and suspended 5 in above the device. A similar connection for medium was made at the device media port at a height of 25 in. Cells and 2.5-μm-diameter YG fluorescent beads were loaded into the device at the cell port, with the beads serving as a fluorescence intensity standard, until several of each entered the trapping region. During loading, all flows were directed toward the waste port to prevent contamination of the media line. To minimize clogging, strong flow from the media port was used to flush clear all cells residing in the shared fluid channels. Finally, the three reservoirs were brought to their final run-time heights, with the cell reservoir fixed at a height 1 in above the waste reservoir and the medium reservoir fixed at a height 1 in above the cell reservoir. These differential heights provided for both gentle flow of medium through the trapping region and strong flow of medium into the waste port, thereby feeding the cells to be monitored while preventing discarded cells from re-entering the system.

2.4.5 Microscopy

Image acquisition was performed on a Diaphot TMD epifluorescent inverted microscope (Nikon Instruments Inc.; Tokyo, Japan) outfitted with fluorescence excitation and emission filter wheels, a ProScan II XY-motorized stage with fine focus control and a hardware-based autofocus controller (Prior Scientific Inc.; Rockland, MA), and Uniblitz VS35 high-speed shutters (Vincent Associates; Rochester, NY). Images were acquired using an Orca-ER cooled CCD camera (Hamamatsu Photonics; Hamamatsu, Japan) and a custom positioning and multispectral acquisition application written in LabVIEW (National Instruments; Austin, TX). Imaging for the autofocus controller was performed using a Cohu 4900 Series CCD camera (Cohu Inc.; San Diego, CA) mounted to one of the microscope eyepieces. Fluorescence visualization of yeVFP and red fluorescent beads was performed with narrow band-pass excitation and emission filters (filter set #86006 for CFP/YFP/DsRed; Chroma Technology Corp.; Rockingham, VT).

2.4.6 Image Processing

The extraction of single-cell expression dynamics from a sequence of images involves two major steps: (i) we segment each image into individual cells, and (ii) we resolve the temporal evolution from the segmented images. To begin the segmentation process, each image is flat field corrected and pre-processed with a 3×3-pixel^2 Gaussian filter to remove high-frequency noise (Fig. 2.10A). Approximate locations of the cells are determined using a seeding technique (Adams and Bischof, 1994). To form seeds, we use the differential of the image averaged with boxcar filters of small and large sizes (5×5 pixel^2 and 15×15 pixel^2, respectively) to support the robust location of local intensity maxima independent of the mean level of the signal. The resulting binary mask is over-segmented in most cases due to the presence of vacuoles which appear as islands of the background inside the foreground cell seeds (Fig. 2.10B). These islands are eliminated by the transferring of closely-connected regions of the background into the foreground. After this correction, the resulting binary image is processed with a morphological distance transform and a watershed segmentation (Vincent, 1993). These operations produce a set of dams which separate cell seeds and are typically located at troughs of the grayscale intensity image (Fig. 2.10C). In the final step of segmentation, the seeds are used for growing the grayscale region in an operation which involves expanding the area of the cells from the peaks within the seeds down to a specified

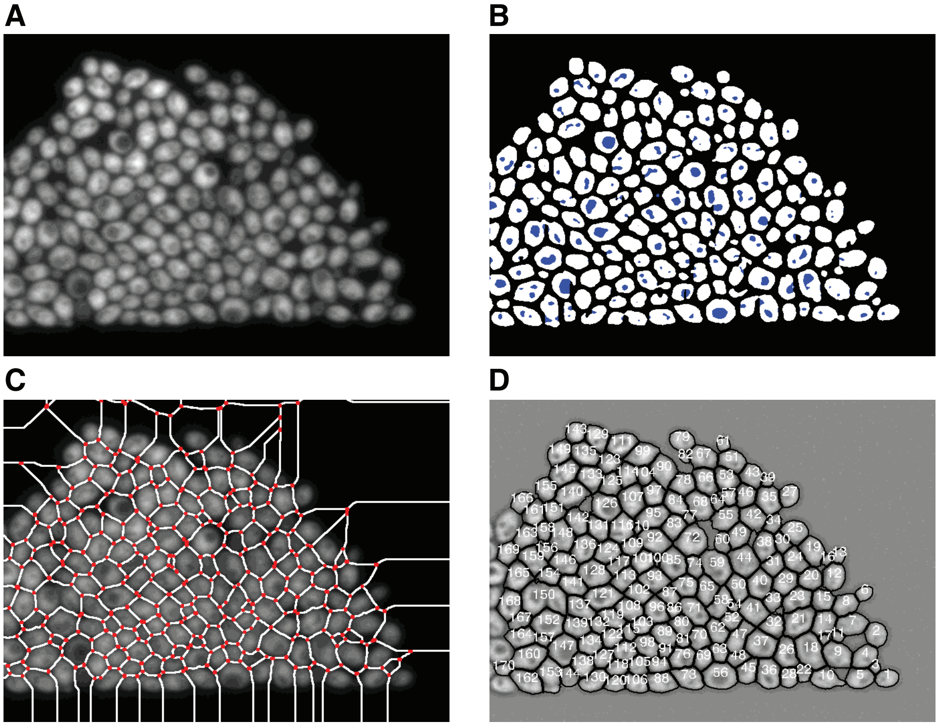

Figure 2.10: Major steps of image segmentation. For visual clarity, only one fourth of the entire image is shown. (**A**) Original fluorescence image after flat field correction and the removal of high-frequency noise. (**B**) Results of initial seeding (white) along with filled "holes" (blue) form the resulting binary mask. (**C**) Results of the watershed segmentation, where segments (white lines) joining nodes (red dots) may be eliminated in the interactive mode to allow the merging of neighboring cells. (**D**) To complete segmentation, recognized cells are enumerated and their boundaries are displayed in black. Cells crossing the boundaries of the field of view are abandoned.

level above the background (Fig. 2.10D). Here, the watershed dams serve to preclude the joining of neighboring cells during the growth process. In addition, the same skeleton of dams is used to allow for an effective means of manual correction, since the removal of a dam segment between touching cells usually results in their joining during the growing of the grayscale region. The resulting algorithm is implemented using the Interactive Data Language (IDL) programming language (ITT Visual Information Solutions; Boulder, CO). In automated mode, which is used in most cases, the segmentation of a single image with 800 cells takes about 30 s on a standard personal workstation (see Supplementary Movie 2.3). In this mode, we determined that the fraction of errors in segmentation typically does not exceed 5% of the total number of recognized cells. Segmentation errors arise primarily when dark regions inside a cell take on values close to the background level, causing the software to draw a watershed line through the cell, or when the boundary between two cells is difficult to observe, causing them to be considered a single cell.

For the second step of image analysis, in which cells are tracked through a set of segmented images, we adopted a set of tools developed in the context of colloidal suspensions and granular materials (Crocker and Grier, 1996). These tools implement cluster analysis, and we used the center of mass coordinates and the total fluorescence integrated over the cellular area as our cluster variables. Errors in this step arise primarily when a clump of cells near the trapping region boundary breaks off and leaves the chamber, causing a shift in the positions of many cells in the chamber. A manual correction option during each step of the image processing makes it possible to correct for errors, and future implementations of the software will include improvements upon these methods. Our image analysis software is freely available for academic use and may be downloaded from our website (http://biodynamics.ucsd.edu/download.htm).

2.4.7 Quantitative Controls and Error Compensation

Quantitative accuracy of the fluorescence trajectories can be ensured by compensating for errors that may be introduced by experimental conditions and image analysis. As a quantitative control in our cell experiments, we simultaneously imaged calibration-standard fluorescent beads of similar brightness. Because these beads are resistant to photobleaching, any variation in intensity from frame to frame will be a measure of deviations due to either focal drift or fluorescent bulb fluctuations. The trajectory of a bead is shown in Fig. 2.11A alongside a typical cell trajectory. The coefficient of variation of the bead signal was found to be 3.0%. While this low noise level is negligible when analyzing general trends in data, the bead trajectory can be used to compensate for experimental error in studies for which these fluctuations would be more detrimental.

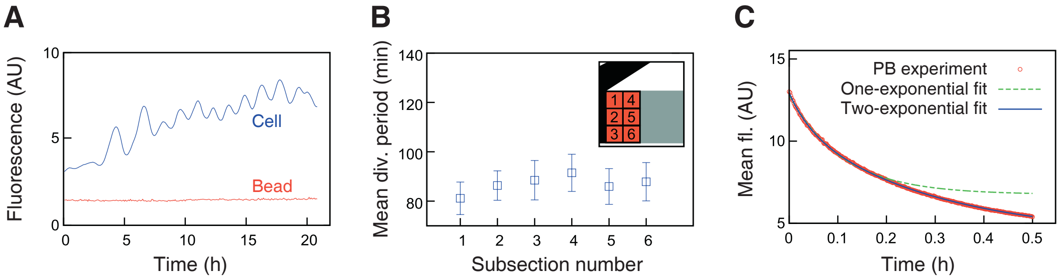

Figure 2.11: Quantitative controls performed to ensure accuracy of the fluorescence data. (**A**) The fluorescence trajectory of a bead (red) alongside a sample cell trajectory (blue). (**B**) Mean division period in each of six subsections of the field of view. Error bars represent standard deviation, and the inset shows a map of subsections. (**C**) Results of a photobleaching experiment to determine the decay rate of yeVFP in response to fluorescent light exposure. Experimental data is shown as red circles. The best fit is given by a two-exponential function (solid blue curve). However, in the analysis we used a one-exponential fit (dashed green curve) for simplicity.

A concern regarding cells being constrained to a shallow chamber is that nutrients may be unevenly distributed, leading to varying growth rates throughout the trapping region. To address this question, we divided the field of view into subsections and calculated division period statistics for all cells residing in each area. We extracted the average cell cycle time for each trajectory by analyzing a power spectrum of the time-series data. Spectra were calculated using the Lomb-Scargle transform for unevenly-spaced data to account for occasional gaps due to tracking errors. In calculating the average cell division period in each of six regions, we found a mean and standard deviation of 86.88 and 3.43 min respectively (Fig. 2.11B). This low variation reflects the constant micro-environment throughout the observed region.

Another typical concern in fluorescence microscopy is that the intermittent exposure of fluorescent molecules to high-intensity light will bleach them over time, adversely affecting the data. To address this, we acquired a photobleaching curve and modeled the effects of exposure on the quantitative integrity of our fluorescence trajectories. In a typical experiment, fluorescence images were acquired every 5 min with exposure times of 50–250 ms. With these acquisition settings, effects of photobleaching of yeVFP molecules were determined to be negligible. A photobleaching curve was obtained by subjecting a full field of view of cells expressing *yeVFP* to constant exposure of fluorescent light. Images were captured every 1.6 s, and mean fluorescence over a region of interest was plotted against time (Fig. 2.11C). We fit this data using both one- and two-exponential functions and for simplicity used a one-exponential fit to obtain the decay rate, γ_p, for yeVFP due to exposure from fluorescent light.

To model the effect of photobleaching on our acquisition of a single-cell fluorescence trajectory, we assume that the fluorescence data obtained from a cell, $\dot{x}$, is a combination of the true fluorescence signal, $f\left(x,t\right)$, plus a degradation term dependent on the amount of yeVFP present in the cell, x:

$$\dot{x} = f\left(x,t\right) - \gamma_p x. \tag{2.20}$$

In order to extract the true signal from the observed signal, we use an explicit first-order discrete model of the ordinary differential equation (ODE) as follows:

$$\left(x_{i+1} - x_i\right)\frac{1}{\Delta t} = f_i\left(x,t\right) - \gamma_{eff} x_i. \tag{2.21}$$

Here, γ_{eff} is the effective decay rate representing the effect of photobleaching due to a single exposure of duration Δt. This equation can be rearranged to give an expression for $f_i\left(x,t\right)$:

$$f_i\left(x,t\right) = \left(x_{i+1} - x_i\right)\frac{1}{\Delta t} + \gamma_{eff}x_i. \tag{2.22}$$

We now want to approximate the actual value of the fluorescence data as it would be recorded if there was no degradation due to photobleaching. The corrected fluorescence value, $\tilde{x}_{i+1}$, at each time point can be evaluated based on the current and previous data points as follows:

$$\tilde{x}_{i+1} = x_i + \Delta t f_i\left(x,t\right) = x_i + \Delta t\left[\left(x_{i+1} - x_i\right)\frac{1}{\Delta t} + \gamma_{eff}x_i\right] = x_{i+1} + \Delta t\gamma_{eff}x_i. \tag{2.23}$$

The effective decay rate, γ_{eff}, should have the same effect on fluorescent intensity over Δt that the calculated decay rate, γ_p, has over the duration of exposure, t_{exp}. That is, $\gamma_{eff}\Delta t = \gamma_p t_{exp}$. Given a maximum exposure time of 250 ms and the value of γ_p calculated from the photobleaching curve of 0.256, we find that the value of $\gamma_{eff}\Delta t$ yields a negligible correction term of 0.1% for each fluorescence value, x_{i+1}. Correcting a given trajectory for this effect has a negligible effect on the data.

An additional concern regarding the extraction of quantitative information from fluorescence microscopy data is that an individual cell, which often moves throughout the field of view during an experiment due to colony expansion, may not experience spatially-constant illumination. To address this concern, we applied a flat field correction to each image to compensate for nonlinearities in our microscope optics. The correction matrix was determined by filling the field of view with a fluorescent dye of even thickness and acquiring an image at the run-time settings. Since the ideal signal should be constant over all pixels, this image could be used as a weighting template to remove optical artifacts from our data due to variations in either the pixel-to-pixel sensitivity of the camera or distortions in the optical path.

2.5 Acknowledgements

Chapter 2 contains material originally published as Cookson, S.*, Ostroff, N.*, Pang, W. L.*, Volfson, D., and Hasty, J., 2005: Monitoring dynamics of single-cell gene expression over multiple cell cycles. *Mol. Syst. Biol.*, **1**, msb4100032-E1-6. (*equal contribution). Copyright permission to republish here was granted by Nature Publishing Group.

Chapter 3

Biomechanical Ordering of Dense Cell Populations

3.1 Introduction

In the process of developing the TμC for use with *S. cerevisiae* (Cookson*, Ostroff*, Pang*, Volfson, and Hasty, 2005, *equal contribution), we found it possible to customize the design for use with other cell species. In particular, we found the device to be well-suited for monolayer imaging of the prokaryotic workhorse *E. coli*. This led to a study of bacterial pattern formation in constrained microenvironments, with a specific focus on cell ordering observed in dense cell populations.

The structure of bacterial populations is governed by the interplay of many physical and biological factors, ranging from properties of surrounding aqueous media and substrates to cell-cell communication and gene expression in individual cells. The biomechanical interactions arising from the growth and division of individual cells in confined environments are ubiquitous, yet little work has focused on this fundamental aspect of colony formation. In the following work, we analyze the spatial organization of *E. coli* growing in a microfluidic chemostat. We find that growth and expansion of a dense colony of cells leads to a dynamical transition from an isotropic disordered phase to a nematic phase characterized by orientational alignment of rod-like cells. We develop a continuum model of collective cell dynamics based on equations for local cell density, velocity, and the tensor order parameter, and we combine this model with discrete element simulations (DES) to elucidate the mechanism of cell ordering and quantify the relationship between the dynamics of cell proliferation and the spatial structure of the population.

Morphogenesis is a highly important theme in both biology and nonequilibrium physics. The fundamental issue is to understand how the local interactions of elementary components lead to collective behavior and the formation of highly organized systems. In nature, this self-organization can lead to significant selective advantages for living organisms and is found on many levels, from biomolecules and single cells to schools of fish and herds of animals. Recent findings indicate that bacteria actively migrate toward surfaces and small enclosed spaces, where they form high-density microcolonies to facilitate quorum sensing (Park et al., 2003). To resist environmental stresses, some species of bacteria form biofilms (Donlan, 2002; Davies et al., 1998; Bassler, 2002), which are commonly present in both natural environments (including living tissues, soils, and aquatic systems) and on synthetic surfaces (such as industrial piping and device implants). Generally, the collective dynamics of such cell populations involve a complex interplay of various physical, chemical, and biological phenomena such as chemotaxis (Pratt and Kolter, 1998), motility (Josenhans and Suerbaum, 2002), cell-cell signaling (Schuster et al., 2004), adhesion (Hinsa et al., 2003), and gene regulation (Schembri et al., 2003).

An important unexplored consequence of the formation of high-density bacterial colonies is spatial organization caused by the “contact biomechanics” arising from cellular growth and division. At low density, communication among cells occurs mainly through chemotaxis, but as bacteria aggregate and form dense communities, direct biomechanical interaction plays an increasingly strong role in colony organization. Although previous studies have explored the complex signaling mechanisms involved in the early stages of biofilm formation, the biomechanics of direct cellular contacts have received little attention. To address this issue, we focus here on the essential structure and dynamics of a growing pseudo-2D colony of non-motile bacteria within a controlled microfluidic environment. In isolating this aspect of colony development, we are able to develop a precise quantitative understanding of the role of biomechanical interactions in the formation of highly organized bacterial colonies. We combine experimental observations and analysis with continuum modeling and DES to provide a multiscale description of cell colony growth. Our results reveal how cell growth and colony expansion trigger the formation of the orientational (nematic) order in the population, which, in turn, affects the mechanical and biochemical properties of the colony.

3.2 Experimental Design and Results

To explore the biomechanical effects of bacterial colony growth, we used non-motile *E. coli* that possess a rod-like structure with a length-to-diameter ratio that varies between two and five depending on the age of the cell (Fig. 3.1A–C). The cells were loaded into a custom-designed microfluidic device containing a long and narrow open channel ($30\times500\times1$ μm^3) where a monolayer of cells could grow under constant environmental conditions. The colony structure was recorded every 2 min using time-lapse microscopy and subsequently analyzed using specially designed segmentation and tracking software. Further details of the experimental protocol can be found in the Microscopy and Image Processing section of Materials and Methods. After extraction from the images, cell positions and orientations were used to compute coarse-grained density, velocity, and orientation fields. The degree of orientation was characterized by the orientational order parameter, $Q = \sqrt{\langle\cos 2\phi\rangle^2 + \langle\sin 2\phi\rangle^2}$, where ϕ is the angle between the cell axis and the channel axis, and brackets denote averaging over the whole system. This order parameter ranges from 0 for a completely disordered colony to 1 for a colony that is completely aligned.

We characterized colony growth and ordering in an open channel microchemostat (Figs. 3.7 and 3.8). Initially, a small number of randomly oriented cells were spread

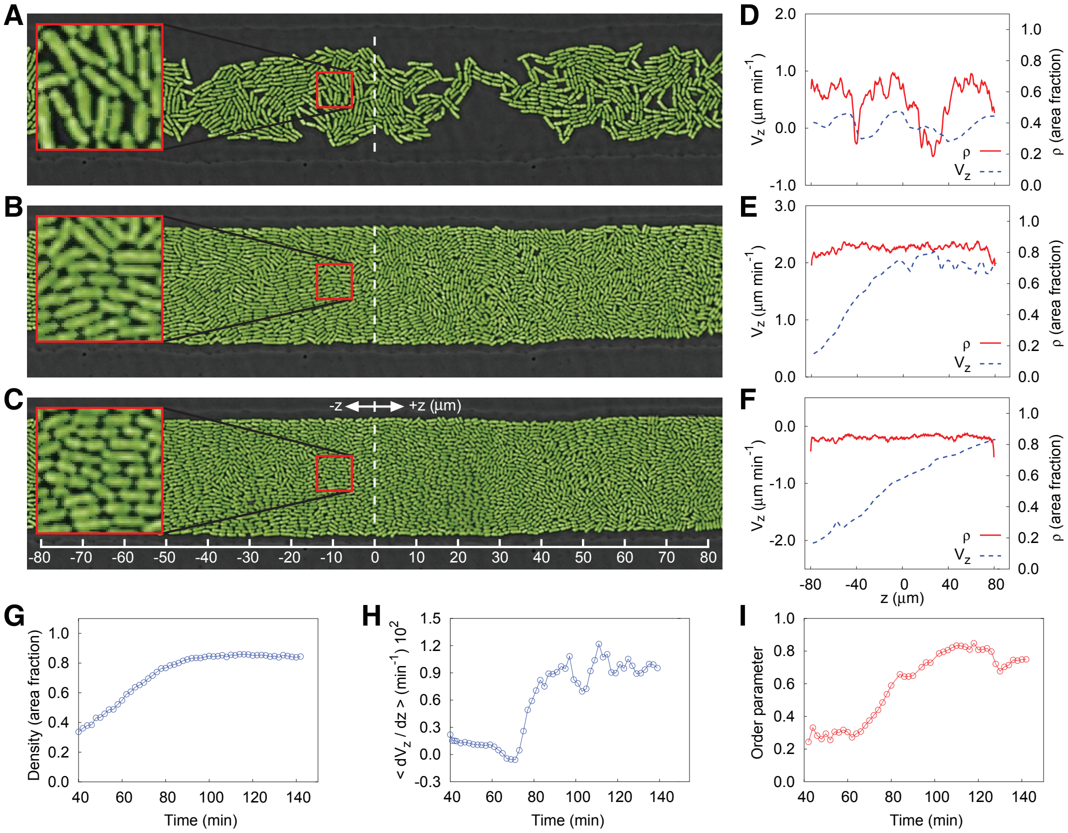

Figure 3.1: Experimental results for bacterial growth and ordering from an evenly distributed, low-density seeding of cells. (**A**–**C**) Three snapshots of *E. coli* monolayer growth and ordering in a pseudo-2D open microfluidic cavity taken at 60, 90, and 138 min from the beginning of the experiment. (**D**–**F**) Velocity and density profiles along the channel corresponding to the snapshots to the left. (**G**–**I**) Time traces of mean density, velocity gradient, and order parameter.

throughout the channel, and a slow flow of medium with negligible drag force on the cells was supplied. Constrained by the narrow 1-μm height of the microfluidic channel and lacking flagella, the bacteria remained motionless during the initial growth phase (Fig. 3.1G, H). After approximately three generations (60 min; Fig. 3.1A, D), the cells began to mechanically push each other and generate a macroscopic expansion flow. At that time, the colony still remained disordered, as demonstrated by the low value of the order parameter ($Q \approx 0.2$; Fig. 3.1I). At a later stage (90 min; Fig. 3.1B, E), the density in the left part of the field of view reached a close-packing regime, so the expansion flow amplified to accommodate cell proliferation. Based on a measurement of the gradient of the flow velocity along the channel ($dV_z/dz \approx 0.023$ min^{-1}), we estimate the cell doubling time at this stage to be $t_d = \ln 2\,(dV_z/dz)^{-1} \approx 30$ min, which agrees well with the typical log-phase division period of *E. coli*. The increasing outgoing flux at this point was accompanied by a rapid orientation of cells along the direction of flow as indicated by the appreciable growth of the order parameter (Fig. 3.1I). Eventually, a quasi-stationary regime was established, with nearly constant density and velocity gradient and a high degree of cell orientation along the channel axis (138 min; Fig. 3.1C, F). At this stage, the expansion velocity gradient had decreased by around half ($dV_z/dz \approx 0.012\,\text{min}^{-1}$), corresponding to a slower cell doubling time of $\sim$60 min. This finding corroborates earlier evidence of the slowing of cell growth rate in response to high mechanical pressure (Shraiman, 2005), although we note that other factors such as a decrease in nutrient concentration or an increase in waste concentration could be acting in conjunction. At this final stage, the cells in the chambers are nematically ordered along the axis of the channel, which coincides with the direction of the expansion flow. Our main conjecture from this experiment is that the nematic ordering of cells is driven by the self-generated growth-induced expansion flow. This is in marked contrast with thermal systems such as liquid crystals and polymers, where nematic ordering is driven by steric exclusion of rod-like molecules and a corresponding entropy maximization (Onsager, 1949).

3.3 Continuum Modeling of Colony Growth and Ordering

To understand the mechanism of cell ordering during colony growth, we first developed a continuum model of the colony dynamics derived from the general equations of nematodynamics (Doi and Edwards, 1986) suitably generalized to include the effects of cell growth and division (see Details of Continuum Modeling section of Materials and Methods). These equations describe the temporal evolution of coarse-grained density, $\rho\left(x, z, t\right)$, velocity, $\mathbf{v} = \left(v_x, v_z\right)\left(x, z, t\right)$, pressure, $p\left(x, z, t\right)$, and tensor order parameter, $\mathbf{Q}\left(x, z, t\right)$, characterizing local cell orientation. We assume that the cell density grows exponentially at a rate α and that this growth does not have a direct effect on local orientation because offspring maintain the orientation of their mother cell just after division. However, the exponential increase in cell mass increases the pressure within the colony, which generates an expansion flow that leads to cell ordering. For flows in long channels, the continuum model may be formulated in terms of dynamical equations for the amplitudes of the coarse-grained fields (model A; see Fig. 3.2 and Details of Continuum Modeling section of Materials and Methods).

To accommodate the constant cellular growth rate, α, the expansion flow in the asymptotic regime must have a longitudinal velocity profile $v\left(z\right) = \alpha z$ (in dimensional form). This velocity profile is driven by a parabolic pressure distribution, $p = \alpha L^2/\mu\left[1 - \left(z/L\right)^2\right]$, where L is the half-length of the channel and μ is the friction coefficient. Thus the pressure in the middle of the channel ($z = 0$) scales as L^2 and for long channels may reach high values. There is experimental evidence corroborating our own observations that high pressure affects cell function and in particular can slow down or stop cell growth (Shraiman, 2005). This effect, in turn, helps to alleviate the pressure buildup in large colonies. To incorporate this effect, we replaced the constant cell growth rate, α, in the model by $\alpha_0\left[1 - \left(p/p_c\right)^2\right]$, with a certain critical value of pressure, p_c, at which cell growth terminates (model B). This model leads to similar

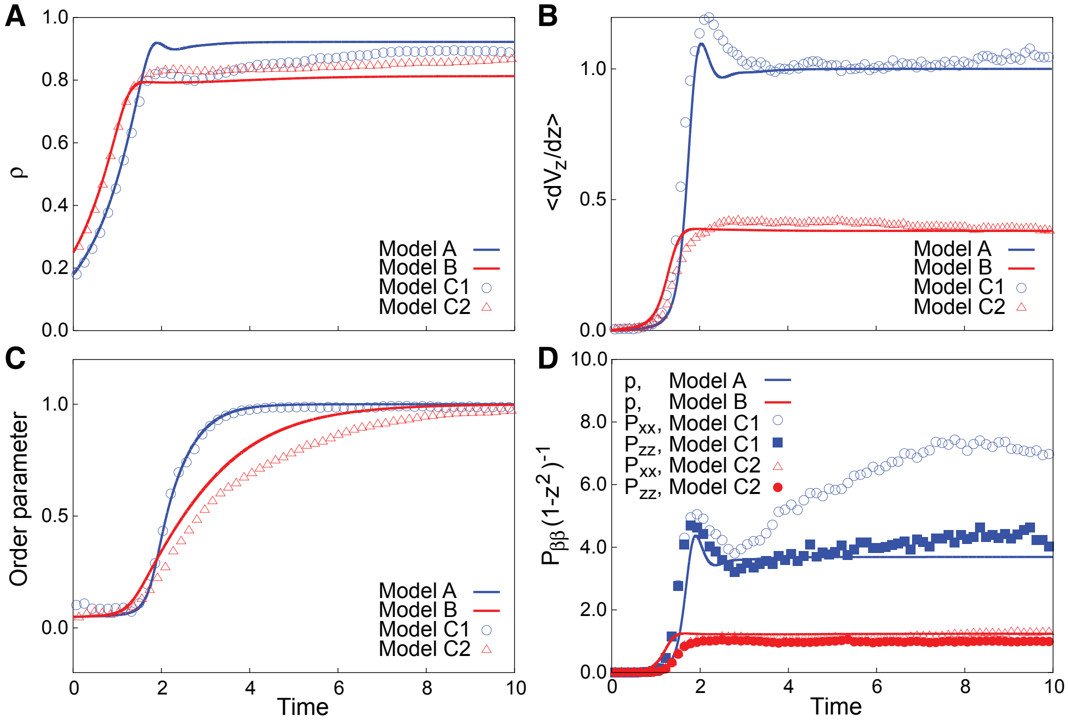

Figure 3.2: Comparison of continuum and DES modeling of the bacterial growth. Shown are time traces of the amplitudes of density (**A**), velocity gradient (**B**), order parameter (**C**), and stress components (**D**) for constant growth rate ($A = 2.0$; models A and C1) and pressure-dependent growth rate ($A = 4.0$; models B and C2). Results of the continuum modeling are indicated by lines, and results of the DES simulations are indicated by symbols.

dynamics; however, saturation occurs at much smaller values of pressure and velocity gradient in the bulk of the colony (Fig. 3.2). We discuss a possible implication of this effect below.

3.4 Discrete Element Simulations of Cell Dynamics

Continuum models aid in understanding the basic biomechanical mechanisms of cell-cell interaction and ordering and can guide our intuition in designing engineered biofilms. However, to make quantitative predictions, a more detailed description of biofilm structure is needed. To augment the experiments and calibrate our continuum models, we carried out detailed DES of the cell dynamics and interactions for constant and pressure-dependent growth rates (models C1 and C2, respectively; see Figs. 3.9 and 3.10 and Details of Discrete Element Simulations section of Materials and Methods).

We used DES to explore the effect of channel length on colony ordering for the constant growth rate condition (model C1; Fig. 3.3). For simulations within a short channel, complete order was established, with almost all cells oriented along the channel (Fig. 3.3A). However, for simulations within a long channel, the population remained in a disordered state characterized by large “swirls” (Fig. 3.3C). This difference can also be seen in velocity profiles obtained by coarse-graining the velocities of individual cells (Fig. 3.3B, D). In Fig. 3.3, arrow color indicates the magnitude of the velocity field, from blue (low) to red (high). Also, we observe that the velocity averaged over the cross section of the cavity is a linear function of the distance from the center of the cavity. This linear elongational flow is consistent with mass conservation, which stipulates that local cell growth must be balanced by mass expansion toward the open ends of the channel, where the resulting velocity gradient is equal to the cell growth rate, α.

Fig. 3.4 illustrates the evolution of the population size, pressure in the middle section, mean velocity gradient, and mean order parameter in DES of colony growth in open channels of different aspect ratios ranging from $A = 2$ to $A = 4$ for the constant growth rate condition (model C1). These plots show the transition from a highly or-

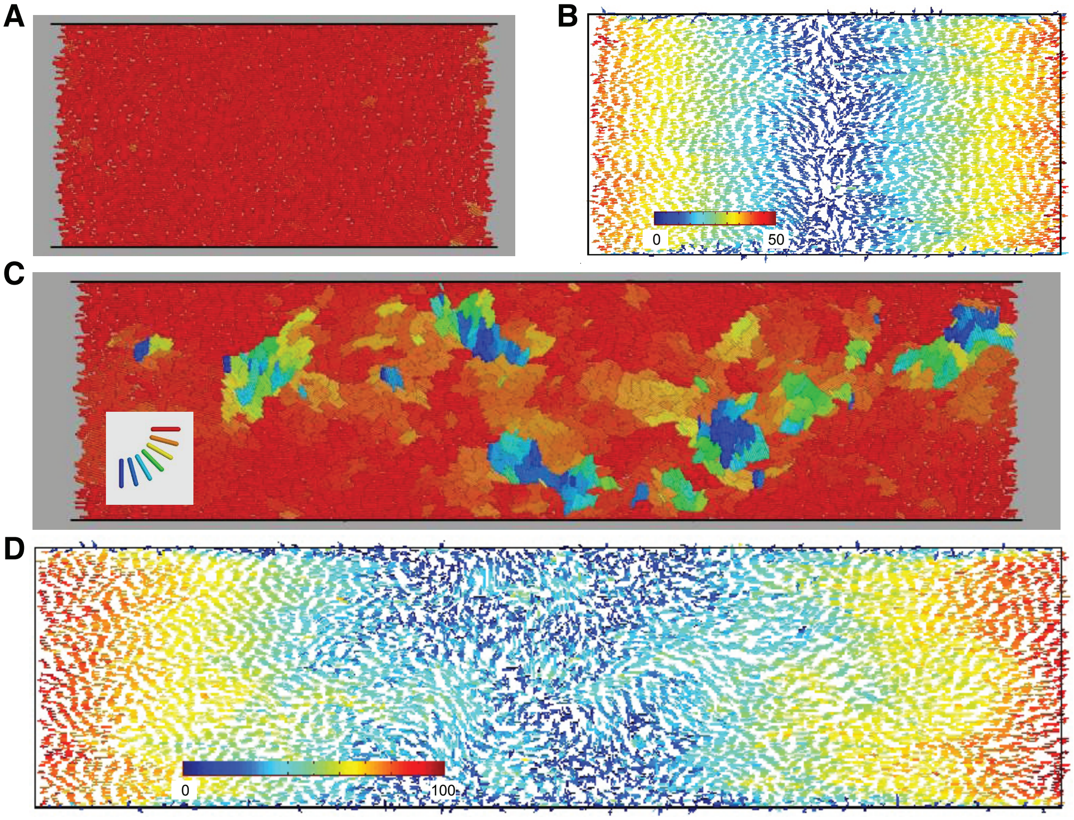

Figure 3.3: DES of the ordering dynamics in channels with different aspect ratios. (**A**) Orientation of individual cells (color-coded) in the system with $A = 2.0$ and a constant growth rate (model C1). (**B**) Velocity field for the same case as in **A**, where unit velocity vectors show the velocity direction for each cell and colors (from blue to red) correspond to the velocity magnitude (from low to high). (**C**) The same as **A**, but for a twice longer system ($A = 4.0$). Defects of the orientation are constantly created in the middle of the channel and advected by the flow toward the open boundaries. (**D**) The same as **B**, but for a twice longer system ($A = 4.0$). The flow is no longer laminar, and there is no apparent correlation between orientation and velocity magnitude.

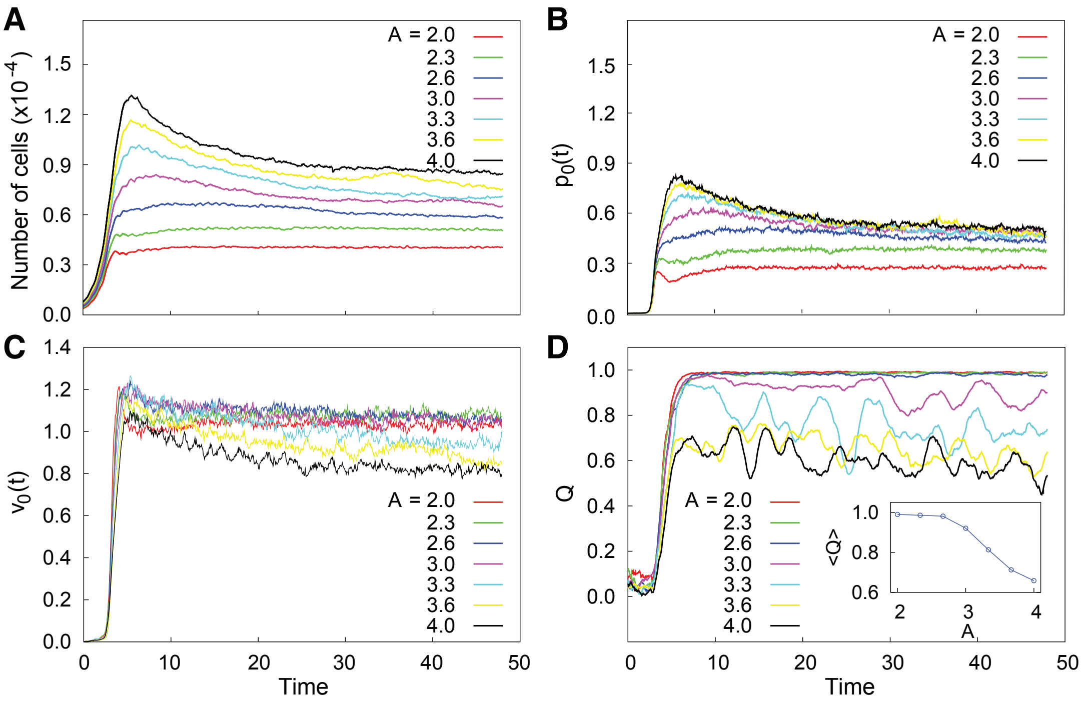

Figure 3.4: DES of bacterial growth for the constant growth rate condition (model C1) in channels with aspect ratios varying from $A = 2$ to $A = 4$. For each aspect ratio, we show the time evolution of the total number of cells within the channel (**A**), the pressure in the middle of the channel (**B**), the mean velocity gradient (**C**), and the averaged order parameter (**D**). (**D Inset**) The decay of the asymptotic value of the order parameter with the aspect ratio, A. Time is measured in units of the inverse growth rate.

dered regime in short channels ($A < 3$) to a partially disordered asymptotic regime in long channels ($A > 3$). Fig. 3.5 depicts the profiles of flow parameters averaged across the channel cross section (velocity, pressure, density, order parameter) plotted against channel length for different system aspect ratios. As seen in Figs. 3.3–3.5, there is a clear transition from a completely ordered stationary regime in short channels ($Q \to 1$) to a partially disordered stationary regime in longer channels with a minimum near the middle of the channel ($Q \approx 0.6 \ldots 0.8$). The nature of this transition is presently unknown but is apparently related to the high values of pressure in the middle of the cavity and the corresponding strong expansion flow. Indeed, in our simulations of a modified system in which the cellular growth rate was not constant but pressure-dependent (model C2), high nematic order was observed in both short and long channels.

To test the validity of the continuum modeling, we compared the results of the DES (models C1 and C2) with models A and B. Fig. 3.2 shows the results of this comparison for simulations in a short channel with constant growth rate (models A and C1) and in a long channel with pressure-dependent growth rate (models B and C2). Except for replacing the constant growth rate, α, by $\alpha_0 \left[1 - (p/p_c)^2\right]$, all parameters were kept the same. In both cases, the continuum model provides a good description of the colony dynamics, indicating that the cell density grows at a similar rate and saturates near the close-packed limit (Fig. 3.2A). However, both the pressure and the ensuing expansion flow in the pressure-dependent growth case (models B and C2) are almost two times smaller (Fig. 3.2B, D), and the cellular ordering is proportionally slower (Fig. 3.2C). Interestingly, pressure-dependent growth leads to the isotropization of local stresses, as evidenced in Fig. 3.2D. This effect may be attributed to the ability of slower-growing cells to better adjust to local contact stresses.

In natural environments, bacterial colonies often grow from a few cells or even a single cell. In this case, the colony has a well-defined boundary that expands during cell growth. Although it is a more difficult system for continuum modeling, we performed experiments and DES to test the ordering mechanism within colonies starting from a localized initial condition rather than a uniformly seeded condition. Our results show

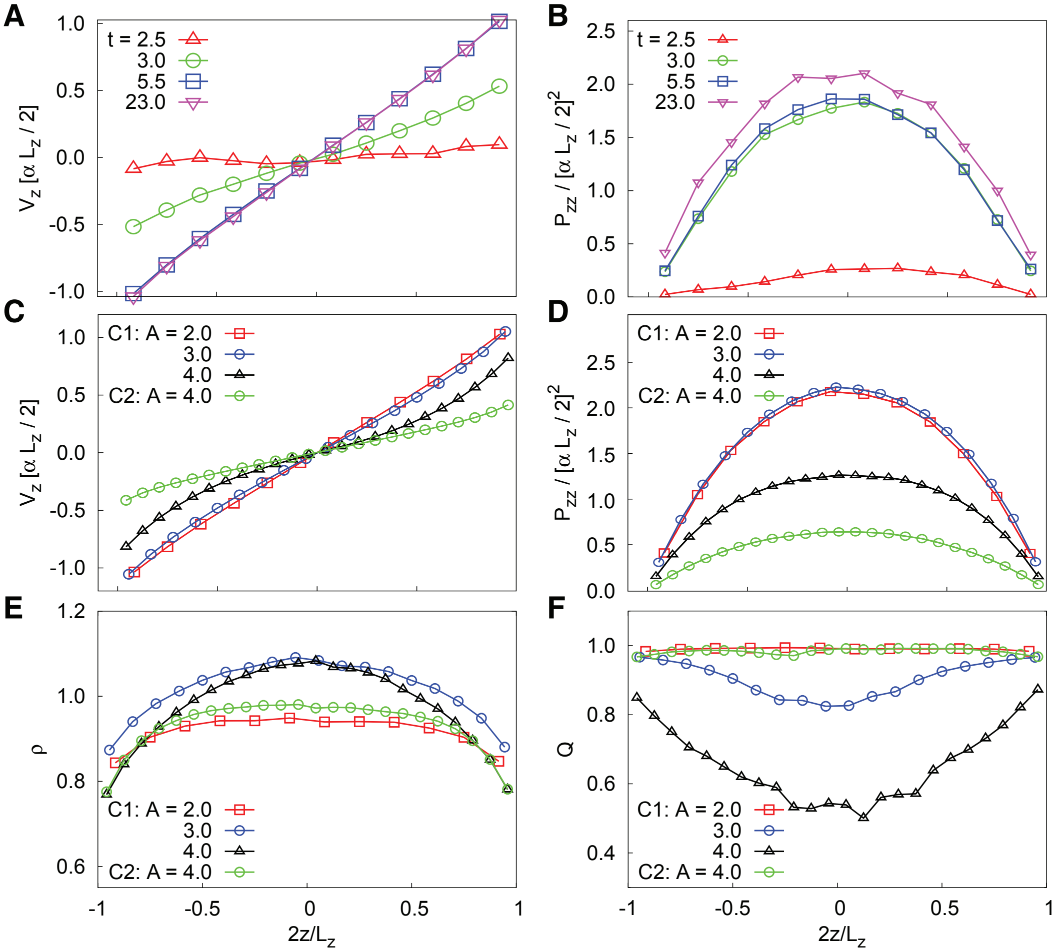

Figure 3.5: Spatiotemporal dynamics of bacterial growth generated using DES. (**A**, **B**) Evolution of profiles of velocity and pressure along the channel in the short system ($A = 2$). (**C**–**F**) Stationary profiles of the velocity, pressure, density, and order parameter for channels of different aspect ratios: $A = 2, 3, 4$ for the case of constant growth rate (model C1) and $A = 4$ for the case of pressure-dependent growth rate (model C2).

that rapid ordering occurs in this case as well (see Fig. 3.6). Because colony dynamics are essentially nonuniform, a proper continuum description should go beyond the ODE model presented here. We anticipate that many interesting issues will arise naturally in this context, including ordering front propagation, coarsening, and defect formation.

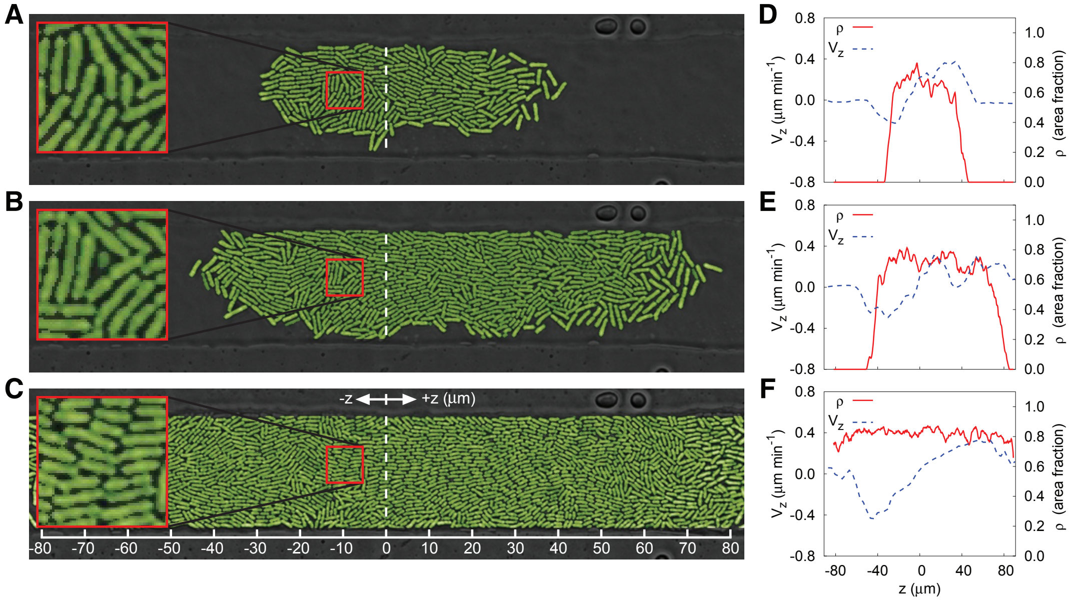

Figure 3.6: Experimental results for bacterial growth and ordering from a single initial cell. (**A**–**C**) Three snapshots of *E. coli* monolayer growth and ordering in a pseudo-2D open microfluidic cavity taken at 169, 198, and 248 min from the beginning of the experiment. (**D**–**F**) Velocity and density profiles along the channel corresponding to the snapshots in **A**–**C**.

3.5 Materials and Methods

3.5.1 Microfluidic Device Design and Fabrication

The design of the microfluidic device used in these experiments was based on the Tesla microfluidic chamber design developed by Cookson*, Ostroff*, Pang*, Volfson, and Hasty (2005, *equal contribution) for use with *S. cerevisiae*. The original TμC design implemented the classic Tesla diode loop (Tesla, 1920; Duffy et al., 1999; Bendib and Français, 2001) modified for imaging a monolayer culture of growing yeast cells. We made several modifications to adapt it for application to *E. coli* (Fig. 3.7A). First, we lowered the height of the diode side-arm, which forms the shallow trapping region capable of constraining a population of cells to a common focal plane. For imaging yeast cells, the cell-trapping region was fabricated to be 4 μm high, which is the approximate diameter of a yeast cell. For imaging *E. coli* cells, we lowered this height to 1 μm, which is the approximate diameter of a cylindrical *E. coli* cell of the K-12 MG1655 strain. To maintain the proper resistance ratio for flow splitting, we also lowered the delivery channel height from 12 μm to 3 μm. Last, we divided the cell-trapping region into three parallel channels for simultaneous observation of isolated colonies. The width of each parallel chamber was limited to 30 μm so as not to exceed the width/height aspect ratio of 30 for PDMS and risk structural collapse of the chamber "ceilings."

Microfluidic devices were fabricated in the UCSD Integrated Technology Laboratory (ITL) using standard soft lithography techniques (Duffy et al., 1999; Unger et al., 2000; Whitesides et al., 2001; Sia and Whitesides, 2003). Photomasks were drawn in FreeHand MX (Macromedia Inc.; San Francisco, CA), printed onto transparency film at high resolution (Output City; Poway, CA), and mounted to clean borosilicate glass plates (McMaster-Carr; Los Angeles, CA). Master molds were created by first spin-coating SU-8 2000 negative photoresists (MicroChem Corp.; Newton, MA) upon clean silicon wafers to appropriate depths using a Headway PWM32 programmable spinner (Headway Research Inc.; Garland, TX) and then patterning with a UV contact mask aligner (HTG; San Jose, CA). After all photolithographic steps were completed, SU-8 feature heights were verified using a DEKTAK 3030ST profilometer (Sloan Technology Corp.; Santa Barbara, CA), and treated with vaporous CTMS for 5–10 min. Replica molds were created from master molds by mixing PDMS (Sylgard 184; Dow Corning; Midland, MI) in a 10:1 (elastomer base/curing agent) ratio, degassing in a vacuum desiccator at $\sim$-1 atm for 1 h, and curing in place over the master at 80°C for 2 h. After removal of the PDMS monolith, chips were sectioned, bored at the fluidic ports, and cleaned with Scotch 810 office tape. Finally, chips were rinsed with methanol of a purity

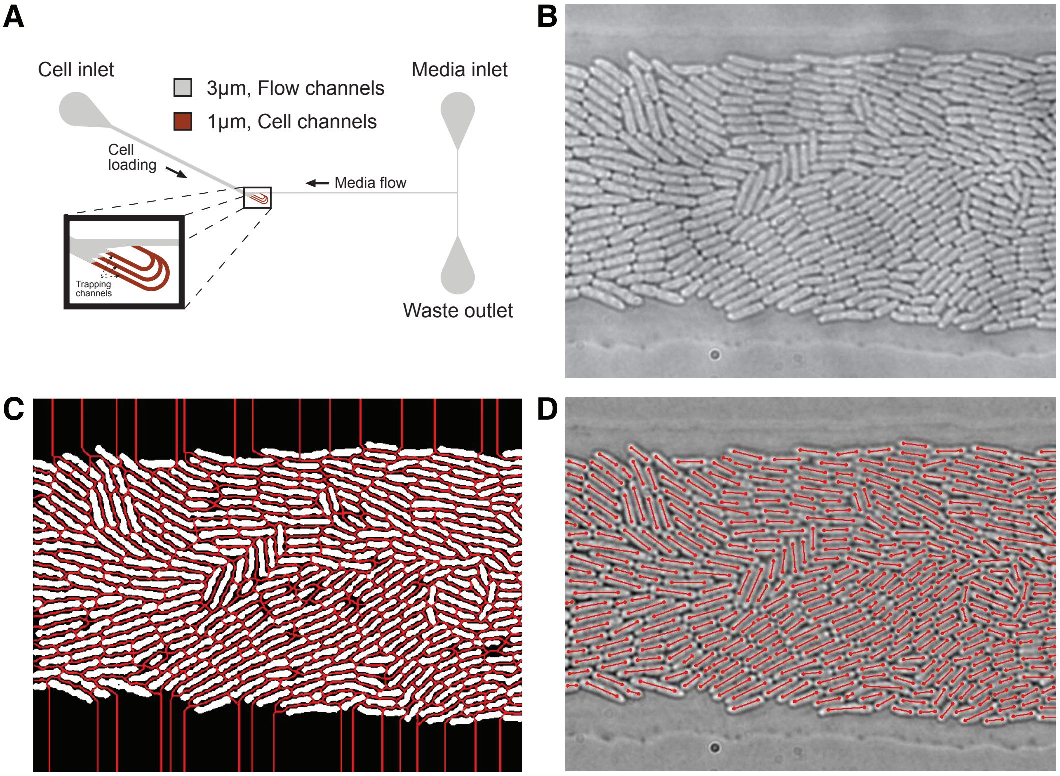

Figure 3.7: Microfluidic device design and image processing. (**A**) Schematic diagram of the TμC microfluidic device adapted to study *E. coli* ordering in open channels. (**B–D**) Image processing steps: original brightfield image (**B**), construction of a binary mask and watershedding (**C**), and recognition (**D**). The lengths of red segments are proportional to the sizes of cells.

appropriate for high-pressure liquid chromatography (HPLC) and permanently bonded to clean 24×40 mm^2 no. $1\frac{1}{2}$ coverslips (Corning Inc.; Corning, NY) via exposure to O_2 plasma at 30 W for 1 min in a 500-II Plasma Asher (Technics Plasma; Danville, CA).

3.5.2 Microfluidic Device Characterization

We performed two experiments to measure the time scales of nutrient distribution over the field of view in our microfluidic channel. In the first experiment, we introduced Sulforhodamine 101, a red fluorescent dye with a MW similar to that of the largest cell nutrient, to the flow of medium at a precise time and measured its diffusion into an empty cell-trapping region. We recorded the fluorescence averaged both within one region in the 3-μm-high bypass channel and within three distinct regions in the cell-trapping area (left cyan, middle orange, and right red boxed regions in Fig. 3.8) distributed over the field of view of the original experiment (green boxed region in Fig. 3.8). We observed uniform distribution of the dye throughout the field of view within 2–3 min after introduction (Fig. 3.8A, C). We also observed a slow upward trend in concentration after the fast initial transient, which was evidently caused by variation in dye concentration within the tall bypass channel. Indeed, after rescaling the fluorescence signal in the bypass channel by a factor of 1:2.5, it matched the fluorescence signal within the cell-trapping region very well. We attribute the observed deviation in the scaling coefficient from the nominal ratio of depths for short and tall channels (1:3) to the nonlinear relationship between the depth of a layer and its integral optical fluorescence.

To examine any difference in diffusion time scales in a full channel, we next repeated this experiment in a chamber packed with cells. Although our intention was to conduct this experiment at the fully packed limit, some empty pockets of medium remained in the cell-trapping channels due to bulk cell flow (Fig. 3.8B, D). In this experiment, fluorescence measured within the regions filled with cells was $\sim$60% smaller than within the empty regions of the channel. This was to be expected, because a large volume fraction of the channels is filled with nonfluorescing cells. Despite the presence

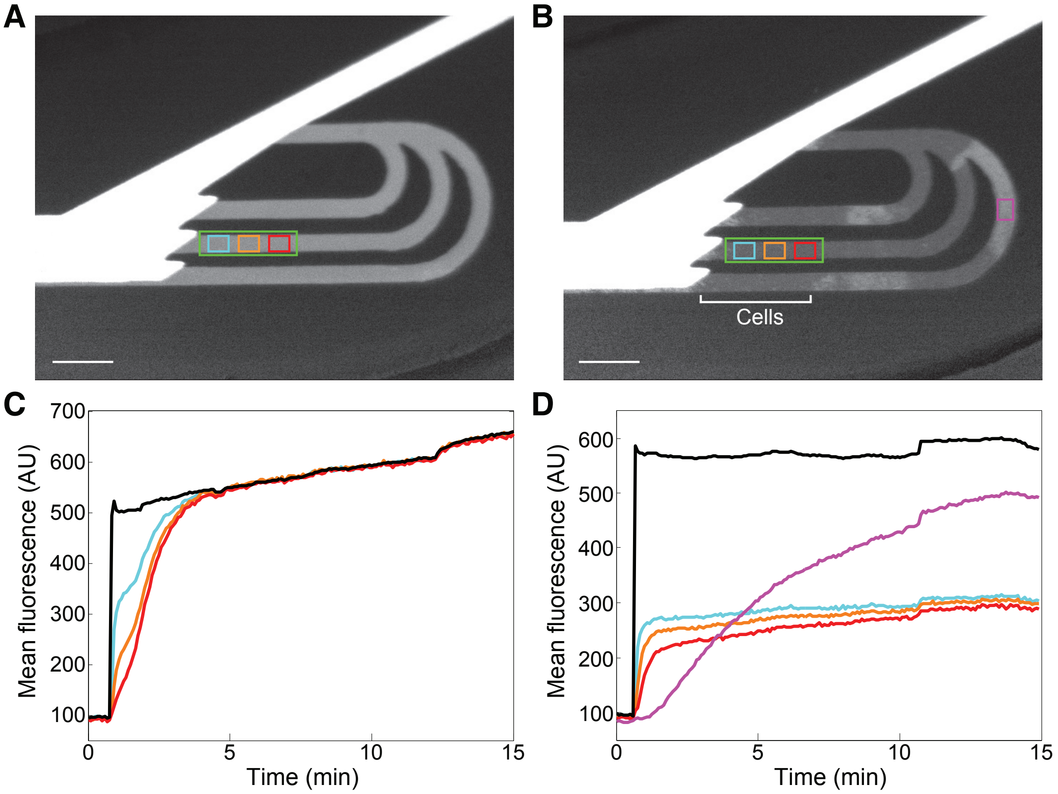

Figure 3.8: Experimental results for the diffusion of fluorescent dye within the chamber. (**A**, **B**) Snapshots of fluorescence after dye propagation throughout the cell-free system (**A**) and the cell-packed system (**B**). Fluorescence is brighter in the deep (3 μm) bypass channel but still nearly uniform in the shallow (1 μm) cell-trapping area. Scale bars, 100 μm. (**C**, **D**) Time-series plots of fluorescence averaged over identical areas in the bypass channel (black) and in three regions (cyan, orange, and red boxes) of the experimental field of view (green box) after dye introduction. Intensity in the bypass channel has been rescaled by a factor of 1:2.5 to match the intensity of dye in the empty cell-trapping area. Additionally, a time series of the averaged intensity in an empty pocket of the cell-trapping region (magenta box in **B**) is shown in **D** in magenta.

of the cells, the dye distribution again quickly became nearly uniform within the field of view (after $\sim$5–10 min; Fig. 3.8B, D), indicating fast nutrient delivery to the cells. Additionally, we took advantage of the empty regions in this experiment to compare the fluorescence in an empty channel region with the fluorescence in the tall bypass channel region (rescaled using the same 1:2.5 ratio as in the empty channel experiment). As Fig. 3.8D shows, these two curves approach each other after $\sim$15 min. The time to reach equilibrium is longer in this case because the selected empty area is significantly further away from the inlet than our typical experimental region.

In summary, we confirmed through experimentation that the volume concentration of nutrients in the working area becomes uniform on a time scale of 5–15 min for both empty and full channels, which is much faster than the time scale of colony development. Thus, the growth rates of our experimental colonies should not be limited by poor nutrient delivery.

3.5.3 Microscopy and Image Processing

Image acquisition was performed on a Diaphot TMD epifluorescent inverted microscope (Nikon Instruments Inc.; Tokyo, Japan) outfitted with a ProScan II XY-motorized stage with fine focus control (Prior Scientific Inc.; Rockland, MA) and Uniblitz VS35 high-speed shutters (Vincent Associates; Rochester, NY). Images were acquired using an Orca-ER cooled CCD camera (Hamamatsu Photonics; Hamamatsu, Japan) and a custom positioning and multispectral acquisition application written in LabVIEW (National Instruments; Austin, TX).

In each experiment, a microfluidic device was mounted to the stage and wetted using a solution of 0.1% v/v TWEEN 20 surfactant (Sigma-Aldrich; St. Louis, MO) in LB-Miller formulation lysogeny broth (LB) medium. For optimal growth, device temperature was maintained at 37°C by flowing heated water through deep thermal channels fabricated into the device. Cells were loaded into the device from the cell port by directing high flow both from the cell port and the media port to the waste port. Upon trapping a single cell in each channel, flow past the cell chamber was reversed and slowed to 1–2 μm s^{-1} such that fresh nutrients were delivered from the media port via a combination of diffusion and advection without physically disturbing the cells. Flow was consistently directed from the media port throughout the loading and running processes to prevent contamination of the medium source. During run time, images of cell growth were collected at ×100 in the transmitted channel every 2–3 min over an experimental duration of ~4–6 h. To capture a complete profile of the system at each time point, three slightly overlapping images were acquired for subsequent stitching into a 1×3 montage. High magnification provided a large number of pixels per cell to aid in image segmentation, while scanning allowed the imaging of many cells. Proper focus was maintained throughout each experiment via manual adjustment.

After each imaging session, a complete profile of the system at each time point was assembled by stitching together the three overlapping images. For each of these merged images, the positions and orientations of individual cells were determined using a custom image segmentation software suite written in IDL (ITT Visual Information Solutions; Boulder, CO). Each composite image was processed using standard grayscale morphology techniques as reported by Cookson*, Ostroff*, Pang*, Volfson, and Hasty (2005, *equal contribution). The major steps of the recognition process are shown in Fig. 3.7B–D. To determine the coarse-grained velocity profiles averaged across the channel, we used the standard PIV technique based on the minimum quadratic difference (MQD) method (Gui and Merzkirch, 1996), followed by filtering using the local signal-to-noise ratio (Sveen and Cowen, 2004).

3.5.4 Details of Continuum Modeling

Constant Growth Rate in 1D (Model A)

The continuum description of cell ordering is similar in spirit to the phenomenological Landau-de Gennes theory developed for dense liquid crystals and polymeric solutions (Doi and Edwards, 1986). In the theory of liquid crystals, the continuous description of nematics is typically based on the equations for the director field and the velocity field (de Gennes and Prost, 1993). Such a description works well below the critical point and when the scalar order parameter is everywhere close to unity. However, close to the isotropic-nematic transition, the magnitude of the order parameter changes significantly, and more general equations of "nematohydrodynamics" incorporating the orientational order parameter are used (Olmsted and Goldbart, 1992). Here, we adopt this description with some important modifications resulting from the differences between rod-like molecules and macroscopic rod-like cells. One such difference is that cells are much less influenced by thermal fluctuations, and accordingly, free energy minimization plays a minor role in the dynamics of the order parameter. Second, unlike molecules, living cells grow and divide, and this process profoundly alters the collective dynamics.

For the description of the expansion flow in a straight open channel, we can assume that all fields depend only on time and coordinate $-L < z < L$ along the channel. Therefore, the full set of equations can be reduced to a 1D model:

$$\begin{aligned} \partial_t \rho + \partial_z (\rho v) &= \alpha \rho && (3.1) \\ \partial_t q + v \partial_z q &= B \left(1 - q^2\right) \partial_z v && (3.2) \\ \partial_t (\rho v) + v \partial_z (\rho v) &= -\partial_z p - \mu \rho v, && (3.3) \end{aligned}$$

where $q \equiv Q \equiv Q_{zz}; v \equiv v_z$; α is the constant cell growth rate; μ is the bottom friction coefficient (we assume that the friction force is proportional to the cell velocity and independent of the orientation); the dimensionless parameter B describes the rate of ordering driven by the velocity gradient; and the pressure, p, satisfies the constitutive relation,

$$p = P \exp\left[s\left(\rho - \rho_c\right)\right]. \tag{3.4}$$

The pressure, p, is density-dependent, being exponentially small for $\rho < \rho_c$ (parameter s is large) and exponentially large for $\rho > \rho_c$. The close-packing density, ρ_c, is itself a function of the order parameter, Q, where more ordered populations have higher close-packing densities. We model this dependency by the relation, $\rho_c = \rho_c^d + \left(\rho_c^o - \rho_c^d\right) Q^2$, where ρ_c^d and ρ_c^o are critical densities of disordered and ordered rods, respectively.

The solution in which the density, $\rho\left(t\right)$, and the order parameter, $q\left(t\right)$, are independent of z; the velocity is a linear function of z ($v = v_0\left(t\right) z$); and the pressure is parabolic ($p = p_0\left(t\right)\left[1 - \left(z/L\right)^2\right]$) satisfies Eqns. 3.1–3.3 at all times. The normalized "magnitudes" of this solution, ρ, v_0, q, and p_0, satisfy the set of three ODEs:

$$\dot{\rho} = \rho\left(\alpha - v_0\right) \tag{3.5}$$

$$\dot{q} = B\left(1 - q^2\right) v_0 \tag{3.6}$$

$$\dot{v}_0 = 2\rho^{-1}L^{-2}p_0 - \left(\alpha + \mu\right) v_0. \tag{3.7}$$

According to this set of equations, initially the density grows exponentially with rate α while the pressure remains low and the velocity gradient is absent. Once the density approaches the random close-packing density, ρ_c, the pressure begins to rise rapidly, and it produces a rapidly increasing expansion flow (Fig. 3.2). This flow removes excess cells from the channel and equilibrates the density at near the close-packed limit. The expansion flow orients the cells along the channel axis, which in turn increases the close-packing density. Eventually, the system reaches a stationary regime with uniform density and velocity gradient, where cell growth is exactly balanced by the outgoing flux of cells. In this regime, $q = 1$ and $\rho \approx \rho_c^o$. The velocity gradient, v_0, equals α, and the corresponding pressure, p_0, equals $\left(\alpha + \mu\right)\rho_c^o \alpha L^2/2$. According to our model, cell density grows exponentially in the absence of flow and may only saturate when the velocity gradient reaches a value equal to the growth rate of the cells. For long channels, the establishment of the stationary velocity profile takes a long time, as the flow velocity has to overcome friction to reach high values near the open ends of the channels. This leads to the "overshoot" of the density, which then gradually diminishes as the velocity gradient increases.

Because the pressure scales as the square of the length of the channel, for long channels it reaches very high values in the middle of the colony. In fact, this high pressure behavior is mitigated by the cell growth saturation. To simulate this effect, we used a modification of the growth model described below.

Pressure-Dependent Growth Rate in 1D (Model B)

ODE model B has the same functional form (Eqns. 3.5–3.7); however, the growth rate, α, is assumed to be a function of pressure, $\alpha = \alpha_0 \left[1 - (p/p_c)^2\right]$, such that cell growth terminates when the pressure reaches a critical value, p_c (Shraiman, 2005). In fact, the pressure is not uniform across the channel; therefore the growth of cells will first saturate in the middle where the pressure is maximal, followed by propagation toward the channel periphery. However, in this simplified model we ignore this subtlety. It turns out that this approximation works quite well in describing the results of the DES (Fig. 3.2).

3.5.5 Details of Discrete Element Simulations

Generalization of the DES Algorithm

To model the proliferation of cells in a microfluidic environment, we generalized an algorithm that we developed earlier to describe the dynamics of granular rods (Volfson et al., 2004). This algorithm is based on the well-known method of molecular dynamics (MD) simulations (Rapaport, 2004), which are used in different areas of statistical physics. The main idea of the method is to follow the dynamics of the individual "particles" that constitute the system under study. In the case of a gas, these particles are molecules, and in the case of a granular material, each particle represents a single grain.

To simulate the motion, growth, and interaction of bacteria, we model every cell as a spherocylinder (circular cylinder with spherical caps) of diameter, d, total length, $l + d$, mass, m, and moment of inertia, I. In our 2D simulations, each cell has two translational and one rotational degree of freedom. The motion of a cell is affected by both elastic and frictional forces exerted by interactions with other cells and the walls of the microfluidic chamber. To compute the elastic forces, we use a variant of the soft particle MD simulation technique (Schäfer et al., 1996). The interaction between overlapping spherocylinders is modeled as the interaction between viscoelastic virtual spheres of diameter d centered at the closest points between the axes of the spherocylinders such that the cylinders are in contact whenever the virtual spheres are. Frictional forces and torques simulating cellular interaction with the top and bottom surfaces in a shallow microfluidic channel are proportional to the cell linear and angular velocities, respectively. The normal forces between virtual spheres are computed using the Hertzian model, and the tangential frictional forces are computed using dynamic Coulomb friction.

We model cellular growth and division by exponentially extending the length of each cell in time as $\exp(\alpha t)$ until it reaches a maximal length, l_m, which is drawn from a Gaussian distribution near a fixed length, l_0, with a coefficient of variation of 0.3. At division, a mother cell is replaced by two collinear daughter cells with lengths taken from a peaked distribution near $l_m/2$ to avoid spurious synchronization of cell division events. These daughter cells then continue to grow independently, with the repeated process of growth and division resulting in an exponential growth of the population.

Simulation Results (Models C1 and C2) and Comparison to Continuum Modeling

Cells were initially distributed uniformly in the cavity at low packing density ($\rho_0 = 0.02$) and random orientation. We imposed open boundary conditions at the ends of the channel so that cells reaching these ends were instantaneously removed from the system.

In model C1, the cell growth rate, α, was fixed as in model A, and in model C2, the growth rate was scaled by the total pressure acting on each cell from its neighbors as in model B. Coarse-graining the positions, orientations, and velocities of individual cells, we analyzed the dynamics of the density, velocity, and order parameter fields. Representative profiles of longitudinal velocity, pressure, density, and order parameter are shown in Fig. 3.5 for different times from the beginning of the simulation and for different values of the aspect ratio, for both the constant growth rate condition (model C1) and the pressure-dependent growth rate condition (model C2).

We also used DES to fit the parameters of the continuum model (Fig. 3.2). Once the parameters were established, we compared DES with model predictions for the evolution of the density, velocity, order parameter, and pressure with constant and pressure-dependent growth starting from a low-density, disordered initial condition.

Finally, we present snapshots of the population structure and velocity fields obtained in DES at three stages of colony growth and ordering. Figs. 3.9 and 3.10 depict the velocity vector fields and cell orientation maps for the constant (model C1) and pressure-dependent (model C2) cell growth cases, respectively. Simulations were performed for a long channel with aspect ratio, $A = 4.0$, starting from the low packing fraction, $\rho_0 = 0.02$. Snapshots correspond to times $t = 4.3\tau$ min (Figs. 3.9A and 3.10A), $t = 5.7\tau$ min (Figs. 3.9B and 3.10B), and $t = 16.4\tau$ min (Figs. 3.9C and 3.10C). Clearly, pressure-dependent growth results in a higher degree of ordering and a reduction in observed "swirls."

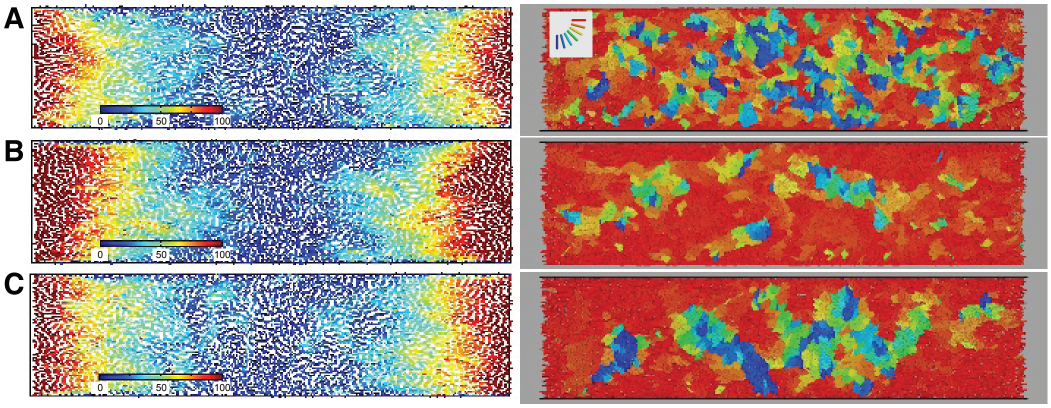

Figure 3.9: DES of bacterial growth in a colony with a constant growth rate (model C1) and a channel aspect ratio of $A = 4.0$. Snapshots of the colony structure in the system show velocity vector fields (**Left**) and cell orientation maps (**Right**). (**Left**) Each vector corresponds to the instantaneous translational velocity of a cell, where length is normalized for visual clarity and colors (from blue to red) correspond to magnitude (from low to high). (**Right**) Cell color denotes orientation relative to the channel axis, from blue (perpendicular) to red (parallel). (**A**) $t = 4.3\tau$ min. (**B**) $t = 5.7\tau$ min. (**C**) $t = 16.4\tau$ min. $\tau = 20$ min is the division time.

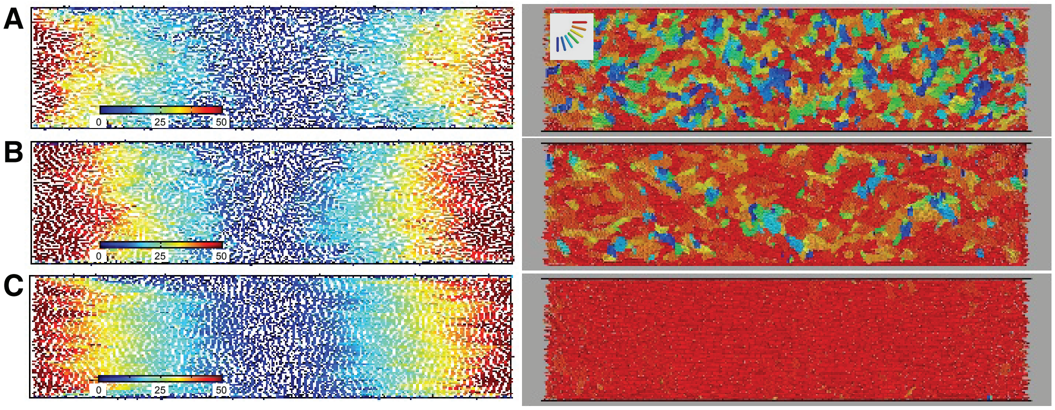

Figure 3.10: DES of bacterial growth in a colony with a pressure-dependent growth rate (model C2) and a channel aspect ratio of $A = 4.0$. Snapshots of colony structure are synchronous to the system shown in Fig. 3.9, but with $\alpha_0 = 0.7128$ and $p_c = \sigma_{xx} + \sigma_{zz} = 2 \times 10^5$.

3.6 Acknowledgements

Chapter 3 contains material originally published as Volfson, D.*, Cookson, S.*, Hasty, J., and Tsimring, L. S., 2008: Biomechanical ordering of dense cell populations. *Proc. Natl. Acad. Sci. U. S. A.*, **105**(40), 15346-51. (*equal contribution). Copyright permission to republish here was granted by the National Academy of Sciences of the USA.

Chapter 4

A Fast, Robust, and Tunable Synthetic Gene Oscillator

4.1 Introduction

Following our success in adapting microfluidics to study biomechanical ordering of *E. coli* in dense monolayer colonies, we used the modified TμC device developed by Volfson*, Cookson*, Hasty, and Tsimring (2008, *equal contribution) and flow cytometry to investigate expression dynamics within single bacterial cells carrying a novel genetic oscillator constructed in the Hasty Laboratory. Our extensive characterization of this synthetic regulatory circuit follows.

One defining goal of synthetic biology is the development of engineering-based approaches that enable the construction of gene-regulatory networks according to "design specifications" generated from computational modeling (Hasty et al., 2002a,b; Tyson et al., 2003; Sprinzak and Elowitz, 2005; Endy, 2005; Andrianantoandro et al., 2006). This approach provides a systematic framework for exploring how a given regulatory network generates a particular phenotypic behavior. Several fundamental gene circuits have been developed using this approach, including toggle switches (Gardner et al., 2000) and oscillators (Elowitz and Leibler, 2000; Atkinson et al., 2003; Fung et al., 2005), and these have been applied in new contexts such as triggered biofilm development (Kobayashi et al., 2004) and cellular population control (You et al., 2004). Here we describe an engineered genetic oscillator in *E. coli* that is fast, robust, and persistent, with tunable oscillatory periods as fast as 13 min. The oscillator was designed using a previously modeled network architecture comprising linked positive and negative feedback loops (Hasty et al., 2002a; Barkai and Leibler, 2000). Using a microfluidic platform tailored for single-cell microscopy, we precisely control environmental conditions and monitor oscillations in individual cells through multiple cycles. Experiments reveal remarkable robustness and persistence of oscillations in the designed circuit; almost every cell exhibited large-amplitude fluorescence oscillations throughout observation runs. The oscillatory period can be tuned by altering inducer levels, temperature, and the growth medium. Computational modeling demonstrates that the key design principle for constructing a robust oscillator is a time delay in the negative feedback loop, which can mechanistically arise from the cascade of cellular processes involved in forming a functional transcription factor. The positive feedback loop increases the robustness of the oscillations and allows for greater tunability. Examination of our refined model suggested the existence of a simplified oscillator design without positive feedback, and we construct an oscillator strain confirming this computational prediction.

4.2 Circuit Design

The synthetic gene oscillator is based on a previously reported theoretical design (Hasty et al., 2002a) and was constructed using *E. coli* components (Fig. 4.1A). The hybrid promoter, $\mathrm{p}_{\mathrm{lac/ara\text{-}1}}$ (Lutz and Bujard, 1997), is composed of the activation operator site from the *araBAD* promoter placed in its normal location relative to the transcription start site, and repression operator sites from the *lacZYA* promoter placed both upstream and immediately downstream of the transcription start site. It is activated by the AraC protein in the presence of arabinose and repressed by the LacI protein in the absence of isopropyl β-D-1-thiogalactopyranoside (IPTG). We placed the *araC*, *lacI*, and *yemGFP*

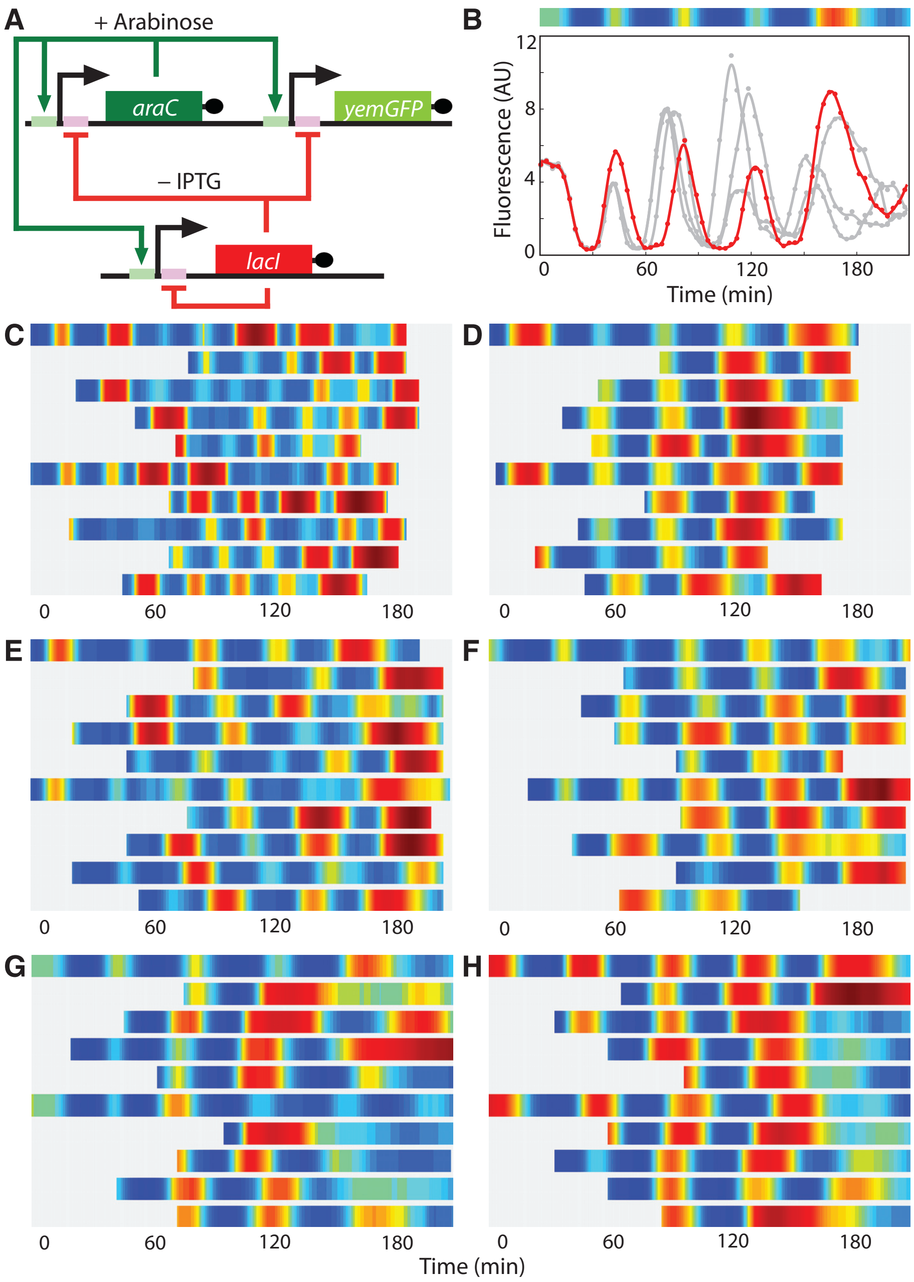

Figure 4.1: Single-cell fluorescence trajectories for the dual-feedback oscillator. (**A**) Network diagram of the dual-feedback oscillator. A hybrid promoter, $p_{\mathrm{lac/ara\text{-}1}}$, drives transcription of *araC* and *lacI*, forming positive and negative feedback loops. (**B**) Single-cell fluorescence trajectories induced with 0.7% arabinose and 2 mM IPTG. Points represent experimental fluorescence values, and solid curves are smoothed by a Savitsky-Golay filter (for unsmoothed trajectories, see Fig. 4.9). The trajectory in red corresponds to the density map above the graph. Density maps for trajectories in gray are shown in **G**. (**C**–**H**) Single-cell density map trajectories for various IPTG conditions ((**C**) 0 mM IPTG; (**D**) 0.25 mM; (**E**) 0.5 mM; (**F**) 1 mM; (**G**) 2 mM; (**H**) 5 mM).

(monomeric yeast-enhanced green fluorescent protein) genes under the control of three identical copies of $p_{\text{lac/ara-1}}$ to form three co-regulated transcription modules (see Plasmid Construction section of Materials and Methods). Hence, activation of the promoters by the addition of arabinose and IPTG to the medium results in transcription of each component of the circuit, and increased production of AraC in the presence of arabinose results in a positive feedback loop that increases promoter activity. However, the concurrent increase in production of LacI results in a linked negative feedback loop that decreases promoter activity, and the differential activity of the two feedback loops can drive oscillatory behavior (Hasty et al., 2002a; Barkai and Leibler, 2000).

4.3 Experimental Results

The oscillator cells (denoted JS011) exhibited ubiquitous fluorescence oscillations over the entire run time of each experiment (at least 4 h). For example, at 0.7% w/v arabinose and 2 mM IPTG, more than 99% of the cells showed oscillations with a period of approximately 40 min (Fig. 4.1B, G; Table 4.1; and Supplementary Movie 4.1). The highly dynamic nature of the oscillator components is shown by the rapid decay of yemGFP signal, which drops from peak to trough in less than 10 min (Fig. 4.1B). The oscillatory phase was heritable between daughter cells, which resulted in synchronized oscillations in areas of the microcolony derived from a common cell. This synchrony was limited to a few periods, presumably owing to oscillatory phase diffusion. We used a microfluidic device with a laminar boundary switch upstream of the growth chamber to investigate the initiation of synchronized oscillations (Fig. 4.8C, D). Cells grown in the absence of inducer initiated oscillations in a synchronous manner on the addition of inducer (Supplementary Movie 4.10), which suggested the possibility of using flow cytometry to characterize the oscillator further. Flow cytometry of samples continuously collected from a culture in logarithmic growth that had been induced with 0.7% arabinose and 2 mM IPTG showed oscillations in mean cell fluorescence (Fig. 4.12). Induction of oscillation was very quick (less than 5 min) and initially well-synchronized.

The amplitude of these bulk oscillations decayed as the experiment progressed, as expected from the desynchronization of individual cells in the colony (see Flow Cytometry section of Materials and Methods). However, the period obtained from the flow cytometry method (green data points in all figures) compared favorably to that obtained from single cells using microscopy (red data points in all figures).

The oscillator was extremely robust over an extensive range of inducer conditions and temperatures. At 0.7$\%$ arabinose and 37°C, almost every observed cell oscillated at all IPTG concentrations examined (Fig. 4.1B–H; Table 4.1; and Supplementary Movies 4.1–4.8). Varying the IPTG concentration allowed for the tuning of the oscillator period (Fig. 4.2A), particularly at low IPTG concentrations. The period decreased at high IPTG concentrations, and subsequent characterization of the promoter revealed that this non-monotonic behavior is probably caused by IPTG interference with AraC activation (Lee et al., 2007) (see Flow Cytometry section of Materials and Methods). The cell doubling time on the microfluidic device remained largely steady between experiments, ranging from 22.3 min to 27.6 min at 37°C and showing little correlation to IPTG concentration ($R^2 = 0.132$). Individual cell fluorescence trajectories showed a gradual increase in oscillatory period as the cells were imaged on the microfluidic device (Fig. 4.3). This increase was not seen in doubling times, implying that the cells were not experiencing nutritional difficulties or environmental stress that might cause an alteration in oscillator behavior.

To explore further the robustness of the oscillator, we investigated the effect of varying arabinose, temperature, and the growth medium. At a fixed value of 2 mM IPTG and at 37°C, the oscillatory period can be tuned from 13 min to 58 min by varying the arabinose level from 0.1$\%$ to 3.0$\%$ (Fig. 4.2B). Cells grown in the absence of arabinose did not produce measurable levels of yemGFP in single-cell microscopy or flow cytometry experiments, and high levels of arabinose seemed to saturate the system. We observed sustained oscillations at a range of temperatures from 25°C to 37°C, with a decreasing period as a function of temperature (Fig. 4.2C). The cell doubling time also decreased with temperature, as expected, and the oscillatory period increased monoton-

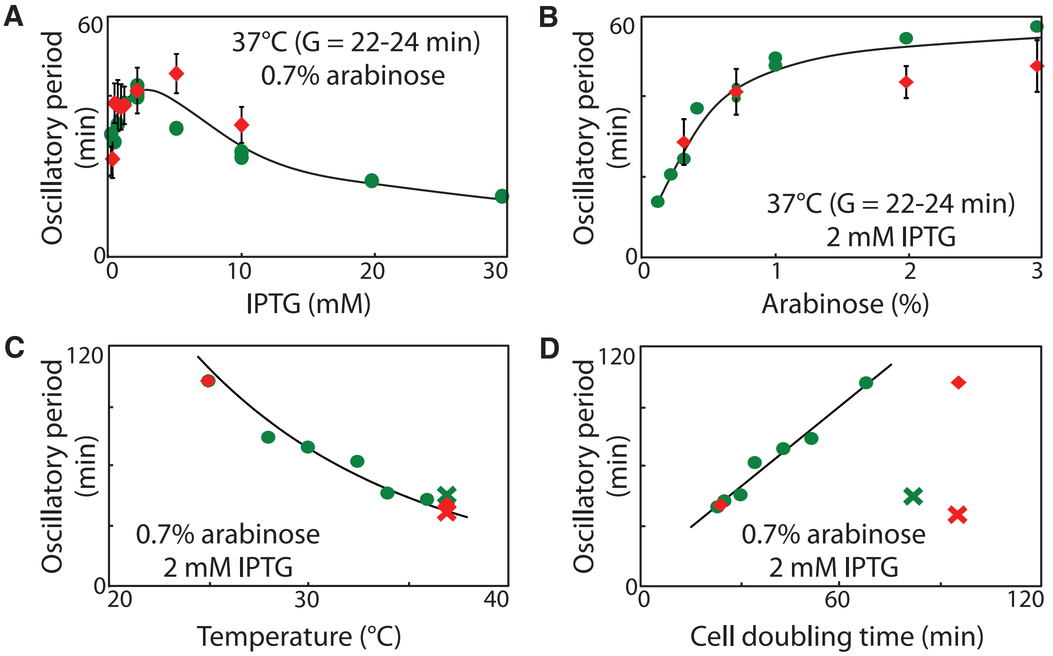

Figure 4.2: Robust oscillations with tunable period in the dual-feedback circuit. (**A**–**C**) Oscillatory periods on transects with 0.7% arabinose and varying IPTG (**A**); 2 mM IPTG and varying arabinose (**B**); or 0.7% arabinose, 2 mM IPTG, and varying temperature (**C**). Mean periods from single-cell microscopy (red diamonds, mean ± standard deviation) or flow cytometry (green circles) are shown. Black curves are trend lines in **A** and **B**, or represent the theoretical prediction based on reference values at 30°C in **C** (see Details of Computational Modeling section of Materials and Methods). Samples grown in minimal medium rather than LB are indicated by crosses. G represents the cell doubling time. (**D**) Oscillatory period and cell doubling time increase monotonically as the growth temperature decreases. Symbols are as described above, and the black line is a linear regression of flow cytometry samples grown in LB.

IPTG (mM)	Oscillating cells	Dim cells	Bright cells	Dead cells
0	129	0	0	2
0.25	149	0	0	0
0.5	209	0	0	0
0.75	331	0	0	0
1	129	0	0	2
2	231	0	2	2
5	233	0	0	0
10	155	0	0	0
Total	1566 **(99.5%)**	0 **(0.0%)**	2 **(0.1%)**	6 **(0.4%)**

Table 4.1: The oscillator circuit is functional in almost every cell observed with single-cell microscopy. The experiments shown in Supplementary Movies 4.1–4.8 were examined, and single cells were identified. Each cell was tracked by eye and classified into one of four groups: oscillating, never fluorescent, always fluorescent (with saturating levels of fluorescence), and dead (with abnormal morphology, usually swollen or burst, and no fluorescence).

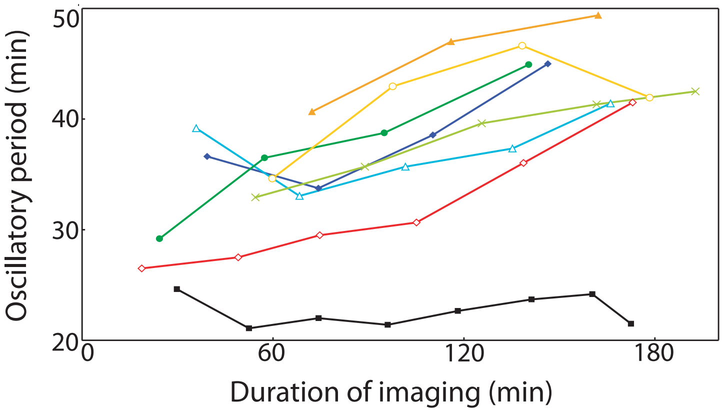

Figure 4.3: The effect of continued growth on oscillatory period. JS011 cells were grown in microfluidic devices for long-term single-cell imaging under inducing conditions. Each point is an average of oscillation periods from several cells at the same point in time and the same conditions (black squares, 0 mM IPTG; purple diamonds, 0.25 mM; blue triangles, 0.5 mM; green circles, 0.75 mM; green crosses, 1 mM; yellow circles, 2 mM; orange triangles, 5 mM; red diamonds, 10 mM). Data analysis was performed using custom-written MATLAB scripts.

ically with cell doubling time (Fig. 4.2D). The oscillator also functioned in minimal A medium with 2 g l^{-1} glucose (Fig. 4.2C, D). Although the cell doubling time in minimal medium was significantly longer than in LB-Miller formulation LB (80–90 min versus 22–24 min at 37°C), the oscillatory period in the minimal medium was very similar to that in LB (Fig. 4.2C, D). This result, together with the strong dependence of the period on IPTG and arabinose concentration (at constant cellular doubling times), demonstrates that the synthetic oscillator is not strongly coupled to cellular growth and division. The similar dependence of the period and the doubling time on the temperature seems to be due to the thermodynamic change of the rate constants affecting all cellular processes.

4.4 Computational Modeling

The oscillator was constructed according to design principles determined from previous theoretical work (Hasty et al., 2002a). However, we found that this original model failed to describe two important aspects of the experiments. First, the model could not describe the observed functional dependence of the period on inducer levels. Second, and perhaps most importantly, because careful parameter tuning was necessary for oscillations in the original model, it was not able to describe the robust behavior demonstrated in the experiments. These shortcomings forced a re-evaluation of the derivation of the oscillator equations and led to a new computational model that more accurately described the experimental observations. The new model incorporates the same coupled positive and negative feedback architecture but includes details that were omitted from the previous model. In particular, we found that directly modeling processes such as DNA looping, protein-DNA binding, DNA transcription, messenger ribonucleic acid (mRNA) translation, protein folding, protein multimerization, and enzymatic degradation greatly increased the accuracy of the model. The result is a computational model that is very robust to parameter variations and correctly describes the dynamics of the oscillator for a large range of IPTG and arabinose concentrations.

We used standard techniques to construct both stochastic and deterministic computational models (Tyson et al., 2003; Hasty et al., 2001; Ozbudak et al., 2004; Wang et al., 2006; Bennett et al., 2008) based on the same underlying biochemical reactions illustrated in Fig. 4.4A (see Details of Computational Modeling section of Materials and Methods). Although interactions between transcription factors and DNA are generally quite complicated to model in detail (Gerland et al., 2002), we used experimental induction curves to calibrate the induction levels in the reactions describing the network (Fig. 4.14). Over many oscillatory cycles, the deterministic simulations were then shown to give accurately the temporal evolution of the mode of the distributions generated by the exact stochastic simulations (Gillespie, 1977). Representative time series for the protein concentrations obtained from the stochastic and deterministic models are depicted in Fig. 4.4B, C. The models are very robust in that oscillatory behavior exists for a large range of parameter values and network details. Importantly, we found excellent quantitative agreement with the experimentally-obtained period as a function of inducer levels (Fig. 4.4D, E).

The amplitude and period of the oscillations as a function of inducer levels can be conceptually explained using Fig. 4.4C. A burst begins with the basal transcription of mRNA from both promoters, encoding both the activator and the repressor. After a short delay (caused by, for example, mRNA translation, protein folding, and protein multimerization), the amount of functional activator rises quicker than the amount of functional repressor, as shown in Fig. 4.4B. This occurs for two reasons. First, the activator gene is on a higher copy number plasmid than the repressor gene, meaning that more activator transcripts are produced than repressor transcripts. Second, assuming that transcription and translation of the monomeric forms of both proteins occur at similar rates, the activator will be more abundant because the functional tetrameric form of LacI requires twice as many monomers as does the functional dimeric form of AraC. As AraC levels rise, an activation burst in production of mRNA occurs due to the positive feedback loop. After LacI has been converted to a sufficient number of tetramers, the production of mRNA is turned off and the proteins decay enzymatically. Once all proteins have decayed, the promoters are freed of all bound regulators and the cycle

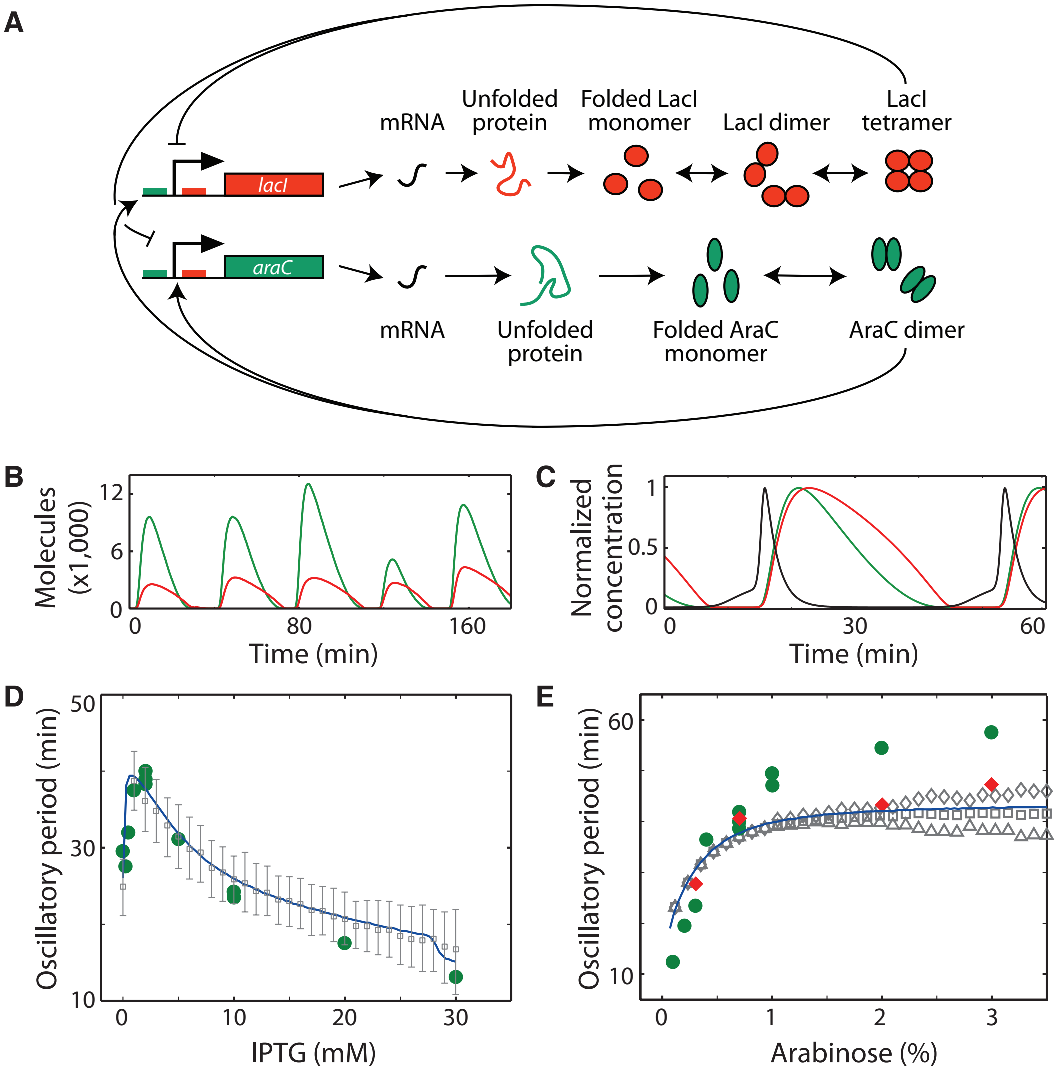

Figure 4.4: Modeling the dual-feedback genetic oscillator. (**A**) Intermediate processes are explicitly modeled in the refined oscillator model. (**B**, **C**) Simulation results from Gillespie simulations (**B**) or deterministic modeling (**C**) at 0.7% arabinose and 2 mM IPTG. AraC dimers (green), LacI tetramers (red), and *lacI* mRNA (black) are shown. (**D**, **E**) Comparison of modeling and experiment for oscillation period at 0.7% arabinose (**D**) or 2 mM IPTG (**E**). Values from deterministic modeling (blue curve), stochastic simulations (gray symbols, Fig. 4.22), and microscopy (red diamonds) or flow cytometry (green circles) are shown. Lower and upper error bars in **D** represent the 16th and 84th percentiles, respectively, of the stochastic data, corresponding to ± 1 standard deviation for a normal distribution.

begins anew. The length of the period is primarily determined by the time required for the proteins to decay. Therefore, the period is dependent on the rate of enzymatic decay and the magnitude of the activation burst. Furthermore, because the burst size depends on the induction characteristics of the promoter, it follows that the period is roughly proportional to the induction level of the promoter.

In examining our refined model, we discovered another region in parameter space that would support oscillatory behavior. Our model predicted that a constantly activated system with repression controlled by a negative feedback loop could produce oscillations in the absence of positive feedback (Fig. 4.23). It has been proposed that negative feedback gene networks can oscillate as long as there is delay in the feedback (Bliss et al., 1982; Bratsun et al., 2005), and, although there is no explicit delay in our model, the intermediate steps of translation, folding, and multimerization of LacI provide an effective form of delay (Rateitschak and Wolkenhauer, 2007) that is sufficient to support oscillations. We constructed this system (denoted JS013) in *E. coli* using a hybrid promoter, $p_{\mathrm{LlacO\text{-}1}}$ (Lutz and Bujard, 1997), that is activated in the absence of LacI (or presence of IPTG) to drive both *lacI* and *yemGFP* expression (Fig. 4.5A). We observed oscillations in these cells when examined by single-cell microscopy under inducing conditions (Fig. 4.5B, Fig. 4.6B, and Supplementary Movie 4.11). These oscillations were not as distinct or regular as in the dual-feedback oscillator, and they did not always return to a dim state, consistent with the predictions of the computational model. Furthermore, the period was largely unaffected by IPTG concentration (varying less than 5% over three experimental runs from 0.6 mM to 20 mM IPTG), suggesting that the addition of the positive feedback loop serves the dual role of regularizing oscillations and allowing tunability of the period (see Details of Computational Modeling section of Materials and Methods).

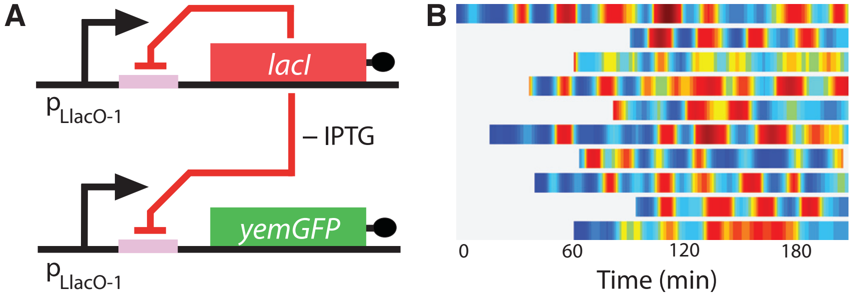

Figure 4.5: An oscillator with no positive feedback loop. (**A**) Network diagram of the negative feedback oscillator. This oscillator is similar to the dual-feedback oscillator except that the hybrid promoter, $p_{\mathrm{LlacO\text{-}1}}$ (Lutz and Bujard, 1997), gives expression of *lacI* and *yemGFP* in the absence of LacI or in the presence of IPTG without requiring an activator. (**B**) Single-cell density map trajectories for cells containing this oscillator (see Fig. 4.6B and Supplementary Movie 4.11).

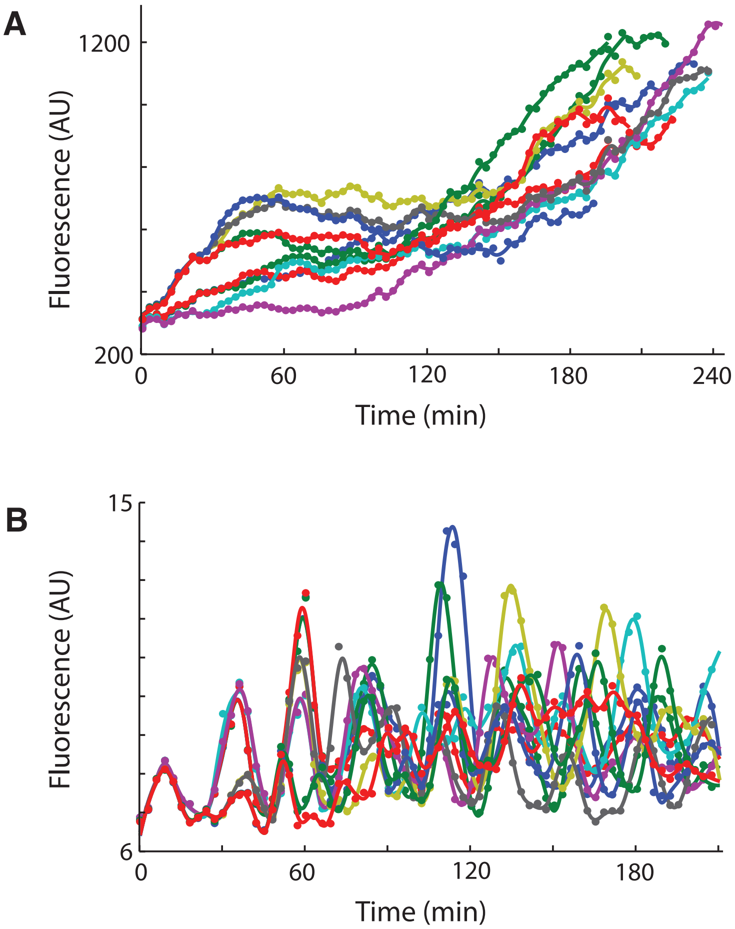

Figure 4.6: Single-cell fluorescence trajectories without and with the negative feedback loop. (**A**) MG1655Z1/pZE12-*yemGFP-ssrA* cells expressing LacI constitutively and containing neither positive nor negative feedback loops (induced with 2 mM IPTG). (**B**) JS013 cells containing the negative feedback oscillator (induced with 0.6 mM IPTG). Fluorescence measurements are given in AU that are consistent between the two experiments shown. Trajectories are smoothed with a Savitsky-Golay filter. Note that the cells without feedback are much brighter and do not show periodic fluorescence dynamics.

4.5 Materials and Methods

4.5.1 Plasmid Construction

The dual-feedback oscillator circuit was constructed by placing *araC*, *lacI*, and *yemGFP* under the control of the hybrid promoter, $p_{\text{lac/ara-1}}$ (Lutz and Bujard, 1997), in three separate transcriptional cassettes. Using a tagging vector, the two components of the oscillator (*araC* and *lacI*) and the gene encoding the fluorescent reporter protein (*yemGFP*) were tagged with carboxy-terminal *ssrA* tags (Andersen et al., 1998) consisting of TS**AANDENYALAA**. The TS sequence encodes a SpeI site and acts as a linker, while the *ssrA* tag (in bold) targets proteins to the ClpXP degradation pathway, greatly increasing their degradation rates and therefore dynamic behavior. The first codon of the *lacI* gene was changed from its wildtype sequence of GTG to a standard ATG start codon. The GFP allele used in this study contains F64L/S65T/A206K mutations and is codon-optimized for yeast expression (Sheff and Thorn, 2004). The first two mutations correspond to mut1GFP (Cormack et al., 1996), while the A206K mutation interferes with GFP dimerization (Zacharias et al., 2002). The yeast codon optimization does not appear to have any effects in *E. coli* other than a mild decrease in expression. In our experience, many GFP variants have deleterious effects in bacteria, especially when expressed at high levels, which may be due to multimerization (Shaner et al., 2005). The A206K mutation allows increased GFP expression without deleterious effects (as measured by growth rate or forward scatter (FSC) measurements by flow cytometry).

These three tagged genes were cloned into pZ modular plasmids under the transcriptional control of the $p_{\text{lac/ara-1}}$ hybrid promoter (Lutz and Bujard, 1997) to form three co-regulated transcriptional modules. The promoter, ribosome binding sequence, and downstream terminator are identical between modules. The $p_{\text{lac/ara-1}}$ promoter is activated by AraC in the presence of arabinose and repressed by LacI in the absence of IPTG. It includes two *lacO* operator sites, one overlapping and the other $\sim$500 base pair (bp) upstream of the transcription start site. LacI repression is mediated by DNA looping by LacI tetramer bound to both sites. We found that a single point mutation in the upstream *lacO* site abolished LacI repression.

The activator *araC* module and the reporter *yemGFP* module were placed on a ColE1 plasmid with kanamycin resistance (pJS167). Although this plasmid contains repeated regions (the $\mathrm{p}_{\mathrm{lac/ara\text{-}1}}$ and terminator sequences), we found no evidence of plasmid instability. The repressor module was placed on a p15A plasmid with ampicillin resistance (pJS169). All sequence junctions and sections amplified by the polymerase chain reaction (PCR) were confirmed by sequencing (see Fig. 4.7).

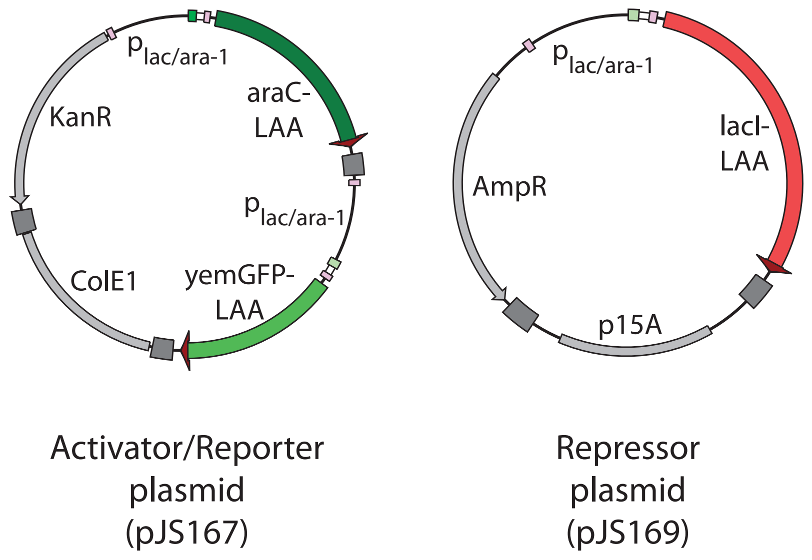

Figure 4.7: The two plasmids containing the dual-feedback oscillator circuit. The activator and reporter modules are on a derivative of pZE24 (Lutz and Bujard, 1997), a medium-copy (Chang and Cohen, 1978) ColE1 plasmid, while the repressor module is on a derivative of pZA14 (Lutz and Bujard, 1997), a lower-copy (Kahn et al., 1979; Atlung et al., 1999) p15A plasmid. Co-transformation of Δ*araC* Δ*lacI E. coli* cells with both of these plasmids gives the oscillator strain JS011. Transcriptional terminators are shown as dark gray squares. Plasmid maps were drawn with Savvy (http://www.bioinformatics.org/savvy/).

To construct the negative feedback oscillator circuit, the hybrid promoter $\mathrm{p}_{\mathrm{LlacO\text{-}1}}$ (Lutz and Bujard, 1997) was used to regulate expression of *lacI* and *yemGFP*. Both genes were tagged with *ssrA* tags as described above. The $\mathrm{p}_{\mathrm{LlacO\text{-}1}}$ promoter consists of the p_{L} promoter from λ phage with *lacO* sites replacing the cI binding sites. The p_{L}

promoter gives constitutive transcription without cI binding. The addition of *lacO* sites allows repression by LacI in the absence of IPTG. Two transcriptional modules containing $p_{\mathrm{LlacO\text{-}1}}$ and *lacI* or *yemGFP* were constructed as above. The repressor module was placed on a p15A plasmid with chloramphenicol resistance (pZA32-*lacI-ssrA*), and the reporter module was placed on a ColE1 plasmid with ampicillin resistance (pZE12-*yemGFP-ssrA*).

4.5.2 Strain Construction

Strains of *E. coli* with deletions in *araC* (JW0063) or *lacI* (JW0336) were obtained from the Keio collection (Baba et al., 2006). Strains from this collection have single gene deletions that are linked to a kanamycin resistance marker that can be eliminated by site-specific recombination with an exogenously supplied recombinase. To construct the oscillator strain, kanamycin resistance was eliminated from JW0063, and Δ*lacI* was introduced into the resulting strain by P1*vir* phage transduction from JW0336. Double knockout transductants were selected for by growth on 50 μg ml^{-1} kanamycin, and kanamycin resistance was again eliminated as above to construct strain JS006 (MG1655 Δ*araC* Δ*lacI* Kan^S). Genomic alterations were confirmed by genomic PCR (Datsenko and Wanner, 2000) and sequencing. The locations of the kanamycin resistance remnants are sufficiently separated on the bacterial chromosome to prevent further recombination between deletion sites. The dual-feedback oscillator strain JS011 was constructed by transforming JS006 with pJS167 and pJS169 such that the only source of AraC and LacI was the oscillator plasmids. To construct the negative feedback oscillator strain, kanamycin resistance was eliminated from JW0336 to form strain JS002 (MG1655 Δ*lacI* Kan^S). JS002 was then transformed with the two negative feedback oscillator plasmids described above to construct JS013.

4.5.3 Microfluidic Device Design and Fabrication

We examined cells with time-lapse fluorescence microscopy using microfluidic devices designed to support growth of a monolayer of *E. coli* cells under constant nutrient flow (Fig. 4.8). Coupling these microfluidic devices with fluorescence measurement and cell tracking methods allowed us to generate fluorescence trajectories for single cells. The design of the microfluidic device used in these experiments was adapted from the TμC design developed by Cookson*, Ostroff*, Pang*, Volfson, and Hasty (2005, *equal contribution) for use with *S. cerevisiae*. The original TμC design implemented the classic Tesla diode loop (Tesla, 1920; Duffy et al., 1999; Bendib and Français, 2001) modified for imaging a monolayer culture of growing yeast cells. Here, modifications were made to support imaging monolayers of *E. coli*, which included lowering the cell chamber height from 4 μm to 1 μm to match the cylindrical diameter of K-12 MG1655 cells, lowering the delivery channel height from 12 μm to 3 μm to maintain equivalent flow splitting between the cell chamber and the bypass channel, and dividing the cell-trapping region into three channels for simultaneous observation of isolated colonies (Fig. 4.8A, B). Lastly, the width of each parallel chamber was limited to 30 μm so as not to exceed the width/height aspect ratio of 30 for PDMS and risk structural collapse of the chamber "ceilings."

In order to achieve long experimental runs, a critical design objective was to avoid clogging between the media port and the trapping region. Toward this end, we developed a three-port chip design in which the main channel extending from the cell port splits into a media channel and a waste channel downstream of the trapping region. The waste port receives untrapped cells during loading and superfluous media during runtime, thereby eliminating contamination of the media port. Cells were loaded into the three trapping channels of the microfluidic device by directing flow in the "forward" direction from the cell port to the waste port. Upon trapping a few cells in each region, the flow was reversed and slowed to steadily supply the cells with fresh nutrients from the media port through a combination of diffusion and advection. Cells grew exponentially

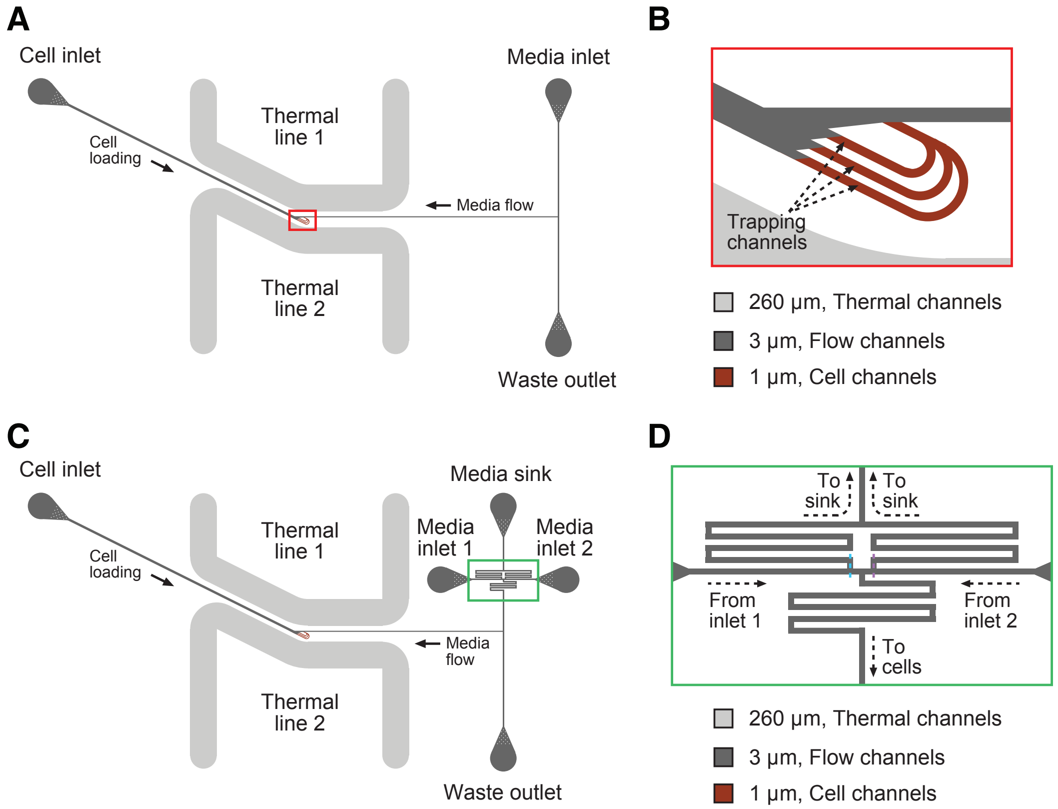

Figure 4.8: Schematics of microfluidic devices used in time-lapse microscopy experiments. (**A**) The TμC device adapted for imaging monolayer colonies of *E. coli* over many cellular generations. Cells are loaded into the trapping channels (dark red, magnified in **B**) by directing flow from the cell inlet to the waste outlet, and then flow is reversed and slowed to provide fresh medium to the cells from the media inlet during the experiment. Flow is maintained away from the media inlet at all times to prevent contamination of this reservoir. Thermal control is achieved by flowing heated water from a reciprocating bath through two high-volume thermal lines (light gray). (**B**) A magnified view of the cell-trapping region (red boxed region in **A**). Cells are loaded into three parallel trapping channels for simultaneous observation of isolated colonies. (**C**) A variant of the device shown in **A**, with an integrated switch incorporated into the media supply line. This switch supports the selection of one of two types of media and is based on laminar flow boundary shifting. (**D**) A magnified view of the switching region (green boxed region in **C**). By shifting the boundary separating the laminar flows of medium 1 and medium 2 to the channel centerline at the left (dashed blue line), flows of both media are directed to the media sink port through the shunt channels, and medium 2 is delivered to the cells. In the opposite configuration, where the laminar flow boundary is shifted to the channel centerline at the right (dashed purple line), flows of both media are directed to the media sink port through the shunt channels and medium 1 is delivered to the cells. Sustained flow of each type of media to the media sink through the shunt channels prevents cross-contamination of the media reservoirs.

to fill the channels over an experimental duration of ∼4–6 h, while images were periodically acquired in the transmitted and fluorescent channels every 2–3 min. The open walls of the trapping region allowed for cells at the periphery of the expanding colonies to be swept away by the high flow in the main channel, thus permitting continuous exponential growth long after the trapping region filled. For optimal *E. coli* growth, chip temperature was typically maintained at 37°C by flowing heated water through deep thermal channels fabricated into the device.

For on-chip induction experiments, we used a variant of the above-described device that incorporated a laminar boundary media switch into the design (Groisman et al., 2005) (Fig. 4.8C). This microfabricated switch directed flow to the cells from one of two media inlet ports by shifting the boundary between the two laminar flow streams (Fig. 4.8D). In these experiments, cells were loaded into the device and grown for several generations in non-inducing medium without periodic image acquisition in order to minimize fluorescence exposure. Upon expanding to occupy roughly half of the field of view, the cells were induced by flipping the state of the on-chip media switch, which switched to inducing medium in less than 1 s. We maintained constant flow from both media inlets to the media sink throughout the switching operation in order to prevent backflow contamination of the media inlets. The uninduced and induced media solutions were differentiated by labeling the inducing medium with Sulforhodamine 101 red fluorescent dye. Cells grown in the absence of inducers initiated oscillations in a synchronous fashion upon the addition of inducers (Supplementary Movie 4.10). This initial synchrony of oscillations suggested the possibility of using flow cytometry to further characterize the oscillator.

All described devices were fabricated in the UCSD Integrated Technology Laboratory (ITL) and the Calit2 Nano3 facility using standard soft lithography techniques (Duffy et al., 1998; Unger et al., 2000; Whitesides et al., 2001; Sia and Whitesides, 2003). Photomasks were drawn in FreeHand MX (Macromedia Inc.; San Francisco, CA), printed onto transparency film at high resolution (Output City; Poway, CA), and mounted to clean borosilicate glass plates (McMaster-Carr; Los Angeles, CA). Master molds were created by first spin-coating SU-8 2000 negative photoresists (MicroChem Corp.; Newton, MA) upon clean silicon wafers to appropriate depths using a Headway PWM32 programmable spinner (Headway Research Inc.; Garland, TX) and then patterning with a UV contact mask aligner (HTG; San Jose, CA). After all photolithographic steps were completed, SU-8 feature heights were verified using a DEKTAK 3030ST profilometer (Sloan Technology Corp.; Santa Barbara, CA), and treated with vaporous CTMS for 5–10 min. Replica molds were created from master molds by mixing PDMS (Sylgard 184; Dow Corning; Midland, MI) in a 10:1 (elastomer base/curing agent) ratio, degassing in a vacuum desiccator at $\sim$-1 atm for 1 h, and curing in place over the master at 80°C for 2 h. After removal of the PDMS monolith, chips were sectioned, bored at the fluidic ports, cleaned with Scotch 810 office tape and HPLC-grade methanol, and permanently bonded to clean 24×40 mm^2 no. $1\frac{1}{2}$ coverslips (Corning Inc.; Corning, NY) via exposure to O_2 plasma at 30 W for 1 min in a 500-II Plasma Asher (Technics Plasma; Danville, CA).

4.5.4 Microscopy and Image Processing

All images were acquired using one of two microscopy configurations—one for brightfield imaging and another for phase contrast imaging. The brightfield setup comprised a Diaphot TMD epifluorescent inverted microscope (Nikon Instruments Inc.; Tokyo, Japan) outfitted with fluorescence excitation and emission filter wheels (filter set #86006 for CFP/YFP/DsRed; Chroma Technology Corp.; Rockingham, VT) and automated by a custom application written in LabVIEW (National Instruments; Austin, TX). The phase contrast setup comprised a TE2000-U epifluorescent inverted microscope (Nikon Instruments Inc.; Tokyo, Japan) outfitted with fluorescence excitation and emission filter wheels (filter set #89006 for CFP/YFP/mCherry; Chroma Technology Corp.; Rockingham, VT) and a GFP filter cube (#GFP-3035B-NTE; Semrock Inc.; Rochester, NY) and automated by NIS-Elements Advanced Research software (Nikon Instruments Inc.; Tokyo, Japan). Both configurations used a ProScan II XY-motorized stage with fine focus control (Prior Scientific Inc.; Rockland, MA), Uniblitz VS35 high-speed shutters (Vincent Associates; Rochester, NY), an Orca-ER cooled CCD camera (Hamamatsu Photonics; Hamamatsu, Japan), and an X-Cite Series 120 fluorescent lamp (EXFO; Quebec, Canada).

In each experiment, a microfluidic device was mounted to the stage and wetted using a solution of 0.1% v/v TWEEN 20 surfactant (Sigma-Aldrich; St. Louis, MO) in the appropriate medium. Culture temperature was maintained by connecting high-volume fluidic channels fabricated into the device to a reciprocating temperature-controlled water bath. Cells that had been passed from an overnight culture into inducing medium ∼3–4 h earlier were loaded into the device from the cell port by directing high flow both from the cell port and the media port to the waste port. Upon trapping a single cell in each channel, flow past the cell chamber was reversed and slowed to 1–2 μm s^{-1} such that fresh nutrients were delivered from the media port via a combination of diffusion and advection without physically disturbing the cells.

During exponential growth of the monolayer colony, images were collected at ×100 magnification in the brightfield or phase contrast and YFP or GFP fluorescence channels (for the two microscope setups described above, respectively) every 2–3 min over a period of ∼4–6 h. Experimental runs were often allowed to run for longer durations, but data analysis was limited to the initial period when the growth chamber had not filled. Focus was maintained during image acquisition by either manual adjustment or contrast-based autofocus algorithms. Following each imaging session, fluorescence trajectories of individual cells were extracted using the Wright Cell Imaging Facility (WCIF) ImageJ cell analysis package (Wayne Rasband; Research Services Branch; National Institute of Mental Health; Bethesda, MD with plug-in collation and organization by the WCIF; Toronto, ON). For each fluorescence frame, mean values of integrated fluorescence were calculated within constant circular areas inscribed within the boundaries of all tracked cells. Long-term fluorescence trajectories were subsequently constructed by manually tracking each cell throughout the experiment. Raw fluorescence trajectories were typically smooth (Fig. 4.9). In cases where cell boundaries could not be resolved in the fluorescence images due to low signal, circular areas were appropriately positioned in accordance with the synchronously collected transmitted images. The great majority of the cells showed oscillations in fluorescence (Table 4.1).

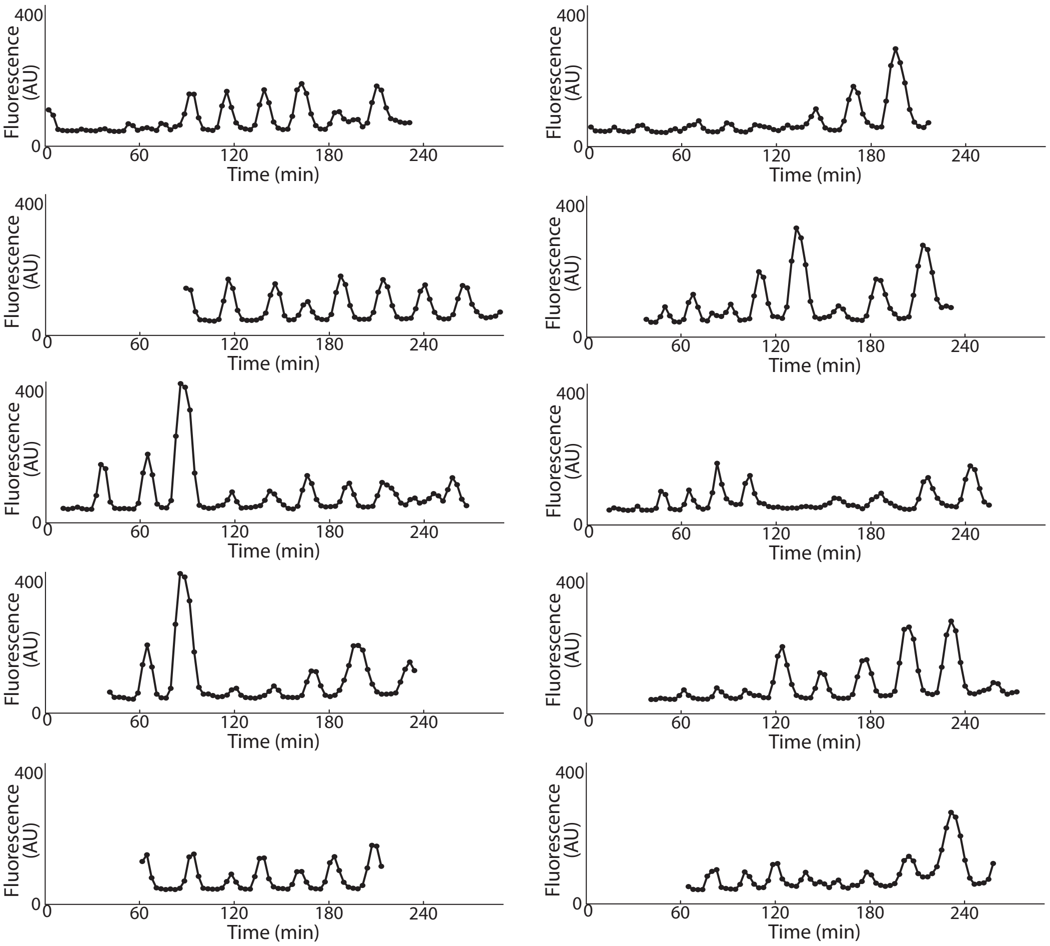

Figure 4.9: An example of unsmoothed fluorescence trajectories. These trajectories were taken from a time-lapse microscopy run at 0.7% arabinose and 0.1 mM IPTG. Each trajectory is a single cell undergoing division and oscillation. The arbitrary fluorescence units on the y-axes are equivalent.

Movies of our constant-induction microscopy runs are provided as Supplementary Movies 4.1–4.9 (dual-feedback loop oscillator, JS011, in LB at 37°C (Movies 4.1–4.8) or 25°C (Movie 4.9)) and 4.11–4.12 (negative feedback loop oscillator, JS013, or control strain, MG1655Z1/pZE12-*yemGFP-ssrA*, in LB at 37°C; see also Fig. 4.6).

Transmitted and fluorescence channels are overlaid in gray and green, respectively. Additionally, a movie capturing the dynamic induction of the dual-feedback oscillator in a partially-filled cell chamber is presented as Supplementary Movie 4.10 (see above). This movie demonstrates that step induction initiates synchronous oscillations within single cells of the colony.

4.5.5 Flow Cytometry

Initial Circuit Characterization

We initially characterized the circuit by flow cytometry of JS011 cells grown in batch cultures. An overnight culture of JS011 was diluted 1:4,000 in LB (10 g l^{-1} NaCl) with 100 μg ml^{-1} ampicillin, 50 μg ml^{-1} kanamycin, and a range of concentrations of L-arabinose and IPTG, and grown for 3.5 h at 37°C. Samples were washed with phosphate buffered saline (PBS) by centrifugation, and flow cytometry analysis was performed. Our expectation was that, given a circuit that produced oscillating cellular fluorescence levels, some of the cells in an unsynchronized population would have fluorescence levels intermediate to bright and dim levels. In contrast, a monostable circuit would result in a well-defined unimodal distribution, and a bistable circuit would result in a bimodal distribution with few intermediate cells. A survey of inducer space using this method revealed potentially oscillatory regions that we subsequently investigated in greater detail using flow cytometry and microscopy (Figs. 4.10 and 4.11).

Continuous Time-Course Flow Cytometry

Additional flow cytometry was performed by one of two similar protocols. The temperature-dependence experiments followed a continuous time-course flow cytometry protocol, in which a single culture was induced at the initial time point and samples were removed for flow cytometry analysis over the course of the experiment. An overnight culture of JS011 was diluted in growth medium with antibiotics and grown for 3 h at the indicated temperature with 250 rpm shaking. The OD_{600} of the culture

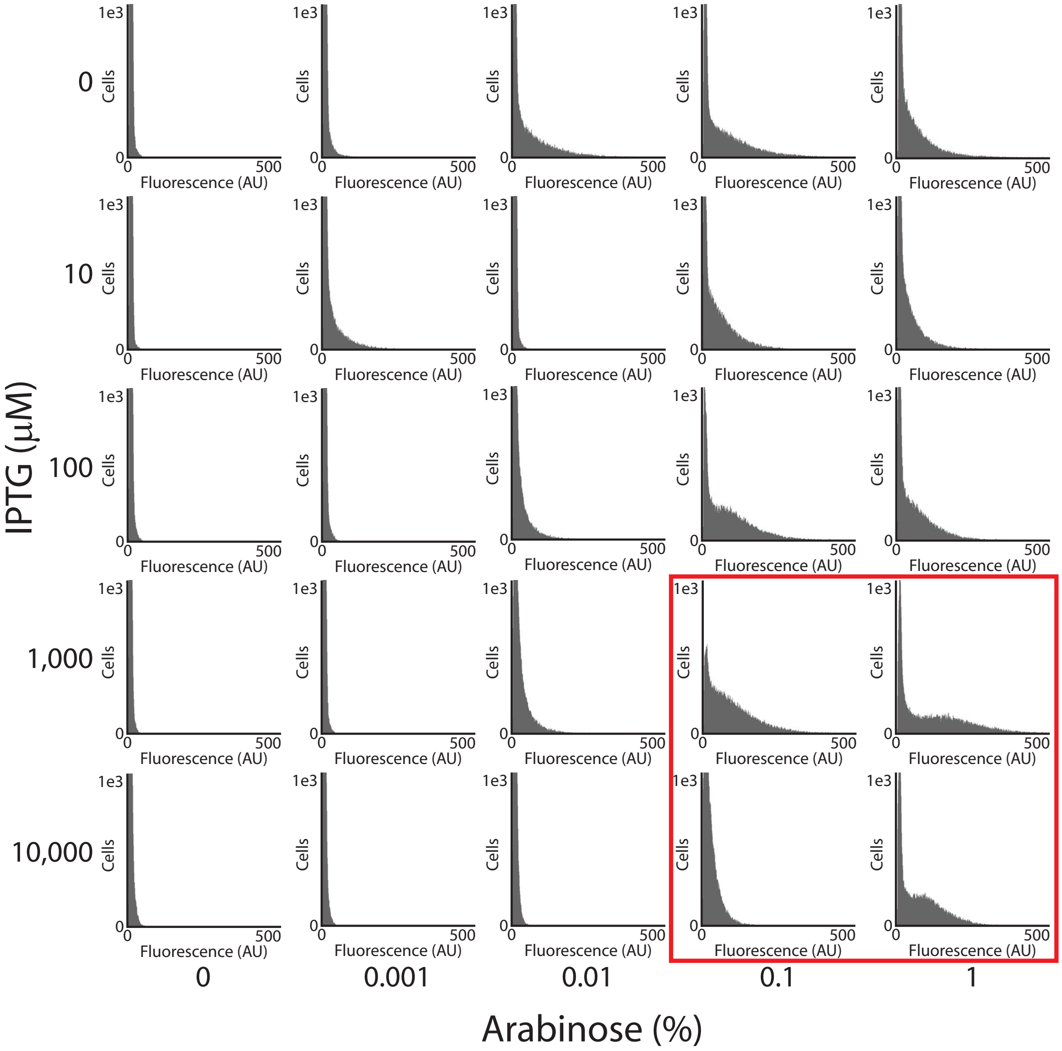

Figure 4.10: A survey of inducer space by flow cytometry. Each subpanel is a fluorescence histogram of a flow cytometry run of JS011 grown in the presence of the indicated inducers. Fluorescence data were collected using linear mode. The x-axis of each plot is linearly scaled and the y-axis of each plot is truncated at 1,000 events to emphasize the shoulders in the distribution. Cells brighter than 500 AU are collected in the rightmost (brightest) bin. In each case, less than 1% of the cells fell into this bin. Distributions showing shoulders on the right side of the distribution (outlined in red) suggest oscillations in cellular fluorescence and were investigated more closely (see Fig. 4.11).

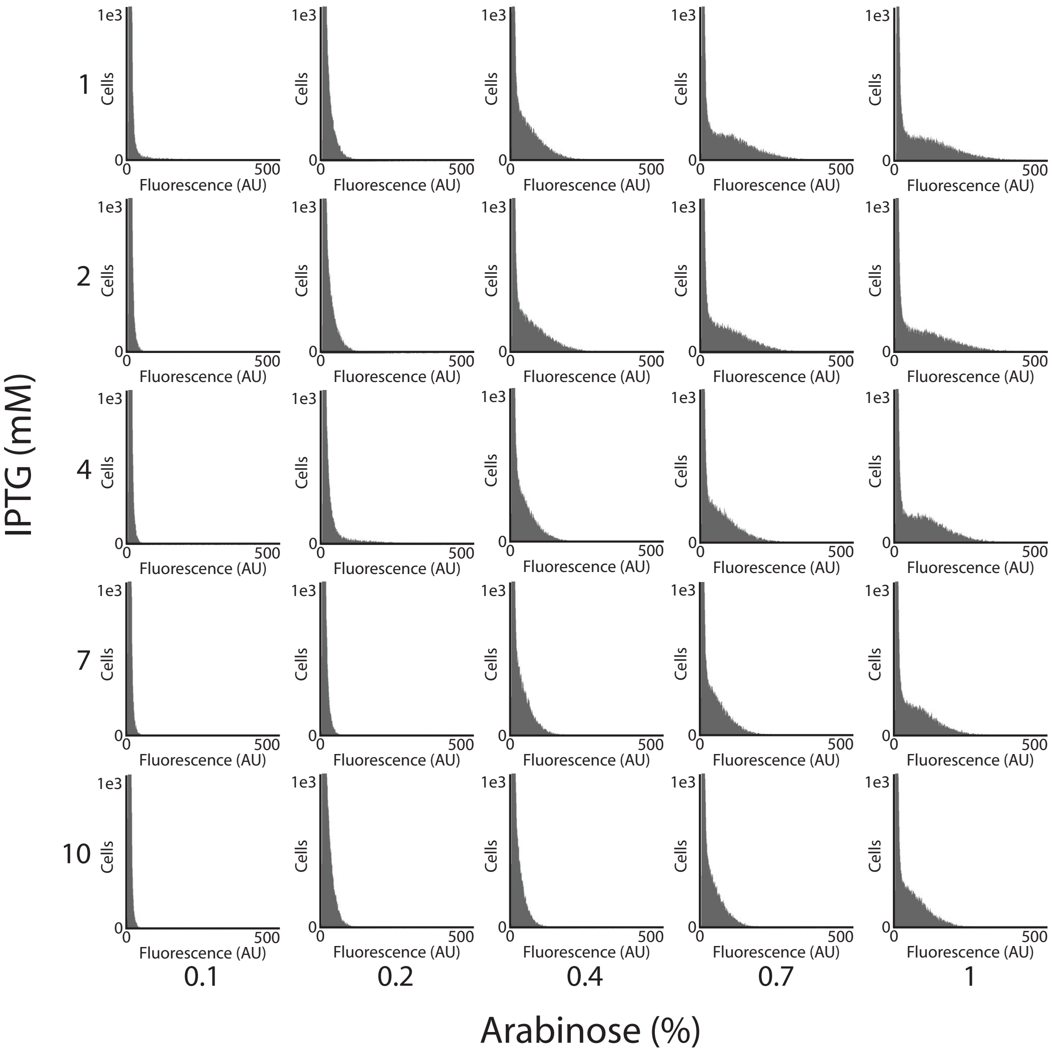

Figure 4.11: A closer look at shouldered fluorescence distributions at some inducer concentrations. Each subpanel is a fluorescence histogram of a flow cytometry run of JS011 grown in the presence of the indicated inducers. Fluorescence data were collected using linear mode. The x-axis of each plot is linearly scaled and the y-axis of each plot is truncated at 1,000 events to emphasize the shoulders in the distribution. Cells brighter than 500 AU are collected in the rightmost (brightest) bin. In each case, less than 1% of the cells fell into this bin.

was ∼0.01–0.02 at this point. A pre-induction sample was removed for immediate flow cytometry analysis, and inducers were added to the remaining culture to the indicated concentrations. The culture was then grown as previously and samples were removed from the culture at regular intervals for flow cytometry. Approximately every three doubling times (∼70–80 min in LB) the culture was diluted 1:9 in prewarmed medium with antibiotics and inducers, and this diluted culture was used for subsequent time points. These serial dilutions kept the OD_{600} of the culture below 0.2. The amplitude of the oscillations was initially high and decreased as the experiment continued, presumably due to desynchronization of the cells and apparent spreading of the oscillatory peaks (Fig. 4.12).

Aggregate Time-Course Flow Cytometry

Inducer-dependence experiments used an aggregate time-course flow cytometry protocol, where an uninduced culture was aliquoted onto different inducer concentrations and allowed to grow for varying lengths of time. An overnight culture of JS011 was diluted 1:100,000 in LB with antibiotics and grown at 37°C. During this growth, culture tubes containing inducers were prewarmed. Between 2.5 and 4 h after initial dilution, aliquots of the growing culture were added to inducer tubes at regular intervals, resulting in a set of cultures with varying induction times. At the end of the experiment, all samples were quickly measured by flow cytometry (∼3 samples min^{-1}), starting with the lowest induction duration. The induction duration was calculated as the time between addition of culture to inducer and flow cytometry measurement, and the oscillatory period was calculated as the time between the first peak and the second peak of the mean fluorescence of the culture.

This protocol allowed parallel examination of multiple inducer conditions more easily than the continuous time-course protocol. Amplitudes and oscillation periods increased along the arabinose transect at 2 mM IPTG as arabinose increased (Fig. 4.13). At low levels of arabinose, mean fluorescence was low enough that following oscilla-

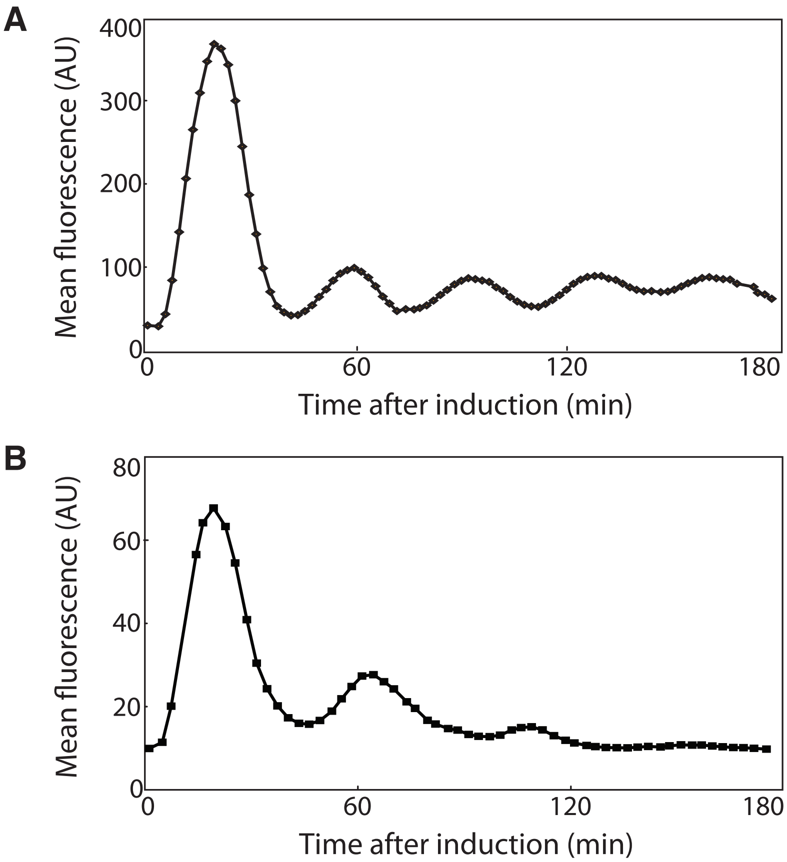

Figure 4.12: Oscillations observed by flow cytometry. JS011 cells were grown at 37°C in either LB (**A**) or minimal A medium as in Miller (1992) with 1 μg ml^{-1} thiamine and 2 g l^{-1} glucose (**B**) plus antibiotics. Oscillations were measured by flow cytometry of samples continually harvested from growing cultures induced with 0.7% arabinose and 2 mM IPTG. Lines connecting the points are unsmoothed. In both cases, oscillations were confirmed by time-lapse microscopy and shown to not decrease in amplitude over time, suggesting that the apparent ringing down of the oscillator in flow cytometry experiments is an artifact of the culture conditions or sampling method.

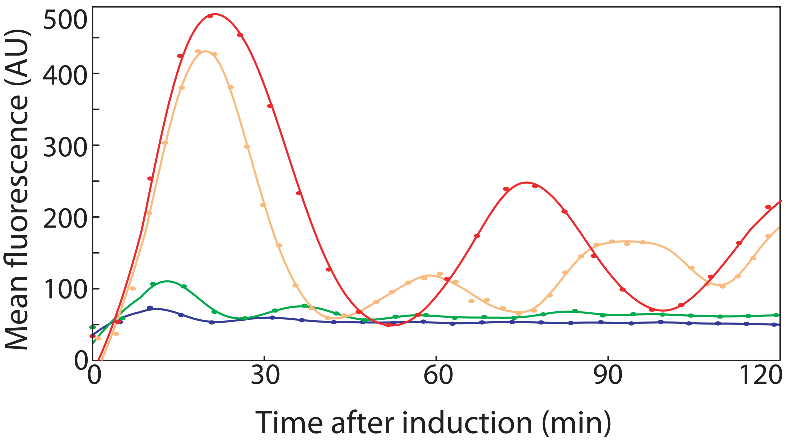

Figure 4.13: Oscillations in mean fluorescence over time on a transect along 2 mM IPTG. Fluorescence was measured by flow cytometry of samples induced with various levels of arabinose (blue, 0.2% arabinose; green, 0.3%; orange, 0.7%; red, 2%) and 2 mM IPTG and grown for a range of durations. Solid curves are smoothed by a Savitsky-Golay filter. (Flow cytometry data for the 2% arabinose sample are shown in Figs. 4.18 and 4.19.)

tions after the second peak became difficult. However, microscopy experiments at these arabinose levels confirmed that the cells were oscillating. The values seen along the IPTG transect at 0.7% arabinose were in good agreement with the period measurements obtained from single-cell trajectories (Fig. 4.2A), although measurements derived from single-cell trajectories were consistently higher. This could be due to an unexplained difference in the growth environment (although doubling times were consistent across the two methods), or it could be related to the gradual increase in period seen in the microscopy experiments (Fig. 4.3). Extension of the IPTG transect to IPTG levels higher than those examined by microscopy resulted in oscillations with low amplitudes and short periods, confirming the decrease in period seen in the microscopy experiments.

Hybrid Promoter Characterization

Hybrid promoter induction curves were determined using MG1655Z1 cells (Lutz and Bujard, 1997) transformed with a plasmid that contained *yemGFP-ssrA* under the control of the $\mathrm{p}_{\mathrm{lac/ara\text{-}1}}$ hybrid promoter (essentially pJS167 without the activator module). MG1655Z1 constitutively produces LacI, which is necessary to support IPTG-mediated release of repression given the large number of *lacO* sites on multiple-copy plasmids. AraC is produced from the wildtype genomic locus. These cells have neither feedback loop from the dual-feedback oscillator. An overnight culture of these cells in LB with kanamycin was diluted 1:3,000 in fresh LB with kanamycin and grown for 2 h at 37°C with shaking. The cells were then diluted 1:4 in fresh LB with kanamycin, arabinose, and varying levels of IPTG and grown for 2.5 h before being analyzed by flow cytometry.

These induction curves showed a decrease in fluorescence starting at $\sim$2–3 mM IPTG similar to that seen in the oscillation period transect along IPTG (Fig. 4.14). IPTG has been observed to interfere with AraC-arabinose binding and subsequent activation at another arabinose-inducible promoter (Lee et al., 2007). We investigated whether IPTG interfered with AraC activation of $p_{\text{lac/ara-1}}$ using a strain with the activator but no repressor module. Arabinose induction of this system results in a runaway positive feedback loop (Fig. 4.15) due to the lack of LacI repressor. This runaway induction can be prevented by IPTG addition despite the lack of LacI (Fig. 4.16). We conclude that IPTG can interfere with activation of $p_{\text{lac/ara-1}}$, and this crosstalk in our circuit is responsible for the decreases in expression of *yemGFP* and in oscillation period that we observe.

Operation and Data Interpretation

All flow cytometry analysis was carried out on a Becton-Dickinson FACScan. Unless otherwise specified, samples were read directly from the LB growth medium. Under these conditions, FSC histograms (at E00 voltage setting in log mode) showed two well-separated subpopulations: a low-FSC population (FSC < 10) that was never fluorescent and a higher-FSC population that had a unimodal distribution with a mean FSC of $\sim$70–100 and could be fluorescent. (Similar results were found with *E. coli* cells expressing *yemGFP* under a constitutive promoter, or with wildtype *E. coli* cells,

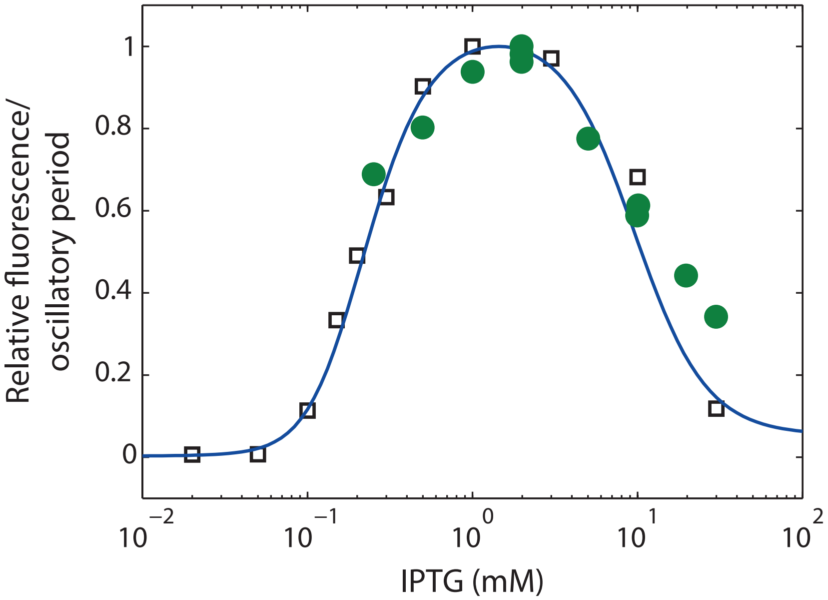

Figure 4.14: Oscillation period dynamics mirror hybrid promoter induction. The experimental induction data from the $p_{\text{lac/ara-1}}$ hybrid promoter in MG1655Z1 cells (with neither feedback loop, black squares) correlates well with the experimental oscillator periods determined by flow cytometry in JS011 cells (both feedback loops, green circles). Both data sets are normalized to their maximum value. The induction curve obtained from the deterministic model (blue curve) is also shown.

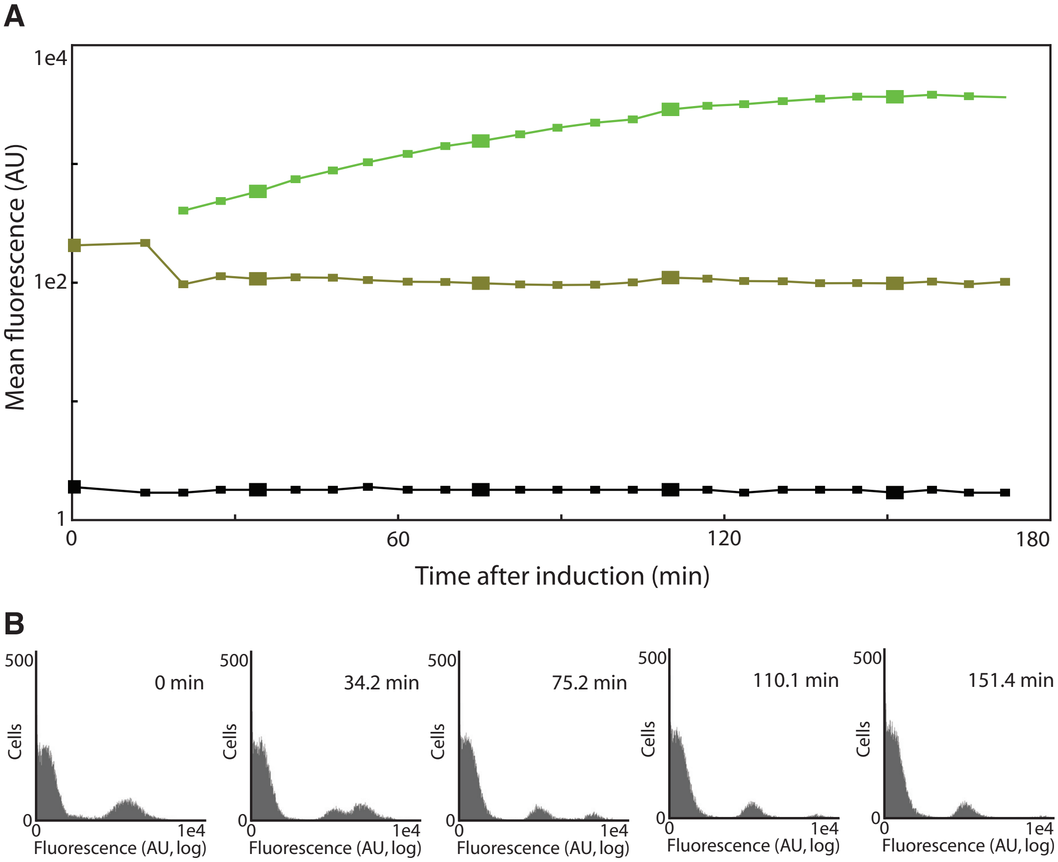

Figure 4.15: Fluorescence dynamics without the repressor module. JS006 cells (Δ*araC* Δ*lacI*) were transformed with pJS167 containing the activator and reporter modules. No *lacI* is present in this strain. (**A**) Time-course flow cytometry, inducing with 0.7% arabinose and 2 mM IPTG at $t = 0$, on the resulting cells, which were separated into three subpopulations based on the fluorescence distributions (**B**). (**B**) Before induction, distribution of the cells was bimodal, with a dim subpopulation (black points in **A**, left peak in the $t = 0$ distribution) and a brighter subpopulation (olive points in **A**, right peak in the $t = 0$ distribution). Upon induction, a third subpopulation of very bright cells separated from the bright cells (green points in **A**, rightmost peak in the post-induction distributions). As induction continued, this subpopulation became extremely bright, increased in size, and eventually decreased in number until they were essentially eliminated from the population. The larger time points in **A** correspond to the distributions in **B**. (The corresponding strain without the activator module is shown in Fig. 4.17.)

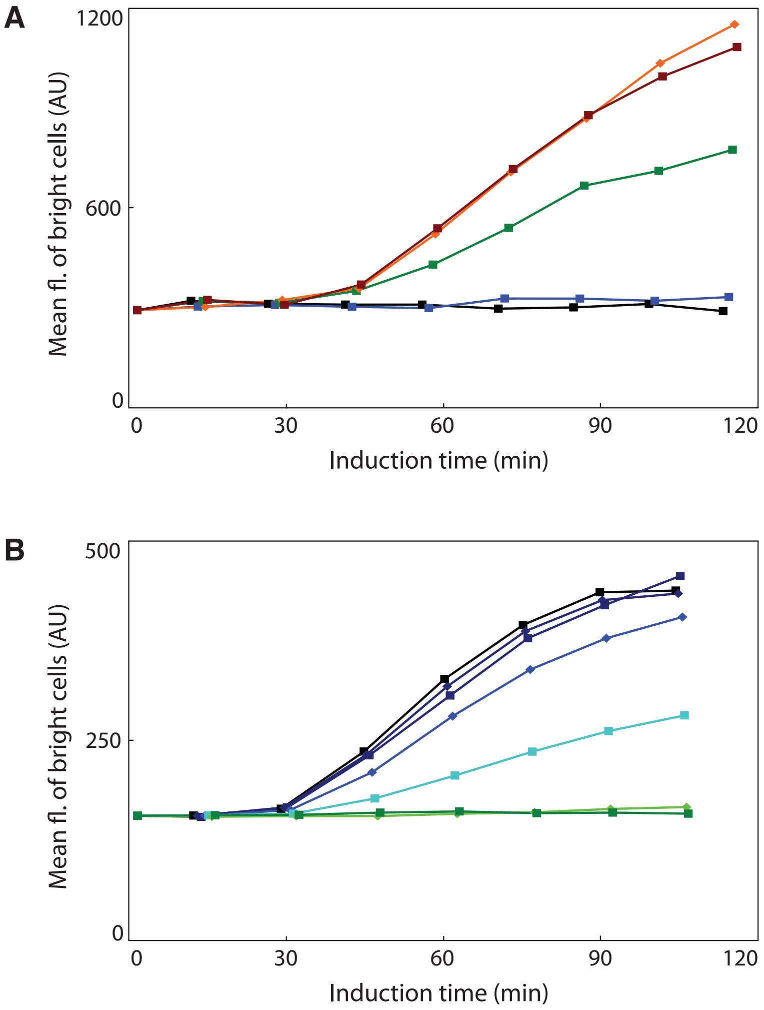

Figure 4.16: High levels of IPTG interfere with $\mathrm{p}_{\mathrm{lac/ara\text{-}1}}$ expression in the absence of LacI. JS006/pJS167 cells have a genomic *lacI* deletion and no plasmid-expressed *lacI*. Arabinose induction results in expression of additional *araC* as well as *yemGFP*, giving a positive feedback loop that induces runaway *yemGFP* expression in a subset of the cells (Fig. 4.15). (**A**) This runaway expression can be measured by the mean fluorescence of the brightest subpopulation. Cells were grown as in Fig. 4.15 and induced with varying levels of arabinose (black, no arabinose; blue, 0.01%; green, 0.1%; brown, 0.3%; orange, 1%), and cellular fluorescence was measured by flow cytometry after induction. The magnitude of the effect is dependent on arabinose concentration, requires at least 0.1% arabinose, and saturates at high levels of arabinose. (**B**) The addition of IPTG can interfere with this arabinose-induced runaway expression even in the absence of LacI . Cells were grown as in Fig. 4.15, induced with 0.1% arabinose and varying levels of IPTG (black squares, no IPTG; dark blue diamonds, 0.1 mM; dark blue squares, 0.3 mM; blue diamonds, 1 mM; blue-green squares, 3 mM; bright green diamonds, 10 mM; dark green squares, 30 mM), and cellular fluorescence was measured by flow cytometry after induction. IPTG interference with runaway activation required 1–3 mM IPTG and was total at 10 mM IPTG.

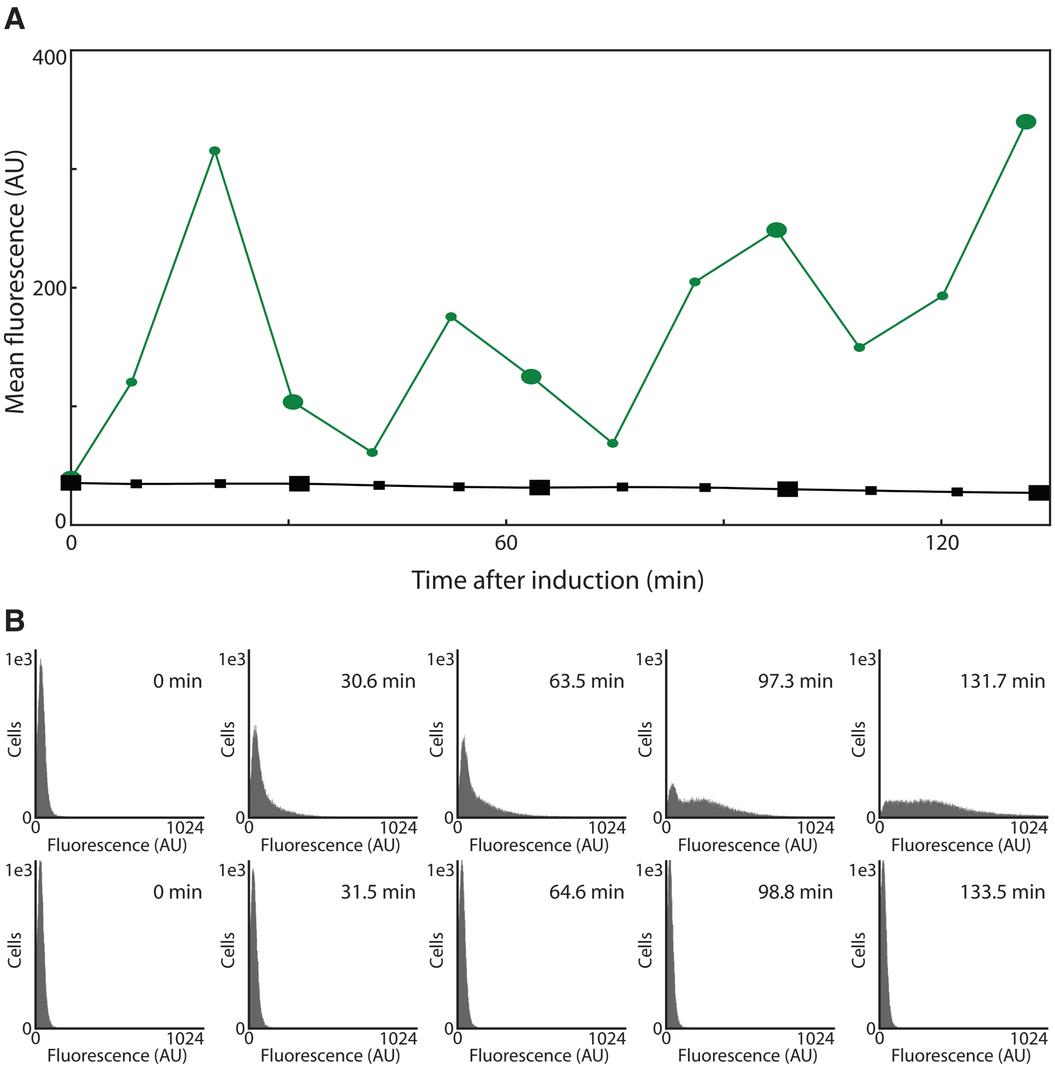

Figure 4.17: Fluorescence dynamics without the activator module. JS006 cells (Δ*araC* Δ*lacI*) were transformed with pJS169 containing the repressor module and pZE24-*yemGFP-LAA*, a pJS167-derived plasmid with the reporter module but without the activator module. No *araC* is present in this strain. (**A**) Time-course flow cytometry, inducing with 0.7% arabinose and 2 mM IPTG at $t = 0$, on the resulting cells (black, square points), and on JS011 cells with both oscillator components (green, circular points) for scale. (**B**) Fluorescence distributions from JS011 cells with both components (top row) and cells with repressor only (bottom row). The larger time points in **A** correspond to the distributions in **B**.

except that the higher-FSC population was not fluorescent with wildtype cells.) The low-FSC subpopulation was assumed to be noncellular and was removed by setting the event threshold on the flow cytometer at FSC $= 20$. Fluorescent detector voltages (and gains if reading in linear mode) were adjusted to the dynamic range appropriate for a particular experiment. For the oscillator characterization experiments, the settings were linear mode, voltage 825–975, gain 8.00–8.25. Any samples that were compared to each other were run under identical settings. For each time point, 25,000–100,000 events were collected at low flow rate.

In our single-cell microscopy experiments, the vast majority of cells oscillated (see Table 4.1). In contrast, in the flow cytometry experiments there was a subpopulation of cells of slightly lower FSC that did not fluoresce (Figs. 4.18 and 4.19). We assume that this subpopulation was essentially static, as the proportion of cells it contained could be seen to be constant over time if the oscillating subpopulation was sufficiently separated. The proportion of this subpopulation was larger at lower inducer concentrations. Inclusion of these cells in flow cytometry data analysis decreases the mean cellular fluorescence proportional to their frequency, but it does not affect the timing of oscillatory peaks (and therefore period determination). In the microscopy experiments, the cells were grown in the presence of inducer before and during loading into the microfluidic device. In contrast, the flow cytometry experiments observed the cells immediately after induction. The cell strain used here has the arabinose transporter genes under native regulation. Since these genes are positively regulated by AraC-arabinose, this gives a positive feedback loop that results in bimodal populations at some arabinose concentrations (Siegele and Hu, 1997). Due to stochastics, some cells will have low initial levels of arabinose transporters and respond poorly to arabinose, while others will have higher initial levels of arabinose transporters and respond well to arabinose. We suggest that the longer exposure to arabinose before observation in the single-cell microscopy experiments results in autoinduction of the arabinose transporters in the great majority of the cells. In contrast, in the flow cytometry experiments at lower arabinose concentrations, a subpopulation of cells does not autoinduce sufficient arabinose transporter expression

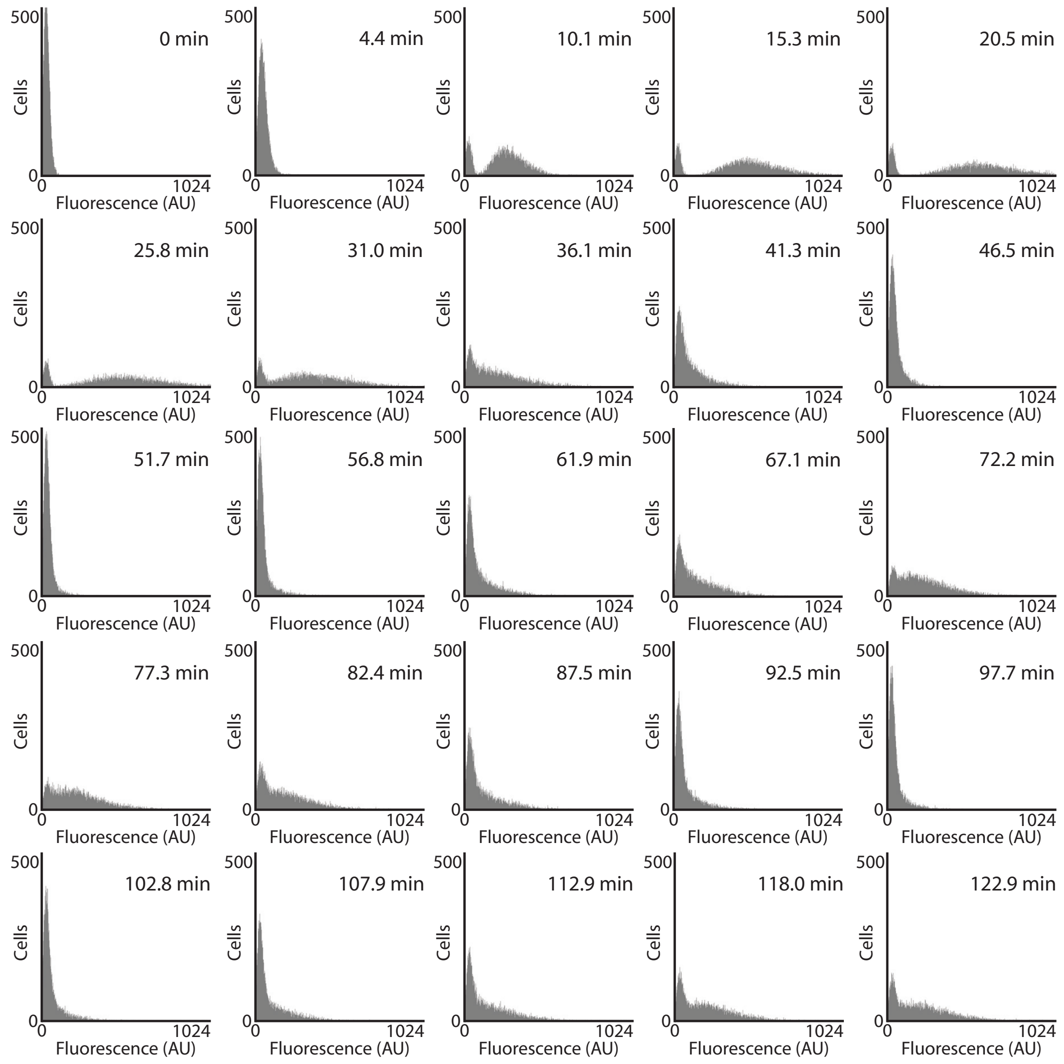

Figure 4.18: Fluorescence distributions from time-course flow cytometry analysis of the 2% arabinose and 2 mM IPTG sample. For each time point collected in this experiment, a histogram of fluorescence values is shown here. (The mean fluorescence value over time is shown in Fig. 4.13.) Fluorescence data were collected in linear mode. Note that the majority of the population oscillates, but there is a small subpopulation that does not fluoresce.

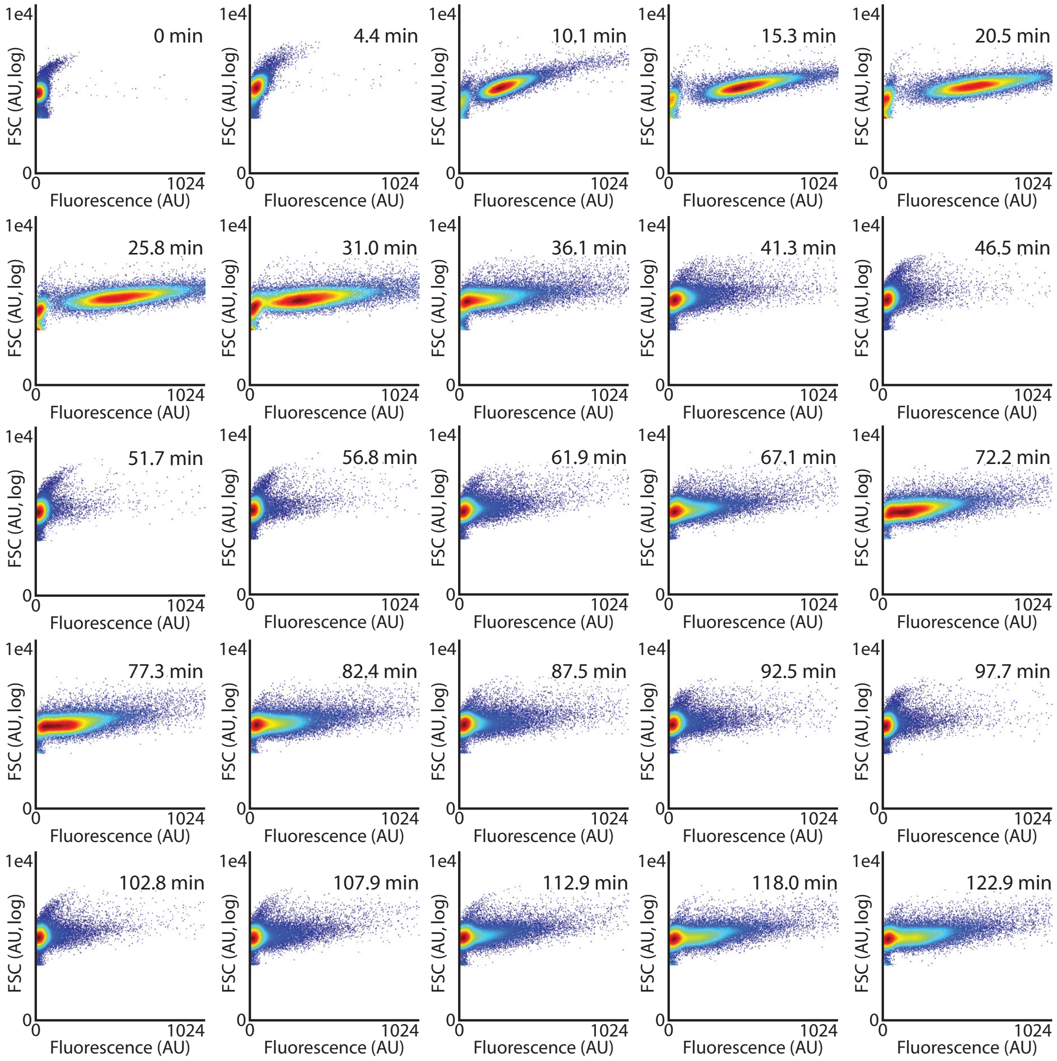

Figure 4.19: FSC versus fluorescence distributions from time-course flow cytometry analysis of the 2% arabinose and 2 mM IPTG sample. For each time point collected in this experiment, a density plot of FSC versus fluorescence is shown. (The mean fluorescence value over time is shown in Fig. 4.13.) Fluorescence data were collected in linear mode, while FSC data were collected in logarithmic mode and low-FSC noise was removed as described in the Flow Cytometry section of Materials and Methods.

to respond to arabinose.

4.5.6 Details of Computational Modeling

Theoretical Predictions of Oscillation Period Versus Inducer Concentrations

We gained insight into and made predictions about the dynamic behavior of our constructed oscillators through the use of mathematical modeling. First, we performed stochastic simulations on the underlying chemical reactions of the oscillators using Gillespie's algorithm (Gillespie, 1977) implemented in custom-written software in the C programming language. Second, we performed deterministic simulations on the corresponding mass-action ODEs using custom-written software in MATLAB. We used these computational models to calculate the oscillation period of the dual-feedback oscillator as a function of both IPTG and arabinose concentration.

Whereas calculation of the oscillation period as a function of IPTG is relatively straightforward, interpreting the models in calculating oscillation period as a function of arabinose is complicated by the existence of two bistable states. The first of these states corresponds to the large-amplitude (and hence long-period) oscillations that are the hallmark of the oscillator. In addition to this state, there is a second state, which for low arabinose levels is a stable limit cycle with very small amplitude and short period. The basin of attraction for this limit cycle appears to be very small, so that it is rarely (if ever) seen stochastically. The intrinsic noise of the system ensures that (i) the probability of reaching this state is small and (ii) when the system does reside in this state, it does not remain there for long. This is illustrated in Fig. 4.20A, which shows the peak-to-peak interval distribution for the stochastic model at 2 mM IPTG and 0.233% arabinose. The distribution is unimodal, with a mean that is equal to the period of the large-amplitude oscillations observed in the deterministic model. As the arabinose concentration increases, the small-amplitude limit cycle goes through a Hopf bifurcation near $[ara] = 1.83\%$, above which the limit cycle becomes a stable fixed point. Stochastically, however, the intrinsic noise creates small-amplitude noise-induced oscillations whenever the system is near the fixed point. The system will most often reside in the large-amplitude oscillation state, but it will occasionally jump to the noise-induced oscillation state for brief periods of time. For example, Fig. 4.21 shows a typical trajectory obtained from stochastic simulations. The basin of attraction for these noise-induced oscillations becomes larger as the arabinose concentration is increased. This can be seen in Fig. 4.20B, C, which show the peak-to-peak interval distributions for $[ara] = 2.1\%$ and $[ara] = 3.5\%$, respectively. Just above the Hopf point (Fig. 4.20B), the system resides mainly in the large-amplitude state, with just a few incursions into the noise-induced oscillatory state. For higher arabinose concentrations, however, the amount of time spent in the small-amplitude state increases due to the enlargement of the basin of attraction (Fig. 4.20C).

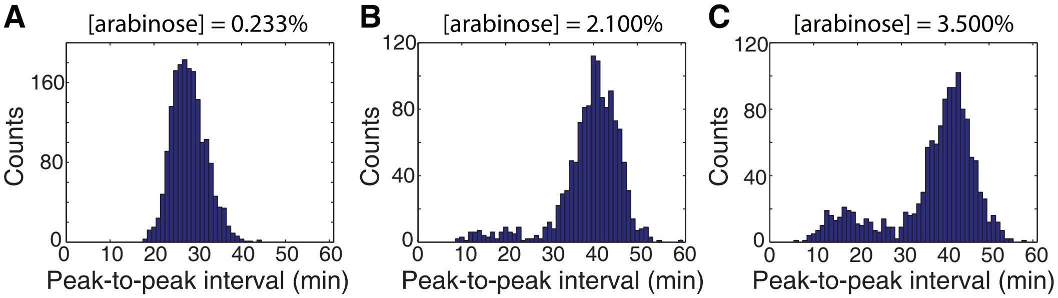

Figure 4.20: Histograms of peak-to-peak intervals for the stochastic model of the oscillator. (**A**) At low arabinose, the distribution of peak-to-peak intervals is unimodal, with a mean equal to the deterministic period. (**B**) When the arabinose concentration increases above 1.83%, bistable oscillations arise. The system stochastically switches between the two forms of oscillation, giving rise to a bimodal peak-to-peak interval distribution. (**C**) As the arabinose concentration increases further, the amount of time spent in the small-amplitude oscillation state increases.

To obtain the stochastic period, we must make a decision as to what statistic of the peak-to-peak distribution to measure. If we were to blindly calculate the mean of the distribution, the period would appear to decrease for increasing arabinose levels, since the time spent in the small-amplitude (and hence short-period) state becomes ever larger. This can be seen in Fig. 4.22, which shows the period of the oscillator as a function of arabinose concentration at 2 mM IPTG. The experimentally-measured values of the

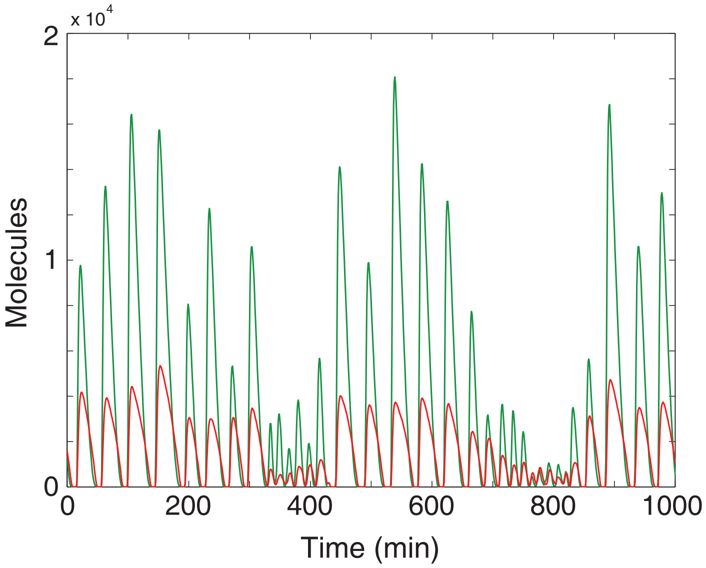

Figure 4.21: An example of bistable oscillations in the stochastic model at high arabinose. Here $[ara] = 3.5\%$ and $[IPTG] = 2$ mM. The green curve is the number of free AraC dimers, while the red curve is the number of free LacI tetramers.

period are shown by green and red points, while the values predicted by the deterministic model (in the large-amplitude oscillatory state) are shown by the blue curve. Also shown are three possible measures of the period taken from the stochastic simulations. The gray triangles represent the value of the period obtained from taking the absolute mean of the peak-to-peak distribution. As expected, that measure of the period decreases at high arabinose levels.

Another possible way to measure the mean period of the stochastic simulations is to ignore the small-amplitude oscillations and concentrate instead on the upper half of the peak-to-peak distribution. Roughly speaking, this can be done by ignoring all intervals that are less than 30 min (provided the arabinose concentration is greater than 1.0%). Such a measure is roughly tantamount to measuring the mode of the whole distribution, provided more time is spent in the large-amplitude state. The gray squares in Fig. 4.22 show this measure of the period, and they match well with the deterministic period.

It is interesting to point out that many of the experimentally-measured values of

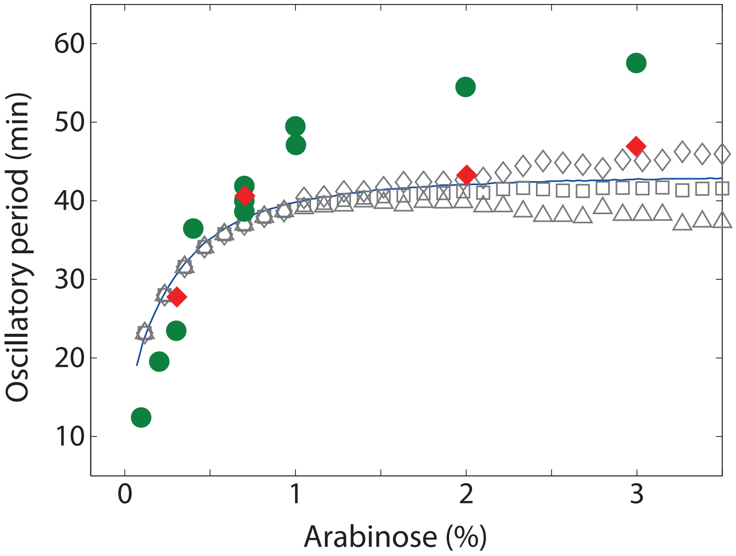

Figure 4.22: The period of oscillation as a function of arabinose concentration at 2 mM IPTG. Shown are the experimentally-measured periods obtained through time-lapse flow cytometry (green circles) or single-cell microscopy (red diamonds), the periods predicted by the deterministic model (blue curve), and the periods predicted by the stochastic model, measured in three ways (gray symbols). The triangles are the raw mean of the peak-to-peak distributions; the squares are the mean of the right-hand side of the distributions (roughly the mode); and the diamonds are the mean of peak-to-peak distributions in which only large-amplitude peaks are considered (such that small-amplitude oscillations are considered part of one long-period oscillation).

the period in Fig. 4.22 were obtained through time-lapse flow cytometry. Because the amplitude of the long-period state is so much higher than the short-period state, it is unlikely that small-amplitude oscillations would be detectable even if they were occurring. Therefore, one final measure of the period may also be relevant. Time spent in the small-amplitude region could be considered as additional time between the two large-amplitude peaks which border it. If the small-amplitude oscillations are not considered as peaks and the resulting gaps are added to the interval between the bordering peaks, the peak-to-peak distribution will be skewed toward the long-period regime. The gray diamonds in Fig. 4.22 show the resulting period of the stochastic simulations measured in this way.

We currently have no experimental evidence that bistable oscillations occur in the oscillator. As mentioned above, small-amplitude oscillations will probably be washed out of any measure obtained through flow cytometry. Additionally, our single-cell measurements obtained through microscopy at high arabinose concentrations have not revealed any cells oscillating with a low period. However, due to the low number of cells present in the imaging chamber, combined with the limited amount of time that reliable images can be taken, it may be that we have not been fortunate enough to observe such oscillations yet. It is also possible that the stochastic model is either in the wrong parameter regime or is missing an important component of the network that would preclude bistability. This remains a subject for further investigation.

Theoretical Predictions of Oscillation Period Versus Temperature

It is well-known that the division period of *E. coli* depends on temperature according to the formula:

$$\tau_{cc}\left(T\right) = \tau_{ref} \exp\left[\Theta_{cc}\left(1/T - 1/T_{ref}\right)\right], \tag{4.1}$$

where $\tau_{cc}\left(T\right)$ is the division period as a function of temperature, T, in Kelvin; τ_{ref} is a reference time at the reference temperature, T_{ref}; and Θ_{cc} is a constant. We measured the doubling times of the JS011 strain at various temperatures and calculated $\Theta_{cc} \approx 8300$K.

In order to predict the frequency of oscillations at various temperatures in the model, each rate constant must be multiplied by a similar Arrhenius constant, such that

$$k_i = k_{ref} \exp\left[-\Theta_i \left(1/T - 1/T_{ref}\right)\right], \tag{4.2}$$

where k_i is the i^{th} rate constant in the model and Θ_i is the constant associated with that reaction. Each reaction will have a different value for Θ_i, and these constants are, in general, not known. However, if we assume that $\Theta_i \approx \Theta_{cc} \forall i$, then calculating the temperature dependence of the model is equivalent to scaling time by the Arrhenius factor, since all affected model constants have an inverse time as part of their units. Therefore, we can determine the period of the model from the equation:

$$P\left(T\right) = P_{ref} \exp\left[\Theta_{cc} \left(1/T - 1/T_{ref}\right)\right], \tag{4.3}$$

where P is the period and P_{ref} is the period at $T = T_{ref}$. Fig. 4.2C shows our prediction of the period based on the reference temperature $T_{ref} = 30$°C and reference period $P_{ref} = 69$ min.

Negative Feedback-Only Oscillations

Even without the positive feedback loop, the model of our circuit exhibits oscillations. However, their properties may depend on the specific way in which the negative feedback-only system is constructed. In particular, we find that the forward rate of the DNA looping reaction plays an important role. We illustrate this with three variants of a negative feedback-only system, each with a different forward rate of DNA looping. For all variants, we set the number of plasmids that produce AraC to zero to ensure that AraC is not produced and that repressor does not interact with DNA residing on those plasmids. We also increase the basal transcription rate of LacI by a factor of $\sim$30 compared to the dual-feedback model.

Our first example of a negative feedback-only system is characterized by a lack of DNA looping (forward DNA looping rate is zero) and roughly corresponds to our experimental negative feedback-only system. A typical time series obtained from this stochastic model is shown in Fig. 4.23A. The amplitude of these oscillations is relatively small, and the LacI concentration does not go all the way down to zero in the troughs of oscillations. The oscillations are noticeably less regular than those in the original dual-feedback model. In fact, for $[IPTG] > 0.2$ mM, the oscillations decay in the deterministic version of the model and are persistent only in stochastic simulations. However, for $[IPTG] < 0.2$ mM, large-amplitude oscillations are observed (not shown). We examined the system for a number of values of $[IPTG]$ up to 1 mM and found that the characteristic period of oscillations was remarkably less tunable than in the dual-feedback oscillator model (Fig. 4.24). These features are consistent with our experimental findings for the $\mathrm{p_{LlacO\text{-}1}}$ promoter that lacks DNA looping and is transcribed at a high level.

In our second example of a negative feedback-only system, DNA looping is present with the same forward rate as in the original dual-feedback model. In this case, we observe larger and more regular LacI oscillations for a wide range of IPTG concentrations in which LacI goes to zero in the troughs of oscillations (Fig. 4.23B). However, the oscillation period is still not sensitive to varying IPTG concentration (Fig. 4.24).

Our third example of a negative feedback-only system uses a forward rate of DNA looping that is 1,000 times larger than our nominal value for the dual-feedback model. In this case, we again observe large-amplitude and regular LacI oscillations for a wide range of IPTG concentrations (Fig. 4.23C). The period of these oscillations is somewhat longer than for the original value of forward DNA looping rate and remains only weakly tunable with respect to varying IPTG concentration (Fig. 4.24).

We conclude from these simulations that negative feedback-only systems may lead to oscillations. However, the properties of these oscillations vary depending on system parameters. The experimental negative feedback-only system oscillates only weakly, in agreement with the model without DNA looping. The addition of a pos-

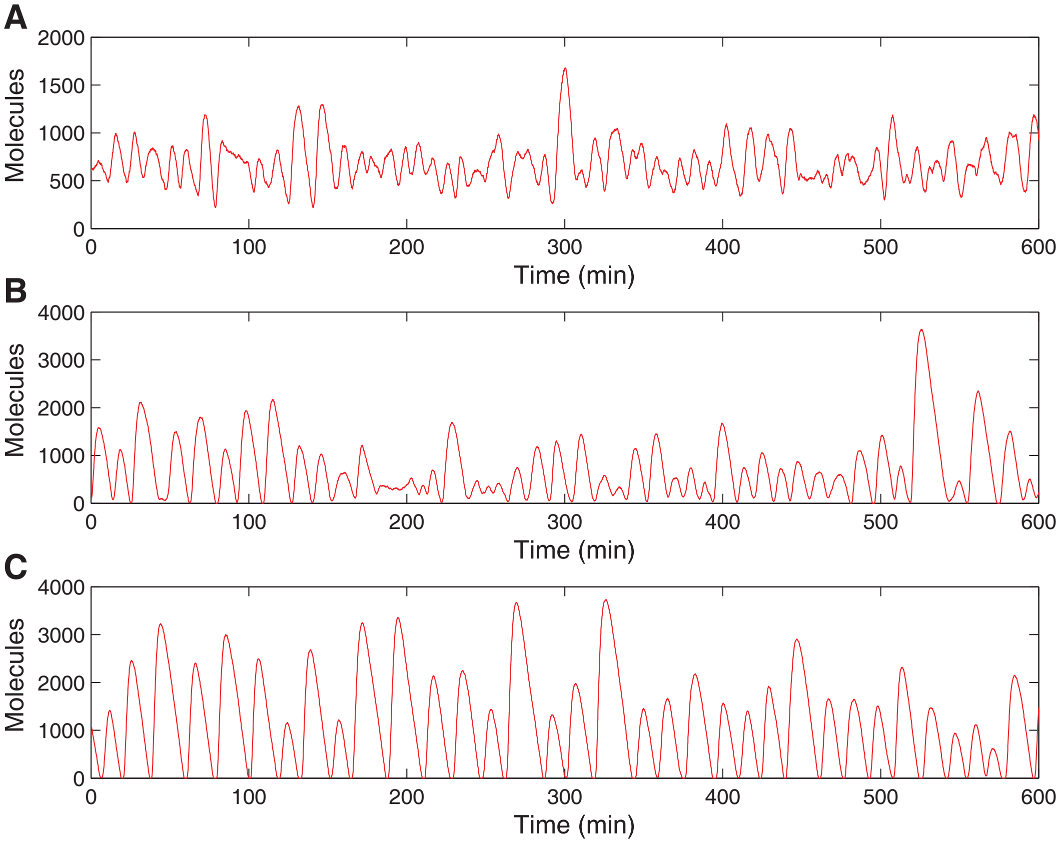

Figure 4.23: Characteristic time series of free LacI tetramer obtained from negative feedback-only stochastic models. Here, the basal transcription rate of LacI has been increased by a factor of ~30 compared to the dual-feedback model, and $[IPTG] = 2.0$ mM. Negative feedback-only systems were tested for three different values of the forward DNA looping rate, k_ℓ: (**A**) $k_\ell = 0$, where DNA looping is not present; (**B**) $k_\ell = 0.36$ min^{-1}, the value used in the dual-feedback model; (**C**) $k_\ell = 360$ min^{-1}.

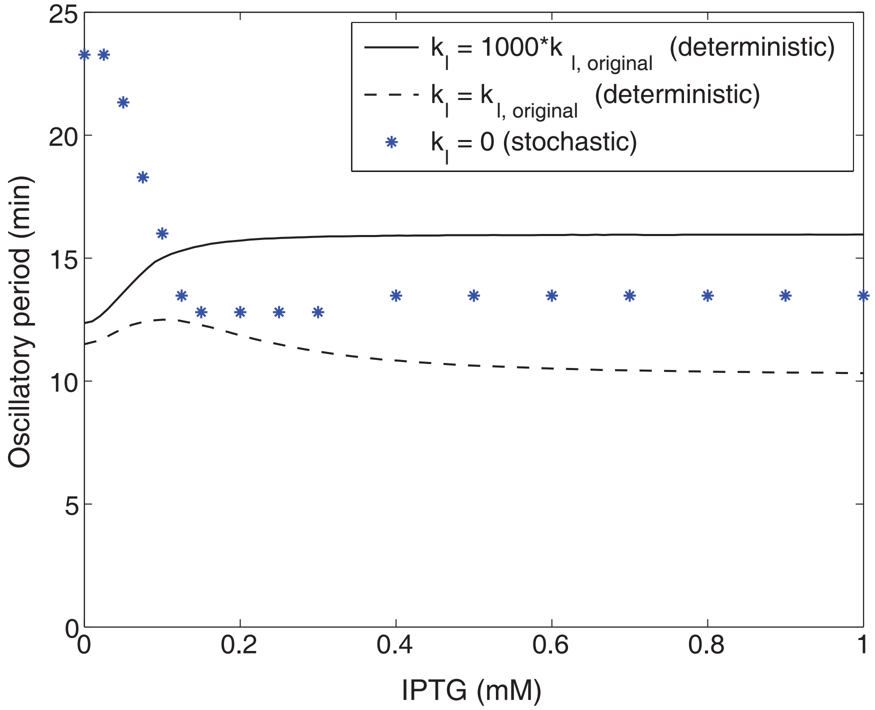

Figure 4.24: Oscillation period versus IPTG concentration for the negative feedback-only simulations shown in Fig. 4.23. $k_{\ell,\text{original}}$ is the forward rate of DNA looping used in the dual-feedback model. As IPTG concentration is scanned, the period varies less than what was seen experimentally in the dual-feedback system. For the $k_\ell = 0$ case, oscillations in the deterministic model decay at $[IPTG] > 0.2$ mM and are only observed in stochastic simulations; therefore, we define the period as the maximum in the power spectrum of the stochastic trajectory.

itive feedback loop in this case leads to an increased robustness of such oscillations. However, due to other possible differences between the $\text{p}_{\text{lac/ara-1}}$ promoter in the experimental dual-feedback system and the $\text{p}_{\text{LlacO-1}}$ promoter in the experimental negative feedback-only system, further experimental work is needed to calibrate the model and test these predictions. Furthermore, it appears that for other experimental implementations, negative feedback-only systems may by themselves generate large-amplitude robust oscillations. A quest for such simplified designs is currently underway.

Negative Feedback Delay and Robustness

The formulation of design principles that lead to the creation of robust gene circuits is a major goal in synthetic biology. Robust circuits are insensitive to the precise tuning of system parameters and thus can cope with the natural variability found *in vivo* (Elowitz et al., 2002). The model of the bacterial oscillator proposed here suggests that delay in negative feedback may be key in explaining the experimentally-observed robustness of oscillations. Such delay may arise from a variety of intermediate steps, such as protein folding and multimerization, which combine into a net delay that promotes oscillatory behavior. The sharpness of a distributed delay may also be relevant in this regard (Rateitschak and Wolkenhauer, 2007).

The relationship between feedback delay and robustness can be simply traced in the case of certain delayed negative feedback gene circuits. Such circuits include the negative feedback oscillator described here with constitutive activator and no positive feedback. A minimal model in this case is the first-order delay-differential equation,

$$\frac{dy\left(t\right)}{dt}=\frac{K}{\left[1+\frac{y(t-\tau)}{C_0}\right]^n}-\gamma y\left(t\right), \tag{4.4}$$

with $y\left(t\right)$ being the amount of some repressor at time t, K being the unrepressed production rate, C_0 being an affinity constant, and γ being a first-order degradation rate. Analytical results for such delayed negative feedback systems are well-known (Bliss et al., 1982; Bratsun et al., 2005; Mackey and Nechaeva, 1995), and we do not re-derive them here. If we define y_0 to be the unique fixed point for Eqn. 4.4, the bifurcation diagram can be represented in terms of the variables $\gamma\tau$ and y_0/C_0 (Fig. 4.25). An important conclusion derived from this bifurcation diagram is that increasing the delay (for some fixed γ) expands the region of parameter space in which the system exhibits stable oscillations. In this sense, increasing intracellular delay leads to enhanced robustness of stable oscillations in delayed negative feedback systems.

Although our full dual-feedback model contains richer dynamics than the delayed negative feedback model described above, conceptual similarity between their basic mechanisms suggests that increasing delay will enhance robustness. The robustness of the full model was numerically explored by probing nearby parameter sets and determining if these sets display oscillatory behavior (see Fig. 4.26 for details of the numerical analysis). One result of this numerical investigation is that the fraction of accessible parameter space (located near the listed parameter values) exhibiting stable oscillations is above 50% for most points taken along the arabinose transect at 2 mM IPTG. This result should be contrasted to the exponentially small (in the number of varied parameters) hypervolume that could be expected when multiple parameters must be accurately and independently tuned. A second result of this numerical investigation, which corroborates our discussion of the above minimal model, is the tendency for an increased robustness with increasing effective delay.

While we have not rigorously proven a general causal relation between delay and enhanced robustness of oscillations, the above analytic and numerical evidence suggests that such a relation holds when the core of a gene oscillator comprises a delayed negative feedback loop. There may be value in basing the designs of future synthetic gene oscillators on such a principle, particularly if methods arise that allow the engineering of a sharply distributed delay between transcription and feedback.

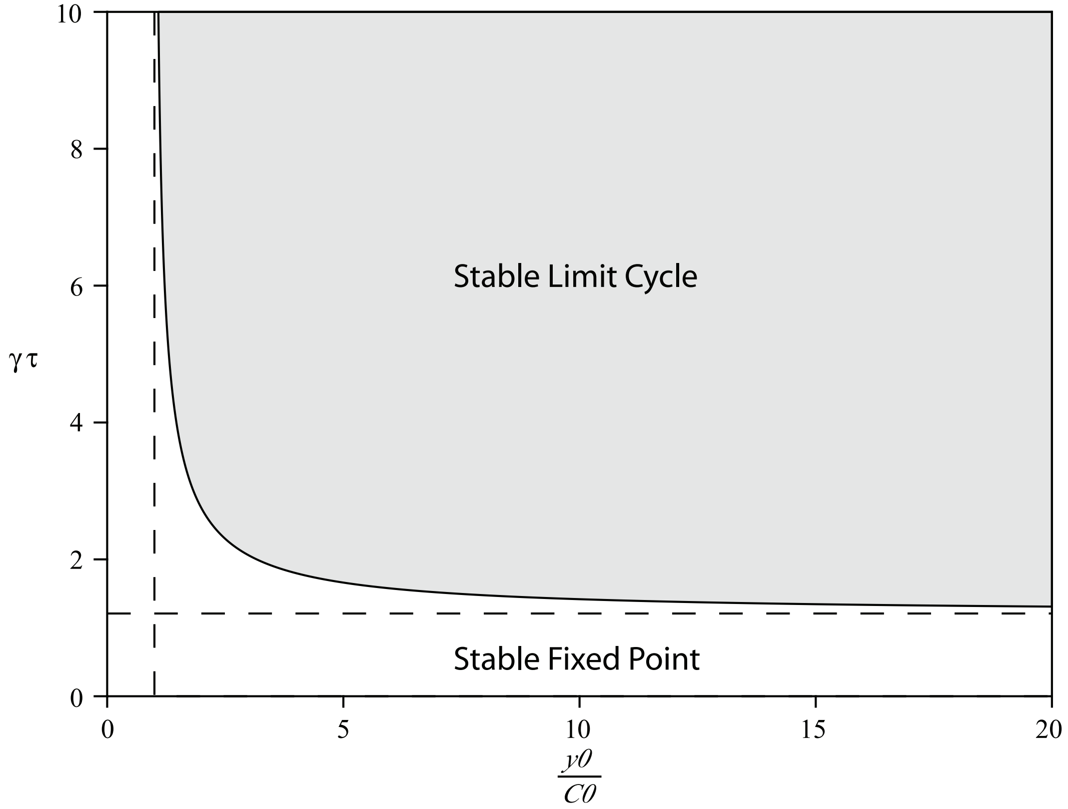

Figure 4.25: Bifurcation diagram for the modeled delayed negative feedback system. In this case, $n = 2$. The bifurcation boundary approaches the asymptotes (marked with dashed lines) defined by $\gamma\tau = \arccos(-1/n)/\sqrt{n^2-1}$ and $y_0/C_0 = 1/(n-1)$. Note that the bifurcation boundary monotonically decreases in y_0/C_0 with increasing $\gamma\tau$. Since y_0 is independent of τ (but not γ), this monotonicity implies that the region of parameter space that supports stable oscillations monotonically increases with increasing τ and fixed γ.

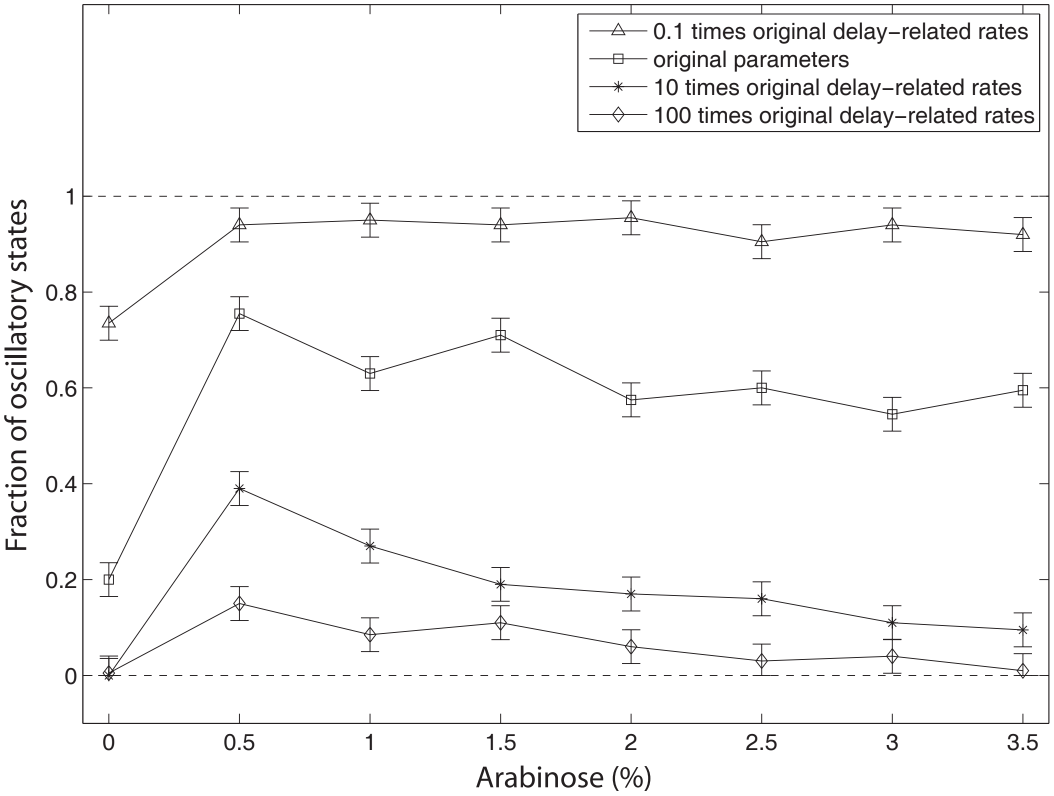

Figure 4.26: A numerical investigation of the effect of changing intracellular delay on robustness. Nearby parameter space in the full dual-feedback model was probed for oscillatory behavior. All parameters were randomly sampled independently and uniformly (in log-space) between half and double their listed values. This approach was chosen to avoid preferential treatment of a particular set of the 21 varied parameters (Gutenkunst et al., 2007). A computed trajectory was determined to not be oscillatory if, after a transient of 2,000 min, the maximal variation in the number of folded monomeric activator was less than 0.1 in a subsequent 400 min of simulation. The plot displays the fraction of oscillatory states for varying levels of arabinose and 2.0 mM IPTG. This procedure was repeated for different mean values of selected delay-related rates by multiplying the parameter values for the forward rates of folding, dimerization, and tetramerization by a common value (see fig. legend). Error bars were set to the maximum standard deviation $\sigma_{max} = 0.5/\sqrt{N}$ for the average of $N = 200$ Bernoulli trials. The data supports our suggestion that decreasing the delay in the system tends to reduce the fraction of oscillatory states in nearby parameter space, while increasing the delay has the opposite effect.

4.6 Acknowledgements

Chapter 4 contains material originally published as Stricker, J.*, Cookson, S.*, Bennett, M. R.*, Mather, W. H., Tsimring, L. S., and Hasty, J., 2008: A fast, robust and tunable synthetic gene oscillator. *Nature*. doi:10.1038/nature07389. (*equal contribution). Copyright permission to republish here was granted by Nature Publishing Group.

Chapter 5

Summary

Realizing the potential of synthetic biology rests on the development of new tools both for the acquisition and processing of data from large samples of individual cells (Thompson et al., 2004; Tourovskaia et al., 2005). In particular, the ability to perform long-duration experiments that yield consistent single-cell data is critical for characterizing synthetic biological systems and generating computational models with predictive abilities. Microfluidic technology continues to demonstrate great promise in re-creating *in vivo*-like microenvironments for studying cellular processes. With their capabilities to constrain and dynamically control the cellular growth environment, microfluidic devices support real-time and long-term measurement of expression profiles within fundamental gene networks. Such a wealth of expression data will allow researchers to understand the intricate web of gene-regulatory dynamics that lead to biological function. Through computational modeling of tractable synthetic regulatory control circuits, these insights will lead to an improved quantitative understanding of biological control modules and their incorporations within complex native networks.

In Chapter 2, we demonstrated the utility of a novel microchemostat designed for monitoring cellular dynamics in *S. cerevisiae* over many generations by constraining colony growth to a monolayer (Cookson*, Ostroff*, Pang*, Volfson, and Hasty, 2005, *equal contribution). This device offers a number of significant technical advantages over alternate methods such as flow cytometry and traditional microscopy. Flow cytometry provides a snapshot of single-cell data but does not offer the ability to track any given cell. These population measurements provide very useful information about the steady-state behavior of biological networks, but they inherently sacrifice details at the single-cell dynamical level. Traditional microscopy assays yield useful and very detailed information on the dynamical behavior of a small number of cells but typically run only for a short time period and sacrifice the ability to generate good statistics over a population. In contrast, the TμC we have designed and developed allows for long-term single-cell dynamical measurements over a large population. Within the context of systems biology, the ability to generate such data at the single-cell level will aid in the development of predictive dynamical modeling (Chen et al., 2004) and facilitate the application of novel approaches such as the use of frequency-space analysis to quantify the variability inherent in gene expression (Simpson et al., 2003). The unique capability of the TμC for studying both the dynamics and the variability of biological processes within a population of living cells represents an important step toward bringing quantitative single-cell data to the field of systems biology.

In Chapter 3, we compared the dynamics of *E. coli* colony expansion in a pseudo-2D microfluidic channel with continuum modeling and DES to reveal a new mechanism of cell ordering within dense populations (Volfson*, Cookson*, Hasty, and Tsimring, 2008, *equal contribution). We demonstrated that purely biomechanical short-range interactions arising from the growth and division of individual cells can lead to highly ordered structures in a constrained environment. Specifically, the expansion flow generated by cellular growth triggers the formation of orientational order in the population, transitioning the colony microstructure from an isotropic disordered phase to an ordered nematic phase characterized by the alignment of rod-like cells. This phenomenon is fundamentally different from the nematic transition in liquid crystals and polymers (Doi and Edwards, 1986) and vibrated granular rods (Blair et al., 2003; Narayan et al., 2006), where ordering is primarily driven by the combination of steric exclusion and fluctuations. Because the mechanism of the ordering transition reported here is related to cell growth, it should be ubiquitous in “living granular matter.”

Finally, in Chapter 4 we constructed and characterized a fast, robust, and tunable genetic oscillator in *E. coli* by implementing a previously modeled regulatory architecture comprising linking positive and negative feedback loops (Stricker*, Cookson*, Bennett*, Mather, Tsimring, and Hasty, 2008, *equal contribution). We used microfluidics and flow cytometry to investigate expression dynamics within single cells carrying this engineered gene circuit, and we used computational modeling to demonstrate that the key design principle for robust operation is a time delay in the negative feedback loop. In the context of synthetic biology, our findings indicate that caution must be exercised when making simplifying assumptions in the design of engineered gene circuits. We found that a full model of the system that takes into account intermediate steps in the production of functional protein such as DNA looping, protein-DNA binding, DNA transcription, mRNA translation, protein folding, protein multimerization, and enzymatic degradation is essential. The reason for this lies not only in the time scales of the system but also in the sequential timing of events. These intermediate steps combine to form an effective delay in the system, and their inclusion within our model greatly increases the robustness of oscillation (Rateitschak and Wolkenhauer, 2007; Mackey and Glass, 1977; Jaeger and Reinitz, 2006) to match our experimental data.

Together, these studies demonstrate the utility of combining quantitative experimentation with computational modeling to elucidate novel properties of biological systems. Specifically, we have shown how microfluidic technology can be used to track long-term dynamic behavior in single cells, which can be compared to computational predictions to reveal key design criteria in the construction of functional regulatory networks. The synthetic biology approach will become increasingly effective as microfluidic technology continues to produce innovative cell assays. The field will also gain strength from technical advances in other measurement techniques designed to quantify the dynamics of cellular interactions. For example, the ability to measure reaction rates of chemical processes *in vivo* will enable the more accurate formulation of computational models of gene regulation. In addition, new assays that reveal the localization of these reactions will lead to investigations into the effects of cellular compartmentalization and transport on regulatory processes. Finally, an expansion of the currently limited set of well-characterized regulatory components that can be used as building blocks for engineered synthetic circuits will permit the construction of increasingly complex and functional networks.

As the tools of synthetic biology evolve, so too will the techniques needed to translate discoveries in this field into applications. Advances in personal genomics will provide the technology to cheaply and rapidly sequence the genome of any individual. Comprehensive models can then be developed to use this information to predict interactions between new constructs and potential target cells. Finally, improvements in gene delivery methods will allow for the reliable integration of genomic therapies into specific cells. Together, these advances will enable the application of synthetic gene networks to both diagnose and treat human disease. One can envision the eventual development of sensor circuits that alter the expression of reporter proteins upon recognizing environmental conditions and delivery circuits that modulate the production of therapeutic proteins depending on the states of cells. Such an integration of synthetic biology with personal genomics and gene therapy has the potential to revolutionize drug therapy and realize the promise of personalized medicine in treating disease.

References

Adams, R., and Bischof, L., 1994: Seeded region growing. *IEEE Trans. Pattern Anal. Mach. Intell.*, **16**(6), 641–7.

Andersen, J. B., Sternberg, C., Poulsen, L. K., Bjørn, S. P., Givskov, M., and Molin, S., 1998: New unstable variants of green fluorescent protein for studies of transient gene expression in bacteria. *Appl. Environ. Microbiol.*, **64**(6), 2240–6.

Andrianantoandro, E., Basu, S., Karig, D. K., and Weiss, R., 2006: Synthetic biology: new engineering rules for an emerging discipline. *Mol. Syst. Biol.*, **2**(2006.0028), msb4100073–1–14.

Ashton, R., Padala, C., and Kane, R. S., 2003: Microfluidic separation of DNA. *Curr. Opin. Biotechnol.*, **14**(5), 497–504.

Atkinson, M. R., Savageau, M. A., Myers, J. T., and Ninfa, A. J., 2003: Development of genetic circuitry exhibiting toggle switch or oscillatory behavior in *Escherichia coli*. *Cell*, **113**(5), 597–607.

Atlung, T., Christensen, B. B., and Hansen, F. G., 1999: Role of the Rom protein in copy number control of plasmid pBR322 at different growth rates in *Escherichia coli* K-12. *Plasmid*, **41**(2), 110–9.

Baba, T., Ara, T., Hasegawa, M., Takai, Y., Okumura, Y., Baba, M., Datsenko, K. A., Tomita, M., Wanner, B. L., and Mori, H., 2006: Construction of *Escherichia coli* K-12 in-frame, single-gene knockout mutants: the Keio collection. *Mol. Syst. Biol.*, **2**(2006.0008), msb4100050–1–11.

Balaban, N. Q., Merrin, J., Chait, R., Kowalik, L., and Leibler, S., 2004: Bacterial persistence as a phenotypic switch. *Science*, **305**(5690), 1622–5.

Balagaddé, F. K., You, L., Hansen, C. L., Arnold, F. H., and Quake, S. R., 2005: Long-term monitoring of bacteria undergoing programmed population control in a microchemostat. *Science*, **309**(5731), 137–40.

Barkai, N., and Leibler, S., 2000: Circadian clocks limited by noise. *Nature*, **403**(6767), 267–8.

Bartek, J., Lukas, C., and Lukas, J., 2004: Checking on DNA damage in S phase. *Nat. Rev. Mol. Cell Biol.*, **5**(10), 792–804.

Bassler, B. L., 2002: Small talk: cell-to-cell communication in bacteria. *Cell*, **109**(4), 421–4.

Basu, S., Gerchman, Y., Collins, C. H., Arnold, F. H., and Weiss, R., 2005: A synthetic multicellular system for programmed pattern formation. *Nature*, **434**(7037), 1130–4.

Begley, T. J., and Samson, L. D., 2004: Network responses to DNA damaging agents. *DNA Repair (Amst)*, **3**(8–9), 1123–32.

Bendib, S., and Français, O., 2001: Analytical study of microchannel and passive microvalve "application to micropump simulator". In *Design, Characterisation, and Packaging for MEMS and Microelectronics 2001*, 283–91. Adelaide, Australia.

Bennett, M. R., Pang, W. L., Ostroff, N. A., Baumgartner, B. L., Nayak, S., Tsimring, L. S., and Hasty, J., 2008: Metabolic gene regulation in a dynamically changing environment. *Nature*, **454**(7208), 1119–22.

Bird, R. B., Stewart, W. E., and Lightfoot, E. N., 2002: *Transport Phenomena*. J. Wiley, New York, 2nd edition.

Blair, D. L., Neicu, T., and Kudrolli, A., 2003: Vortices in vibrated granular rods. *Phys. Rev. E Stat. Phys. Plasmas Fluids Relat. Interdiscip. Topics*, **67**(3), 031303–1–6.

Bliss, R. D., Painter, P. R., and Marr, A. G., 1982: Role of feedback inhibition in stabilizing the classical operon. *J. Theor. Biol.*, **97**(2), 177–93.

Bratsun, D., Volfson, D., Tsimring, L. S., and Hasty, J., 2005: Delay-induced stochastic oscillations in gene regulation. *Proc. Natl. Acad. Sci. U. S. A.*, **102**(41), 14593–8.

Breeden, L. L., 2003: Periodic transcription: a cycle within a cycle. *Curr. Biol.*, **13**(1), R31–8.

Chang, A. C. Y., and Cohen, S. N., 1978: Construction and characterization of amplifiable multicopy DNA cloning vehicles derived from the p15A cryptic miniplasmid. *J. Bacteriol.*, **134**(3), 1141–56.

Chen, K. C., Calzone, L., Csikasz-Nagy, A., Cross, F. R., Novak, B., and Tyson, J. J., 2004: Integrative analysis of cell cycle control in budding yeast. *Mol. Biol. Cell*, **15**(8), 3841–62.

Chiu, D. T., Jeon, N. L., Huang, S., Kane, R. S., Wargo, C. J., Choi, I. S., Ingber, D. E., and Whitesides, G. M., 2000: Patterned deposition of cells and proteins onto surfaces by using three-dimensional microfluidic systems. *Proc. Natl. Acad. Sci. U. S. A.*, **97**(6), 2408–13.

Cookson, S.*, Ostroff, N.*, Pang, W. L.*, Volfson, D., and Hasty, J., 2005: Monitoring dynamics of single-cell gene expression over multiple cell cycles. *Mol. Syst. Biol.*, **1**, msb4100032–E1–6. (*equal contribution).

Cormack, B. P., Valdivia, R. H., and Falkow, S., 1996: FACS-optimized mutants of the green fluorescent protein (GFP). *Gene*, **173**(1 Spec No), 33–8.

Crocker, J. C., and Grier, D. G., 1996: Methods of digital video microscopy for colloidal studies. *J. Colloid Interface Sci.*, **179**(1), 298–310. See also "Particle tracking using IDL" online tutorial developed by E. Weeks, http://www.physics.emory.edu/ weeks/idl/.

Datsenko, K. A., and Wanner, B. L., 2000: One-step inactivation of chromosomal genes in *Escherichia coli* K-12 using PCR products. *Proc. Natl. Acad. Sci. U. S. A.*, **97**(12), 6640–5.

Davies, D. G., Parsek, M. R., Pearson, J. P., Iglewski, B. H., Costerton, J. W., and Greenberg, E. P., 1998: The involvement of cell-to-cell signals in the development of a bacterial biofilm. *Science*, **280**(5361), 295–8.

de Gennes, P. G., and Prost, J., 1993: *The Physics of Liquid Crystals*, volume 83 of *The international series of monographs on physics*. Clarendon, Oxford, 2nd edition.

Dertinger, S. K. W., Chiu, D. T., Jeon, N. L., and Whitesides, G. M., 2001: Generation of gradients having complex shapes using microfluidic networks. *Anal. Chem.*, **73**(6), 1240–6.

Doi, M., and Edwards, S. F., 1986: *The Theory of Polymer Dynamics*, volume 73 of *The international series of monographs on physics*. Clarendon, Oxford.

Donlan, R. M., 2002: Biofilms: microbial life on surfaces. *Emerg. Infect. Dis.*, **8**(9), 881–90.

Duffy, D. C., McDonald, J. C., Schueller, O. J. A., and Whitesides, G. M., 1998: Rapid prototyping of microfluidic systems in poly(dimethylsiloxane). *Anal. Chem.*, **70**(23), 4974–84.

Duffy, D. C., Schueller, O. J. A., Brittain, S. T., and Whitesides, G. M., 1999: Rapid prototyping of microfluidic switches in poly(dimethyl siloxane) and their actuation by electro-osmotic flow. *J. Micromech. Microeng.*, **9**(3), 211–7.

Egilmez, N. K., and Jazwinski, S. M., 1989: Evidence for the involvement of a cytoplasmic factor in the aging of the yeast *Saccharomyces cerevisiae*. *J. Bacteriol.*, **171**(1), 37–42.

Elowitz, M. B., and Leibler, S., 2000: A synthetic oscillatory network of transcriptional regulators. *Nature*, **403**(6767), 335–8.

Elowitz, M. B., Levine, A. J., Siggia, E. D., and Swain, P. S., 2002: Stochastic gene expression in a single cell. *Science*, **297**(5584), 1183–6.

Endy, D., 2005: Foundations for engineering biology. *Nature*, **438**(7067), 449–53.

Fu, A. Y., Chou, H. P., Spence, C., Arnold, F. H., and Quake, S. R., 2002: An integrated microfabricated cell sorter. *Anal. Chem.*, **74**(11), 2451–7.

Fung, E., Wong, W. W., Suen, J. K., Bulter, T., Lee, S.-G., and Liao, J. C., 2005: A synthetic gene-metabolic oscillator. *Nature*, **435**(7038), 118–22.

Gardner, T. S., Cantor, C. R., and Collins, J. J., 2000: Construction of a genetic toggle switch in *Escherichia coli*. *Nature*, **403**(6767), 339–42.

Gardner, T. S., di Bernardo, D., Lorenz, D., and Collins, J. J., 2003: Inferring genetic networks and identifying compound mode of action via expression profiling. *Science*, **301**(5629), 102–5.

Gerland, U., Moroz, J. D., and Hwa, T., 2002: Physical constraints and functional characteristics of transcription factor-DNA interaction. *Proc. Natl. Acad. Sci. U. S. A.*, **99**(19), 12015–20.

Gillespie, D. T., 1977: Exact stochastic simulation of coupled chemical-reactions. *J. Phys. Chem.*, **81**(25), 2340–61.

Groisman, A., Enzelberger, M., and Quake, S. R., 2003: Microfluidic memory and control devices. *Science*, **300**(5621), 955–8.

Groisman, A., Lobo, C., Cho, H., Campbell, J. K., Dufour, Y. S., Stevens, A. M., and Levchenko, A., 2005: A microfluidic chemostat for experiments with bacterial and yeast cells. *Nat. Methods*, **2**(9), 685–9.

Gui, L. C., and Merzkirch, W., 1996: A method of tracking ensembles of particle images. *Exp. Fluids*, **21**(6), 465–8.

Gutenkunst, R. N., Waterfall, J. J., Casey, F. P., Brown, K. S., Myers, C. R., and Sethna, J. P., 2007: Universally sloppy parameter sensitivities in systems biology models. *PLoS Comput. Biol.*, **3**(10), 1871–8.

Haberman, R., 1998: *Elementary Applied Partial Differential Equations: with Fourier Series and Boundary Value Problems*. Prentice Hall, Upper Saddle River, NJ, 3rd edition.

Hansen, C., and Quake, S. R., 2003: Microfluidics in structural biology: smaller, faster . . . better. *Curr. Opin. Struct. Biol.*, **13**(5), 538–44.

Hartwell, L. H., Szankasi, P., Roberts, C. J., Murray, A. W., and Friend, S. H., 1997: Integrating genetic approaches into the discovery of anticancer drugs. *Science*, **278**(5340), 1064–8.

Hasty, J., Dolnik, M., Rottschäfer, V., and Collins, J. J., 2002a: Synthetic gene network for entraining and amplifying cellular oscillations. *Phys. Rev. Lett.*, **88**(14), 148101.

Hasty, J., McMillen, D., and Collins, J. J., 2002b: Engineered gene circuits. *Nature*, **420**(6912), 224–30.

Hasty, J., McMillen, D., Isaacs, F., and Collins, J. J., 2001: Computational studies of gene regulatory networks: *in numero* molecular biology. *Nat. Rev. Genet.*, **2**(4), 268–79.

Hinsa, S. M., Espinosa-Urgel, M., Ramos, J. L., and O'Toole, G. A., 2003: Transition from reversible to irreversible attachment during biofilm formation by *Pseudomonas fluorescens* WCS365 requires an ABC transporter and a large secreted protein. *Mol. Microbiol.*, **49**(4), 905–18.

Hong, J. W., Studer, V., Hang, G., Anderson, W. F., and Quake, S. R., 2004: A nanoliter-scale nucleic acid processor with parallel architecture. *Nat. Biotechnol.*, **22**(4), 435–9.

Huang, F. C., Liao, C. S., and Lee, G. B., 2006: An integrated microfluidic chip for DNA/RNA amplification, electrophoresis separation and on-line optical detection. *Electrophoresis*, **27**(16), 3297–305.

Huh, D., Gu, W., Kamotani, Y., Grotberg, J. B., and Takayama, S., 2005: Microfluidics for flow cytometric analysis of cells and particles. *Physiol. Meas.*, **26**(3), R73–98.

Ibarra, R. U., Edwards, J. S., and Palsson, B. O., 2002: *Escherichia coli* K-12 undergoes adaptive evolution to achieve *in silico* predicted optimal growth. *Nature*, **420**(6912), 186–9.

Ideker, T., Thorsson, V., Ranish, J. A., Christmas, R., Buhler, J., Eng, J. K., Bumgarner, R., Goodlett, D. R., Aebersold, R., and Hood, L., 2001: Integrated genomic and proteomic analyses of a systematically perturbed metabolic network. *Science*, **292**(5518), 929–34.

Jaeger, J., and Reinitz, J., 2006: On the dynamic nature of positional information. *Bioessays*, **28**(11), 1102–11.

Josenhans, C., and Suerbaum, S., 2002: The role of motility as a virulence factor in bacteria. *Int. J. Med. Microbiol.*, **291**(8), 605–14.

Kahn, M., Kolter, R., Thomas, C., Figurski, D., Meyer, R., Remaut, E., and Helinski, D. R., 1979: Plasmid cloning vehicles derived from plasmids ColE1, F, R6K, and RK2. *Methods Enzymol.*, **68**, 268–80.

Kobayashi, H., Kærn, M., Araki, M., Chung, K., Gardner, T. S., Cantor, C. R., and Collins, J. J., 2004: Programmable cells: interfacing natural and engineered gene networks. *Proc. Natl. Acad. Sci. U. S. A.*, **101**(22), 8414–9.

Kohn, K. W., and Pommier, Y., 2005: Molecular interaction map of the p53 and Mdm2 logic elements, which control the Off-On switch of p53 in response to DNA damage. *Biochem. Biophys. Res. Commun.*, **331**(3), 816–27.

Lee, S. K., Chou, H. H., Pfleger, B. F., Newman, J. D., Yoshikuni, Y., and Keasling, J. D., 2007: Directed evolution of AraC for improved compatibility of arabinose- and lactose-inducible promoters. *Appl. Environ. Microbiol.*, **73**(18), 5711–5.

Lin, F., Saadi, W., Rhee, S. W., Wang, S. J., Mittal, S., and Jeon, N. L., 2004: Generation of dynamic temporal and spatial concentration gradients using microfluidic devices. *Lab Chip*, **4**(3), 164–7.

Lion, N., Rohner, T. C., Dayon, L., Arnaud, I. L., Damoc, E., Youhnovski, N., Wu, Z. Y., Roussel, C., Josserand, J., Jensen, H., Rossier, J. S., Przybylski, M., and Girault, H. H., 2003: Microfluidic systems in proteomics. *Electrophoresis*, **24**(21), 3533–62.

Lutz, R., and Bujard, H., 1997: Independent and tight regulation of transcriptional units in *Escherichia coli* via the LacR/O, the TetR/O and AraC/I_1-I_2 regulatory elements. *Nucleic Acids Res.*, **25**(6), 1203–10.

Mackey, M. C., and Glass, L., 1977: Oscillation and chaos in physiological control systems. *Science*, **197**(4300), 287–9.

Mackey, M. C., and Nechaeva, I. G., 1995: Solution moment stability in stochastic differential delay equations. *Phys. Rev. E Stat. Phys. Plasmas Fluids Relat. Interdiscip. Topics*, **52**(4), 3366–76.

Mangan, S., Zaslaver, A., and Alon, U., 2003: The coherent feedforward loop serves as a sign-sensitive delay element in transcription networks. *J. Mol. Biol.*, **334**(2), 197–204.

Mao, H., Yang, T., and Cremer, P. S., 2002: A microfluidic device with a linear temperature gradient for parallel and combinatorial measurements. *J. Am. Chem. Soc.*, **124**(16), 4432–5.

McMurray, M. A., and Gottschling, D. E., 2004: Aging and genetic instability in yeast. *Curr. Opin. Microbiol.*, **7**(6), 673–9.

Miller, J. H., 1992: *A short course in bacterial genetics: a laboratory manual and handbook for Escherichia coli and related bacteria.* Cold Spring Harbor Laboratory, Plainview, N. Y.

Narayan, V., Menon, N., and Ramaswamy, S., 2006: Nonequilibrium steady states in a vibrated-rod monolayer: tetratic, nematic, and smectic correlations. *J. Stat. Mech. Theory Exp.*, P01005–1–17.

Ng, J. M., Gitlin, I., Stroock, A. D., and Whitesides, G. M., 2002: Components for integrated poly(dimethylsiloxane) microfluidic systems. *Electrophoresis*, **23**(20), 3461–73.

Olmsted, P. D., and Goldbart, P. M., 1992: Isotropic-nematic transition in shear flow: state selection, coexistence, phase transitions, and critical behavior. *Phys. Rev. A At. Mol. Opt. Phys.*, **46**(8), 4966–93.

Onsager, L., 1949: The effects of shape on the interaction of colloidal particles. *Ann. N. Y. Acad. Sci.*, **51**(4), 627–59.

Ozbudak, E. M., Thattai, M., Lim, H. N., Shraiman, B. I., and van Oudenaarden, A., 2004: Multistability in the lactose utilization network of *Escherichia coli*. *Nature*, **427**(6976), 737–40.

Paegel, B. M., Blazej, R. G., and Mathies, R. A., 2003: Microfluidic devices for DNA sequencing: sample preparation and electrophoretic analysis. *Curr. Opin. Biotechnol.*, **14**(1), 42–50.

Park, S., Wolanin, P. M., Yuzbashyan, E. A., Lin, H., Darnton, N. C., Stock, J. B., Silberzan, P., and Austin, R., 2003: Influence of topology on bacterial social interaction. *Proc. Natl. Acad. Sci. U. S. A.*, **100**(24), 13910–5.

Pedraza, J. M., and van Oudenaarden, A., 2005: Noise propagation in gene networks. *Science*, **307**(5717), 1965–9.

Pratt, L. A., and Kolter, R., 1998: Genetic analysis of *Escherichia coli* biofilm formation: roles of flagella, motility, chemotaxis and type I pili. *Mol. Microbiol.*, **30**(2), 285–93.

Rapaport, D. C., 2004: *The Art of Molecular Dynamics Simulation*. Cambridge University Press, Cambridge, 2nd edition.

Rateitschak, K., and Wolkenhauer, O., 2007: Intracellular delay limits cyclic changes in gene expression. *Math. Biosci.*, **205**(2), 163–79.

Rosenfeld, N., Young, J. W., Alon, U., Swain, P. S., and Elowitz, M. B., 2005: Gene regulation at the single-cell level. *Science*, **307**(5717), 1962–5.

Schäfer, J., Dippel, S., and Wolf, D. E., 1996: Force schemes in simulations of granular materials. *J. Phys. I*, **6**(1), 5–20.

Scheibel, T., Bloom, J., and Lindquist, S. L., 2004: The elongation of yeast prion fibers involves separable steps of association and conversion. *Proc. Natl. Acad. Sci. U. S. A.*, **101**(8), 2287–92.

Schembri, M. A., Kjærgaard, K., and Klemm, P., 2003: Global gene expression in *Escherichia coli* biofilms. *Mol. Microbiol.*, **48**(1), 253–67.

Schuster, M., Hawkins, A. C., Harwood, C. S., and Greenberg, E. P., 2004: The *Pseudomonas aeruginosa* RpoS regulon and its relationship to quorum sensing. *Mol. Microbiol.*, **51**(4), 973–85.

Shaner, N. C., Steinbach, P. A., and Tsien, R. Y., 2005: A guide to choosing fluorescent proteins. *Nat. Methods*, **2**(12), 905–9.

Sheff, M. A., and Thorn, K. S., 2004: Optimized cassettes for fluorescent protein tagging in *Saccharomyces cerevisiae*. *Yeast*, **21**(8), 661–70.

Shraiman, B. I., 2005: Mechanical feedback as a possible regulator of tissue growth. *Proc. Natl. Acad. Sci. U. S. A.*, **102**(9), 3318–23.

Sia, S. K., and Whitesides, G. M., 2003: Microfluidic devices fabricated in poly(dimethylsiloxane) for biological studies. *Electrophoresis*, **24**(21), 3563–76.

Siegele, D. A., and Hu, J. C., 1997: Gene expression from plasmids containing the *araBAD* promoter at subsaturating inducer concentrations represents mixed populations. *Proc. Natl. Acad. Sci. U. S. A.*, **94**(15), 8168–72.

Simon, I., Barnett, J., Hannett, N., Harbison, C. T., Rinaldi, N. J., Volkert, T. L., Wyrick, J. J., Zeitlinger, J., Gifford, D. K., Jaakkola, T. S., and Young, R. A., 2001: Serial regulation of transcriptional regulators in the yeast cell cycle. *Cell*, **106**(6), 697–708.

Simon, J. A., and Yen, T. J., 2003: Novel approaches to screen for anticancer drugs using *Saccharomyces cerevisiae*. *Methods Mol. Biol.*, **223**, 555–76.

Simpson, M. L., Cox, C. D., and Sayler, G. S., 2003: Frequency domain analysis of noise in autoregulated gene circuits. *Proc. Natl. Acad. Sci. U. S. A.*, **100**(8), 4551–6.

Sprinzak, D., and Elowitz, M. B., 2005: Reconstruction of genetic circuits. *Nature*, **438**(7067), 443–8.

Stricker, J.*, Cookson, S.*, Bennett, M. R.*, Mather, W. H., Tsimring, L. S., and Hasty, J., 2008: A fast, robust and tunable synthetic gene oscillator. *Nature*. doi:10.1038/nature07389. (*equal contribution).

Sveen, J. K., and Cowen, E. A., 2004: *PIV and Water Waves*, volume 9 of *Advances in Coastal and Ocean Engineering*, chapter Quantitative imaging techniques and their application to wavy flows, 1–49. World Scientific, Singapore.

Tavazoie, S., Hughes, J. D., Campbell, M. J., Cho, R. J., and Church, G. M., 1999: Systematic determination of genetic network architecture. *Nat. Genet.*, **22**(3), 281–5.

Tesla, N., 1920: U. S. Patent No. 1,329,559.

Thompson, D. M., King, K. R., Wieder, K. J., Toner, M., Yarmush, M. L., and Jayaraman, A., 2004: Dynamic gene expression profiling using a microfabricated living cell array. *Anal. Chem.*, **76**(14), 4098–103.

Thorsen, T., Maerkl, S. J., and Quake, S. R., 2002: Microfluidic large-scale integration. *Science*, **298**(5593), 580–4.

Tourovskaia, A., Figueroa-Masot, X., and Folch, A., 2005: Differentiation-on-a-chip: a microfluidic platform for long-term cell culture studies. *Lab Chip*, **5**(1), 14–9.

Tyson, J. J., Chen, K. C., and Novak, B., 2003: Sniffers, buzzers, toggles and blinkers: dynamics of regulatory and signaling pathways in the cell. *Curr. Opin. Cell Biol.*, **15**(2), 221–31.

Unger, M. A., Chou, H. P., Thorsen, T., Scherer, A., and Quake, S. R., 2000: Monolithic microfabricated valves and pumps by multilayer soft lithography. *Science*, **288**(5463), 113–6.

Venturoli, D., and Rippe, B., 2005: Ficoll and dextran vs. globular proteins as probes for testing glomerular permselectivity: effects of molecular size, shape, charge, and deformability. *Am. J. Physiol. Renal Physiol.*, **288**(4), F605–13.

Vincent, L., 1993: Morphological grayscale reconstruction in image analysis: applications and efficient algorithms. *IEEE Trans. Image Process.*, **2**(2), 176–201.

Vogelstein, B., Lane, D., and Levine, A. J., 2000: Surfing the p53 network. *Nature*, **408**(6810), 307–10.

Volfson, D., Tsimring, L. S., and Aranson, I. S., 2004: Stick-slip dynamics of a granular layer under shear. *Phys. Rev. E Stat. Phys. Plasmas Fluids Relat. Interdiscip. Topics*, **69**(3), 031302–1–4.

Volfson, D.*, Cookson, S.*, Hasty, J., and Tsimring, L. S., 2008: Biomechanical ordering of dense cell populations. *Proc. Natl. Acad. Sci. U. S. A.*, **105**(40), 15346–51. (*equal contribution).

Walker, G. M., Zeringue, H. C., and Beebe, D. J., 2004: Microenvironment design considerations for cellular scale studies. *Lab Chip*, **4**(2), 91–7.

Wang, X., Hao, N., Dohlman, H. G., and Elston, T. C., 2006: Bistability, stochasticity, and oscillations in the mitogen-activated protein kinase cascade. *Biophys. J.*, **90**(6), 1961–78.

Wheeler, A. R., Throndset, W. R., Whelan, R. J., Leach, A. M., Zare, R. N., Liao, Y. H., Farrell, K., Manger, I. D., and Daridon, A., 2003: Microfluidic device for single-cell analysis. *Anal. Chem.*, **75**(14), 3581–6.

Whitesides, G. M., Ostuni, E., Takayama, S., Jiang, X., and Ingber, D. E., 2001: Soft lithography in biology and biochemistry. *Annu. Rev. Biomed. Eng.*, **3**, 335–73.

Wu, Z. Y., Xanthopoulos, N., Reymond, F., Rossier, J. S., and Girault, H. H., 2002: Polymer microchips bonded by O_2-plasma activation. *Electrophoresis*, **23**(5), 782–90.

You, L., Cox, I., R. S., Weiss, R., and Arnold, F. H., 2004: Programmed population control by cell-cell communication and regulated killing. *Nature*, **428**(6985), 868–71.

Zacharias, D. A., Violin, J. D., Newton, A. C., and Tsien, R. Y., 2002: Partitioning of lipid-modified monomeric GFPs into membrane microdomains of live cells. *Science*, **296**(5569), 913–6.